

ABSTRACT

Convective Heat Transfer from Realistic Ice Roughness Distributions

Joshua Logan Tecson, M.S.M.E.

Mentor: Stephen T. McClain, Ph.D.

As supercooled water droplets impinge the surfaces of in-flight aircraft, a layer of accreted ice will form. In the initial stages of the accretion process, the ice will form as a distributed surface roughness. Ice accretions degrade the aerodynamic performance and safety of an aircraft. Icing effects are simulated and mitigated during aircraft design through the use of computational ice accretion codes. A significant area for improvement of these codes exists in the simplistic characterization of convective heat transfer from ice roughness. A better characterization of convective heat transfer must be obtained for flows over surfaces with realistic ice roughness properties and relevant thermal boundary conditions. A series of steady state experiments was performed in a wind tunnel on a flat plate with two realistic ice roughness surfaces. Using an infrared camera, detailed maps of convective heat transfer coefficients were obtained for the surfaces.

Convective Heat Transfer from Realistic Ice Roughness Distributions

by

Joshua Logan Tecson, B.S.M.E

A Thesis

Approved by the Department of Mechanical Engineering

William Jordan, Ph.D., Chairperson

Submitted to the Graduate Faculty of
Baylor University in Partial Fulfillment of the
Requirements for the Degree
of
Master of Science in Mechanical Engineering

Approved by the Thesis Committee

Stephen T. McClain, Ph.D., Chairperson

Lesley M. Wright, Ph.D.

Jack D. Tubbs, Ph.D.

Accepted by the Graduate School

May 2013

J. Larry Lyon, Ph.D., Dean

Copyright © 2013 by Joshua Logan Tecson

All rights reserved

TABLE OF CONTENTS

LIST OF FIGURES	vii
LIST OF TABLES	xi
NOMENCLATURE	xii
ACKNOWLEDGMENTS	xvi
DEDICATION	xvii
CHAPTER ONE	1
Introduction	1
Impact of Aircraft Icing	1
Use of Ice Accretion Codes	2
Objectives and Significance of Work	3
Presentation Outline	4
CHAPTER TWO	5
Technical Background	5
Fluid Mechanics and Heat Transfer Background	5
Boundary Layers	5
Surface Roughness	11
Airfoils	16
Ice Roughness Background	18
The Messinger Model for Aircraft Icing	21
Ice Roughness in LEWICE	22
Improvements in Ice Roughness Modeling	25

CHAPTER THREE	29
Materials and Methodology	29
Instrumented Test Plate	29
Test Plate Design	29
Required Tools and Materials	33
Initial Test Plate Machining	34
Subsurface Thermocouple Installation	35
Heated Section Preparation	36
Gold Deposited Mylar Film Installation	37
Wiring	40
Creation of Testable Ice Roughness	41
Lagrangian Droplet Simulator Development	41
Matching to Reported Data	44
Manufacture of Testable Surfaces	51
Experimental Procedure and Instrumentation	54
Steady State Convective Heat Transfer Coefficient Test	56
Thermal Boundary Layer Measurement	63
Velocity Boundary Layer Measurement	65
CHAPTER FOUR	66
Data Reduction and Uncertainty Analysis	66
Convective Heat Transfer Coefficient Measurements	66
Air Properties	66
Temperature Calibration	67

Heat Transfer Equation	68
Smooth Surface Validation	70
Evaluation of Uncertainty	73
Boundary Layer Thickness Measurements	77
Viscous Boundary Layer	77
Thermal Boundary Layer	78
CHAPTER FIVE	84
Results and Discussion	84
Convective Heat Transfer Results	84
Convective Heat Transfer Enhancement	96
Element Interaction Effects	98
Heat Loss Modes	100
Boundary Layer Results	101
CHAPTER SIX	106
Conclusions	106
Summary of Current Work	106
Recommendations for Future Work	107
APPENDIX A	110
Data Reduction MATLAB Code	110
APPENDIX B	117
Evaluation of Uncertainty Mathcad Worksheet	117
REFERENCES	135

LIST OF FIGURES

Figure 1.1:	Effect of icing exposure time to aerodynamic characteristics [1] ...	2
Figure 2.1:	Viscous boundary layer development over a flat plate	6
Figure 2.2:	Thermal boundary layer on a flat plate, $T_\infty < T_S$	8
Figure 2.3:	Comparison of flat plate correlations for h and c_f	10
Figure 2.4:	Representations of complex flow fields over a single roughness element in laminar boundary layer [15]	12
Figure 2.5:	Single roughness element on a flat plate with (a) isothermal heating and (b) unheated starting length [16]	13
Figure 2.6:	Viscous and thermal boundary layers for the scenarios of Figure 2.5 [16]	13
Figure 2.7:	Comparison of ABS and aluminum roughness element temperature distributions from Mart [33]	14
Figure 2.8:	Forces on an airfoil (a) pressure, (b) viscosity, and (c) resultant	16
Figure 2.9:	Boundary layer separation due to an adverse pressure gradient (not to scale)	17
Figure 2.10:	Ice roughness examples	18
Figure 2.11:	Appendix C design envelopes [6]	20
Figure 2.12:	Modes of energy transfer on a generic airfoil [24]	21
Figure 2.13:	Comparison of measured and predicted roughness height [26]	24
Figure 2.14:	Simplistic ice roughness distributions used by Poinatte et al. [21]	26
Figure 3.1:	Conceptual design for the test plate	30
Figure 3.2:	Side view of instrumented test plate model	31

Figure 3.3:	Isometric view of test plate with hidden features shown	31
Figure 3.4:	Surface plate grid and heated sections, dimensions are in inches ...	33
Figure 3.5:	Plexiglas test plate after initial machining	35
Figure 3.6:	Heated section 0 prior to the Mylar film application	37
Figure 3.7:	Heated section partially prepared for spray adhesive, target area outlined	38
Figure 3.8:	Mylar film prepared for cutting, cutting lines outlined	39
Figure 3.9:	Completed heated section	40
Figure 3.10:	Completed instrumented test plate	41
Figure 3.11:	Comparison of simulator results	43
Figure 3.12:	Histograms for three impinged droplet numbers showing the increasing second mode	44
Figure 3.13:	Images of roughness for cases (a) “5-29-96 Run 4” and (b) “5-30-96 Run 1” from the experiments of Anderson et al. [23]	45
Figure 3.14:	Comparison of droplet distributions for the “5-29-96 Run 4” case from (a) unconditioned data, (b) truncated data, (c) truncated and stretched data, and (d) truncated, stretched, and scaled data	49
Figure 3.15:	Comparison of droplet diameter distributions for the “5-29-96 Run 4” case from (a) Anderson et al. [23], (b) unmodified Lagrangian droplet simulator data, (c) truncated and stretched data, and (d) truncated, stretched, and scaled data	50
Figure 3.16:	Scaling and replication of a roughness surface for “5-29-96 run 4” (not to scale)	52
Figure 3.17:	052996_run4_x10 surface comparison	55
Figure 3.18:	053096_run1_x10 surface comparison	56
Figure 3.19:	IR equipment installed on the wind tunnel ceiling	57
Figure 3.20:	Thermocouple and IR window locations, dimensions are in inches	58

Figure 3.21:	Wiring diagrams for power supply and measurement	60
Figure 3.22:	Data acquisition cart setup	61
Figure 3.23:	Boundary layer traversing ceiling installed on wind tunnel	64
Figure 4.1:	Heat transfer diagram (not to scale)	69
Figure 4.2:	Surface maps for the smooth laminar surface	73
Figure 4.3:	Surface maps for the smooth turbulent surface	74
Figure 4.4:	Comparison of centerline experimental and theoretical heat transfer	75
Figure 4.5:	Measured and theoretical viscous boundary layer comparisons for the smooth surfaces	79
Figure 4.6:	Nondimensional velocity profile traces for the smooth surfaces	80
Figure 4.7:	Measured and theoretical thermal boundary layer comparisons for the smooth surfaces	81
Figure 4.8:	Nondimensional temperature profile traces for the smooth surfaces	82
Figure 5.1:	Surface maps for the 052996_run4_x10 surface	89
Figure 5.2:	Surface maps for the 053096_run1_x10 surface	90
Figure 5.3:	Centerline ± 0.5 " spanwise averaged convective heat transfer coefficients	91
Figure 5.4:	Area averaged convective heat transfer coefficient comparison	94
Figure 5.5:	Nondimensional convective heat transfer coefficient comparison	95
Figure 5.6:	Convective heat transfer enhancement comparison	97
Figure 5.7:	Element pair locations, flow is from left to right	99
Figure 5.8:	Viscous and thermal boundary layer thicknesses for the rough surfaces	102

Figure 5.9:	Viscous and thermal boundary layer thicknesses comparison for all surfaces	103
Figure 5.10:	Nondimensional velocity profile traces for the rough surfaces	104
Figure 5.11:	Nondimensional temperature profile traces for the rough surfaces	105

LIST OF TABLES

Table 3.1:	Comparison of unconditioned and conditioned simulator surface statistics to “5-29-96 Run 4” reported values	47
Table 3.2:	Comparison of unconditioned and conditioned simulator surface statistics to “5-30-96 Run 1” reported values	50
Table 3.3:	Stated ranges and accuracies of instrumentation	61
Table 4.1:	Air properties during convective heat transfer tests	67
Table 4.2:	Total uncertainties and components	76
Table 5.1:	Smooth laminar surface test data	85
Table 5.2:	Smooth turbulent surface test data	86
Table 5.3:	052996_run4_x10 surface test data	87
Table 5.4:	053096_run1_x10 surface test data	88
Table 5.5:	052996_run4_x10 element data	100
Table 5.6:	053096_run1_x10 element data	100
Table 5.7:	Percentage of heat transfer by mode	101

NOMENCLATURE

A_{pix}	Pixel area (4.00E-04 in ²)
A_t	Total area of heated section
Bi	Biot number
B_T	Correlated uncertainty (1.4 K)
c_f	Skin friction coefficient
c_p	Specific heat of the fluid
D	Roughness element diameter
E	Voltage across heated section
F_s	Spacing scaling factor
F_d	Diameter scaling factor
h	Convective heat transfer coefficient
H/D	Roughness element height-to-diameter ratio
I	Current through heated section
k_f	Fluid thermal conductivity
k_p	Plexiglas thermal conductivity
k_s	Solid thermal conductivity
k_φ	Thermal conductivity at the icing surface
L_c	Characteristic length
L_{ha}	Length of heated area
N	Measurement sample size
N_E	Number of roughness elements on a surface
$N_{f,\text{stag}}$	Freezing fraction at stagnation point

Nu	Nusselt number
P	Roughness element spacing
Pr	Prandtl number
Q	Heat transfer terms in data reduction
q"	Heating terms in the Messinger model
Re	Reynolds number
S	Standard deviation
S _E	Element diameter standard deviation
T _{BL}	Boundary layer temperature
T _∞	Freestream temperature
T _{IR}	Infrared calibrated temperature
T _S	Surface or wall temperature
T _{SS}	Subsurface thermocouple calibrated temperature
T _{UP}	Under the plate thermocouple calibrated temperature
t	Student's t-value
t _p	Plexiglas thickness
u	Velocity inside of boundary layer
U	Uncertainty
U _∞	Freestream velocity
W	IR camera detector power measurement
W _{ha}	Width of heated area
x	Flowwise location on plate
x _{cr}	Critical distance for flow transition

x_k	Sand-grain equivalent roughness height from LEWICE
y	Spanwise location on plate
z	Vertical distance from plate surface

Greek

δ	Viscous boundary layer height
δ_T	Thermal boundary layer height
ε	Emissivity (0.95)
θ	Nondimensional temperature
μ	Dynamic fluid viscosity
ν	Kinematic fluid viscosity
ξ	Starting length
ρ	Fluid density
σ	Stefan-Boltzmann constant (5.67E-08)
τ	Transmissivity (0.82)
τ_w	Wall shear stress
φ	Surface normal to icing surface in LEWICE

Subscripts

IR,C	Infrared camera temperature measured during calibration
IR,S	Infrared camera temperature measured at steady state
TC,C	Thermocouple temperature measured during calibration
TC,S	Thermocouple temperature measured at steady state

Abbreviations

IRT Icing research tunnel

LWC Liquid water content

MVD Median volumetric diameter

ACKNOWLEDGMENTS

First and foremost, I would like to thank Dr. Stephen McClain for serving as my advisor. Without his support and mentorship this thesis would not have been possible. I would also like to thank Dr. Lesley Wright and Dr. Jack Tubbs for serving as members of my thesis defense committee. Your time and perspective is invaluable to the development of this document. I would also like to thank Mr. Ashley Orr and Mr. Dan Hromadka for helping with various aspects of apparatus construction. Finally, I would like to thank my fellow graduate students Cash Elston, Charlie Brown, Chris Walker, Weston Harmon, Russ Mailen, Ben Lewis, Josh Weed, and John Bitter for their assistance in exchanging wind tunnel test section parts.

The efforts reported in this document were performed as part NASA Collaborative Agreement No. NNX12AB85A. The assistance and guidance of the members of the Icing Research Branch at NASA Glenn Research Center are greatly appreciated, especially Mario Vargas, Ron Colantonio, Mary Wadel, Eric Kreeger, and Paul Tsao. Any opinions presented in this document are those of the authors and do not reflect the views of NASA or the United States government.

DEDICATION

To my wife and family

CHAPTER ONE

Introduction

Impact of Aircraft Icing

In-flight icing of aircraft is a well-documented, yet not fully understood, natural phenomenon. It occurs as supercooled water droplets impinge and freeze on an aircraft surface. Given sufficient time in icing conditions, an accreted layer of ice will form which can become large enough to negatively affect the performance and safety of an aircraft. The aerodynamic impacts can manifest as a reduction in the stall margin, increase in drag, decrease in lift, and an increase in aircraft weight. Addy [1] showed that exposure to icing conditions for as little as two minutes can have a significant negative impact on the lift coefficient and stall angle of an airfoil. Figure 1.1 shows an example of performance degradation for a general aviation airfoil subjected to icing conditions. Further, Figure 1.1 illustrates that continued exposure to icing conditions will lead to continued performance degradation. In addition to the potential aerodynamic effects, icing can also lead to the failure of external sensors and mechanical parts (such as wing flaps) as ice continues to accrete.

Between 1998 and 2009, almost 3000 icing related aviation events (including 229 fatalities) were reported to various government agencies, with countless other non-reportable events surely occurring in that time span [2]. Ideally, icing conditions would be avoided altogether; however, this is not always practical or possible. The next best option would be prevention of ice formation (anti-icing systems) or complete removal of accreted ice (de-icing systems). However, due to the potential for relatively high energy

consumption requirements, it is often not feasible to design an aircraft to obtain complete de-icing or anti-icing capabilities while remaining “economically competitive” in the system design [3]. As a consequence, all aircraft must be able to operate with some degree of tolerated ice [4]. The current federal code regulating aircraft icing tolerance for flight certification is the Code of Federal Regulations, Title 14, §25, Appendix C (known simply as “Appendix C icing conditions” going forward) [5,6].

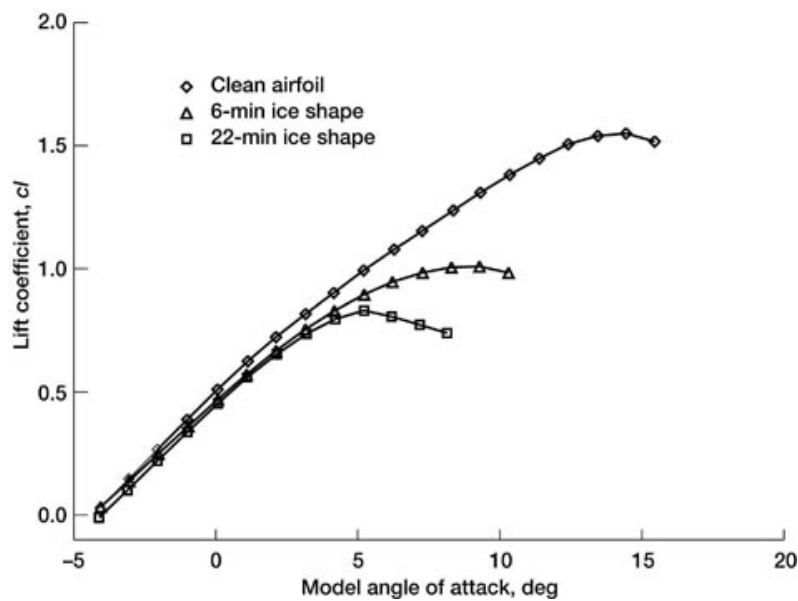


Figure 1.1: Effect of icing exposure time on aerodynamic characteristics [1]

Use of Ice Accretion Codes

Designing aircraft for flight certification in Appendix C icing conditions was once a costly process, with new designs requiring a range of expensive full-scale icing tests [4]. Due to increased availability and effectiveness, ice accretion codes coupled with computational fluid dynamics (CFD) simulations are now commonly used during aircraft design to predict icing effects. The goal of these codes is to accurately predict both the size and shape of the final accreted ice layer for given icing conditions [3]. Proper

prediction of the size (or mass) of an ice accretion aids in the sizing of ice protection systems to mitigate icing effects. Proper prediction of the shape of an ice accretion aids in predicting aerodynamic effects and determining safe aircraft operating conditions. These simulations give engineers more insight and confidence in their designs prior to certification testing, greatly reducing testing costs [7]. The use of simulations also allows for a relatively simple study of icing effects across a large range of conditions.

Objectives and Significance of Work

Due to the prevalence of icing codes in modern aircraft design, constant efforts are made to improve their predictive capabilities. One of the biggest areas for improvement in icing codes exists in the characterization of convective heat transfer from the ice roughness that forms in the initial stages of icing [8]. Ice roughness is an important factor because it couples the fluid flow, heat transfer, and droplet impingement processes [9]; however, it is difficult to characterize due to the chaotic nature of its formation [3]. A better understanding of the convective heat transfer behavior of realistic ice roughness distributions will help improve the accuracy and effectiveness of icing codes.

In this study, the convective heat transfer behavior of two surfaces reflective of Appendix C ice roughness were investigated in a subsonic wind tunnel utilizing a flat plate study. A smooth surface was also tested to calibrate and validate the experimental setup. A series of three experiments was performed for each surface: 1) steady state convective heat transfer coefficient measurement, 2) velocity boundary layer measurement, and 3) thermal boundary layer measurement. The main objective of this work was to uncover a fundamental understanding of the convective heat transfer

behavior from surfaces with realistic ice roughness and how it relates to boundary layer development. This work will serve as a building block for future studies on ice roughness convective heat transfer, serving to improve ice accretion codes.

Presentation Outline

The remainder of this document is organized as follows. Chapter Two provides a technical background for fluid mechanics, heat transfer, aircraft icing, ice accretion codes, and ice roughness. Chapter Three details the processes used in the development of the experimental apparatuses and the procedures used during experimentation. Chapter Four presents the data reduction and uncertainty analysis methods which were developed to analyze the experimental data. Chapter Five presents and discusses the results of the investigation. Chapter Six provides concluding remarks and suggestions for future work. Appendix A contains an example calculation for the reduction of the convective heat transfer coefficient data. Appendix B contains an example calculation for the determination of experimental uncertainty.

CHAPTER TWO

Technical Background

This chapter provides a fundamental background on the topics important to understanding the purpose and impact of this investigation. It begins with a basic review of boundary layer flows, the effects of surface roughness, and the operating principles of airfoils. The fundamentals of aircraft icing physics are then introduced, finishing with a focus on ice roughness.

Fluid Mechanics and Heat Transfer Background

Boundary Layers

Boundary layer theory was first introduced by Ludwig Prandtl in 1904 [10] and has remained an important part of fluid mechanics ever since. A viscous (or velocity) boundary layer is a slender region near the wall of an object where the significant variations in the velocity of a fluid will take place [11]. The boundary layer is also the area where the viscous effects of a fluid are important. The area outside of the boundary layer is typically considered to be inviscid. Figure 2.1 shows how the viscous boundary layer will develop as fluid flows over a flat plate. For a given location on the plate (x) the velocity inside the boundary layer (u) is assumed to vary as a function of vertical distance from the surface (z) only, or $u(z)$. As a general rule, the viscous boundary layer thickness (δ) is considered to extend to the point where $u(z)$ equals 99% of the freestream velocity (U_∞), or $u(z) = 0.99U_\infty$, and varies as a function of x .

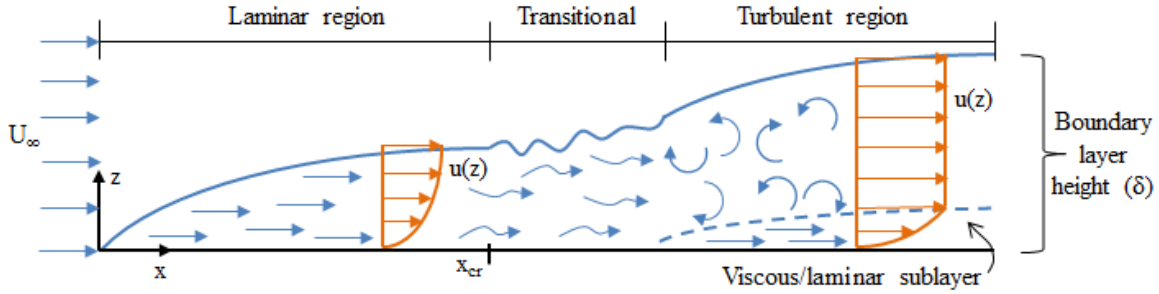


Figure 2.1: Viscous boundary layer development over a flat plate

Figure 2.1 also highlights the different flow regimes a fluid will encounter as the boundary layer develops. The boundary layer begins in the laminar regime. In laminar flow the fluid particles move in a well-ordered manner along streamlines. After some critical distance (x_{cr}) the flow will begin transition to the turbulent regime. In turbulent flow the fluid particle motion is much more chaotic due to the presence of rotating areas of fluid, known as eddies. There is also a very thin viscous (or laminar) sublayer present in the turbulent boundary layer near the wall. The viscous sublayer affects the shape of the boundary layer profile, causing much larger velocity gradients to develop at the wall in turbulent flow when compared to laminar flow. The transitional region between laminar and turbulent flow is not well understood, but the flow behaves in a manner between laminar and turbulent. The Reynolds number is a non-dimensional parameter used to characterize the thickness of the viscous boundary layer. The Reynolds number (Re) for flow over a flat plate (as a function of x) is given by Eq. (2.1),

$$Re = \frac{\rho U_\infty x}{\mu} \quad (2.1)$$

where ρ is the density of the fluid, μ is the dynamic viscosity of the fluid, U_∞ is the freestream fluid velocity, and x is a distance from the leading edge of the plate. It is helpful to consider the Reynolds number as a geometric slenderness ratio which relates

the size of the boundary layer to the distance along the plate [11]. Eq. (2.2) and (2.3) give correlations for boundary layer thickness based on the Reynolds number for laminar and turbulent flow, respectively.

$$\delta = 4.91xRe^{-1/2} \quad (2.2)$$

$$\delta = 0.382xRe^{-1/5} \quad (2.3)$$

The Reynolds number is also used to establish flow similarity, that is, flows with similar Reynolds numbers behave in a similar manner. Undisturbed flat plate flows with a Reynolds number of less than 5×10^5 can be considered laminar, while flows with a Reynolds number above this value are expected to be transitional or turbulent [13].

A wall shear stress (τ_w) will develop as a result of the force exerted by the fluid viscosity in the boundary layer. The wall shear stress is a function of the fluid viscosity and the velocity gradient at the wall, as expressed by Eq. (2.4).

$$\tau_w = \mu \left(\frac{\partial u}{\partial y} \right)_{y=0} \quad (2.4)$$

Wall shear stress will vary along the surface of the plate. The skin friction coefficient (c_f) is often used to express the wall shear stress in a non-dimensional form and is given by Eq. (2.5).

$$c_f = \frac{\tau_w}{0.5\rho U_\infty} \quad (2.5)$$

The skin friction coefficient is an important parameter because it is directly related to the parasitic drag on an object, such as an airfoil. Eqs. (2.6) and (2.7) give correlations for the skin friction coefficient along a flat plate for laminar and turbulent flow, respectively.

$$c_f = 0.664Re^{-1/2} \quad (2.6)$$

$$c_f = 0.0592Re^{-1/5} \quad (2.7)$$

For flows with differing wall/surface (T_S) and freestream fluid (T_∞) temperatures, a thermal boundary layer will develop in a manner similar to the viscous boundary layer. The thermal boundary layer is the area where the significant variations in fluid temperature will occur. Figure 2.2 shows the development of a thermal boundary layer over a flat plate with $T_\infty < T_S$.

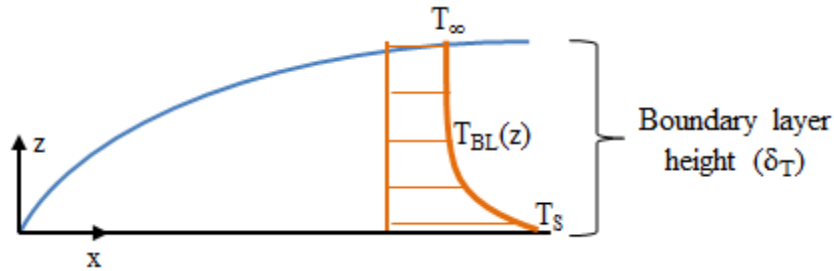


Figure 2.2: Thermal boundary layer on a flat plate, $T_\infty < T_S$

Similar to the viscous boundary layer, the temperature inside the boundary layer (T_{BL}) is assumed to vary only as a function of z for a given x location, or $T_{BL}(z)$. The thermal boundary layer thickness (δ_T) extends to the point where the temperature difference between the boundary layer and the surface equals 99% of the temperature difference between the freestream temperature and the surface, or $(T_{BL}(z) - T_S) = 0.99(T_\infty - T_S)$.

The Prandtl number is a non-dimensional parameter used to characterize the size of the thermal boundary layer. Like the Reynolds number, the Prandtl number can be viewed as a geometric scaling parameter, relating the size of the viscous and thermal boundary layers by comparing the rate of viscous diffusivity to thermal diffusivity [11].

The Prandtl number (Pr) is given by Eq. (2.8),

$$Pr = \frac{c_p \mu}{k_f} = \frac{\nu}{\alpha} \quad (2.8)$$

where c_p is the specific heat of the fluid, k_f is the thermal conductivity of the fluid, ν is the kinematic viscosity of the fluid, and α is the thermal diffusivity of the fluid. For an isothermal plate a Prandtl number greater than one implies a thicker viscous boundary layer while a Prandtl number less than one implies a thicker thermal boundary layer.

Similar to the way that skin friction develops in the viscous boundary layer due to velocity gradients at the wall, the temperature gradient that exists in the thermal boundary layer, along with bulk fluid motion, will drive convective heat transfer. The Nusselt number (Nu) is a useful parameter which gives a non-dimensional form of the convective heat transfer coefficient (h), given by Eq. (2.9).

$$Nu = \frac{hx}{k_f} \quad (2.9)$$

The Nusselt number is often presented as a function of the Reynolds and Prandtl numbers. Eq. (2.10) presents such a correlation for laminar flow over a smooth flat plate with a constant heat flux boundary condition [13].

$$Nu = 0.453Re^{1/2}Pr^{1/3} \quad (2.10)$$

Eq. (2.11) presents a correlation for turbulent flow over a smooth flat plate with a constant heat flux boundary condition [13].

$$Nu = 0.0308Re^{4/5}Pr^{1/3} \quad (2.11)$$

These correlations provide insight into the convective heat transfer behavior to be expected from a flat plate for the specified conditions. A correction factor can be applied to these correlations to account for an unheated starting length (ξ) on the plate since thermal boundary layer development and convection do not occur along the unheated length [12]. For laminar flow the correction factor is $(1 - (x/\xi)^{3/4})^{-1/3}$ and for turbulent flow the correction factor is $(1 - (x/\xi)^{9/10})^{-1/9}$.

Figure 2.3 shows the results of Eqs. (2.10) and (2.11), solved for h , for air at 20 °C flowing over a one meter long flat plate at 15 m/s. The skin friction from Eqs. (2.6) and (2.7) is also shown. The critical distance for transition in this case is 0.5 m, which is presented as an instantaneous change, with no transitional region, for convenience. Note the general trend (within each flow regime) for both h and c_f to decrease with increasing distance along the surface. This is due to the growth of the viscous and thermal boundary layers causing smaller velocity and temperature gradients at the plate surface. Since these gradients drive h and c_f , smaller gradients imply lower values. Also note the sharp increase in both h and c_f when the flow becomes turbulent. This is due to the increased chaos and mixing in the turbulent regime, as well as the larger velocity and temperature gradients which develop at the surface due to the viscous sublayer. The quantities h and c_f can be approximately related by use of the Reynolds analogy, which correlates wall shear stress and heat flux [12].

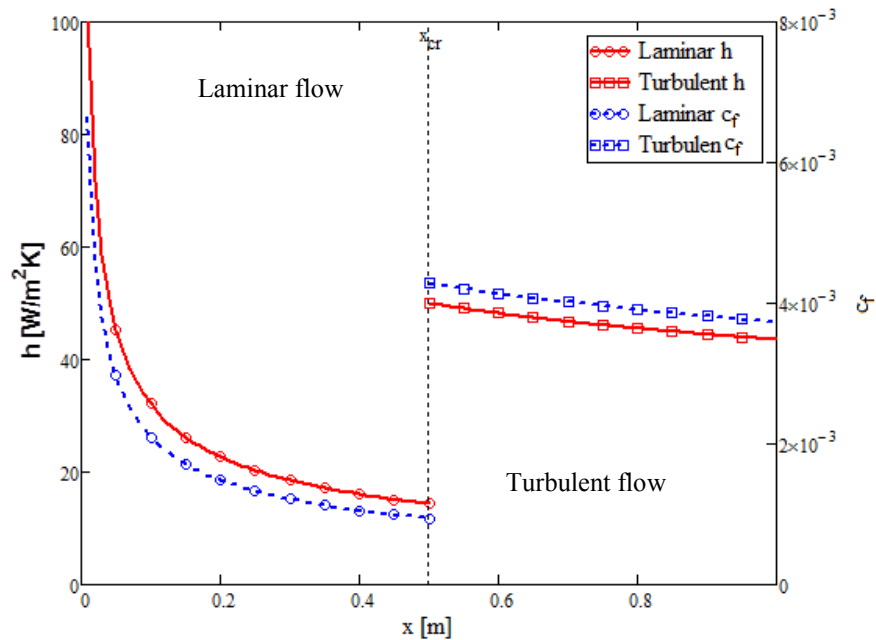


Figure 2.3: Comparison of flat plate correlations for h and c_f

The Biot number (Bi) is another useful non-dimensional heat transfer parameter. It relates the resistance of a body to external heat convection to its resistance to internal heat conduction [12]. It is given by Eq. (2.12),

$$Bi = \frac{h}{k_s/L_c} \quad (2.12)$$

where L_c is a characteristic body length and k_s is the thermal conductivity of the solid body. A higher Biot number indicates higher resistance to internal heat conduction; therefore, larger temperature gradients will develop across the body when heated.

Surface Roughness

Surface roughness appears in many forms; from manufacturing imperfections on pipe walls to fuel depositions on gas turbine engine blades, or as it relates to the current investigation, accreted ice. As demonstrated by Schlichting [14] in his foundational paper on the effects of surface roughness, skin friction is impacted differently by the presence of roughness depending on the flow regime. In general, skin friction is most affected by the presence of roughness in a turbulent boundary layer. Although the overall height of the boundary layer increases in the turbulent regime, the viscous sublayer is much smaller than a laminar boundary layer. As a consequence, surface roughness is likely to protrude through the laminar sublayer and alter the wall shear stress [14].

As seen in Figure 2.4, a single roughness element protruding through a boundary layer can lead to the formation of complex flow fields around the element, disturbing the boundary layer. This can cause an otherwise laminar boundary layer to prematurely transition to turbulence, leading to enhanced convective heat transfer. The surface roughness elements also exhibit a fin-like behavior, enhancing heat transfer.

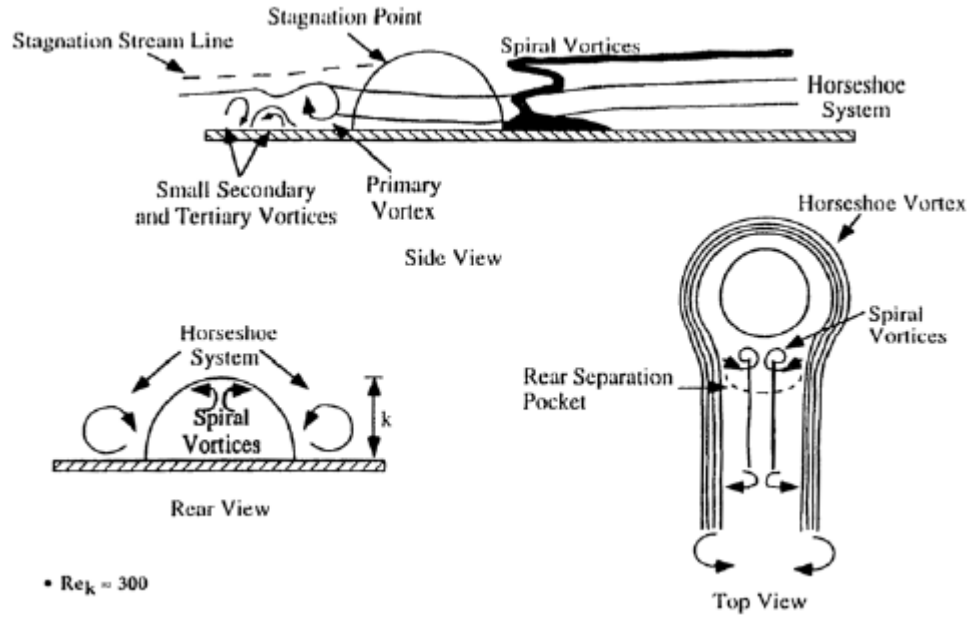


Figure 2.4: Representations of complex flow fields over a single roughness element in a laminar boundary layer [15]

As demonstrated by Mart and McClain [16], the height of the surface roughness relative to the size of the viscous and thermal boundary layers is also important as it relates to convective heat transfer. Consider the scenarios presented in Figure 2.5. A single roughness element is affixed to a heated flat plate with (a) isothermal heating and (b) an unheated starting length. In these scenarios, the roughness element will experience the same viscous boundary layer regardless of heating conditions, but the thermal boundary layer thicknesses will differ. Figure 2.6 shows the differences in the thermal boundary layers (indicated by θ_f) encountered by a 4.77 mm tall roughness element subjected to the scenarios presented in Figure 2.5. Figure 2.6 indicates a difference of about 20% in the boundary layer temperature at the element apex, which will greatly impact the convective heat transfer at the element surface. This behavior can be extended to surface roughness elements distributed at different locations along an isothermal plate,

all experiencing different thermal boundary layer profiles. As a consequence, it is important to characterize the development of both the viscous and thermal boundary layers when quantifying convective heat transfer behavior on rough surfaces [16].

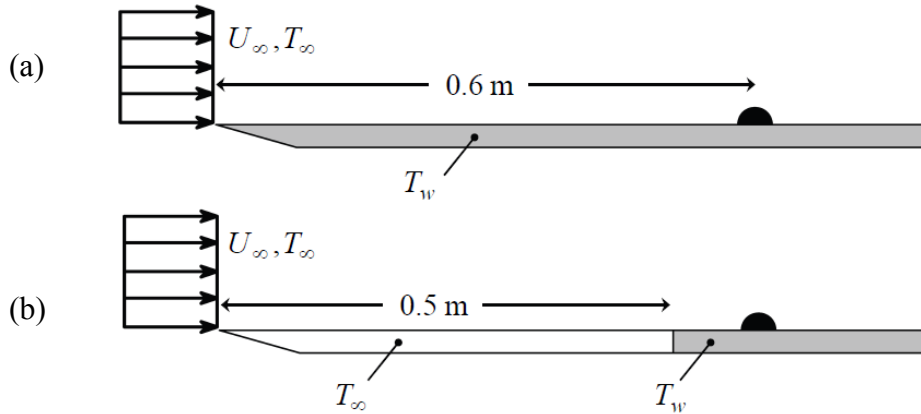


Figure 2.5: Single roughness element on a flat plate with (a) isothermal heating and (b) unheated starting length [16]

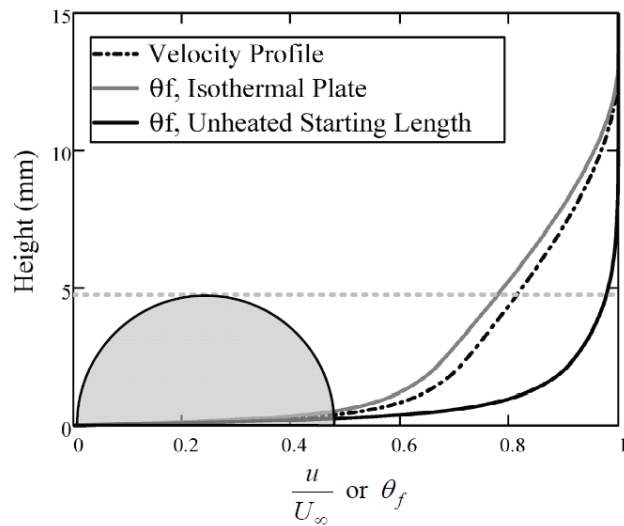


Figure 2.6: Viscous and thermal boundary layers for the scenarios of Figure 2.5 [16]

It is also important to consider the effects of roughness element thermal conductivity on convective heat transfer. Mart [33] constructed two identical surface roughness distributions using 9.53 mm diameter hemispherical elements arranged in a

all experiencing different thermal boundary layer profiles. As a consequence, it is important to characterize the development of both the viscous and thermal boundary layers when quantifying convective heat transfer behavior on rough surfaces [16].

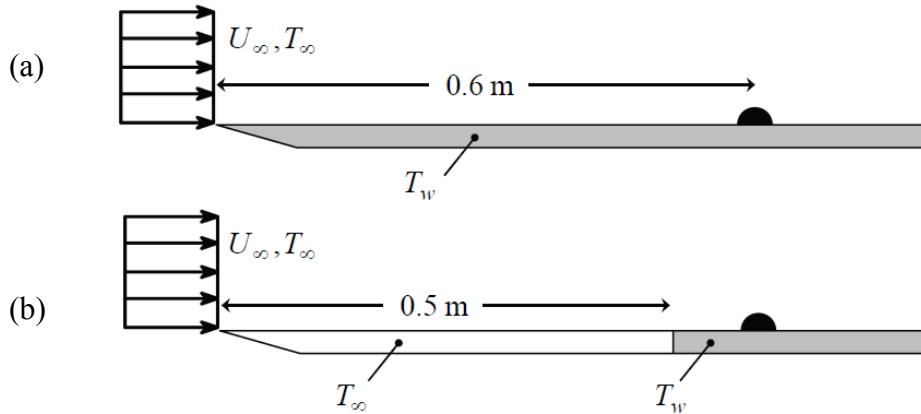


Figure 2.5: Single roughness element on a flat plate with (a) isothermal heating and (b) unheated starting length [16]

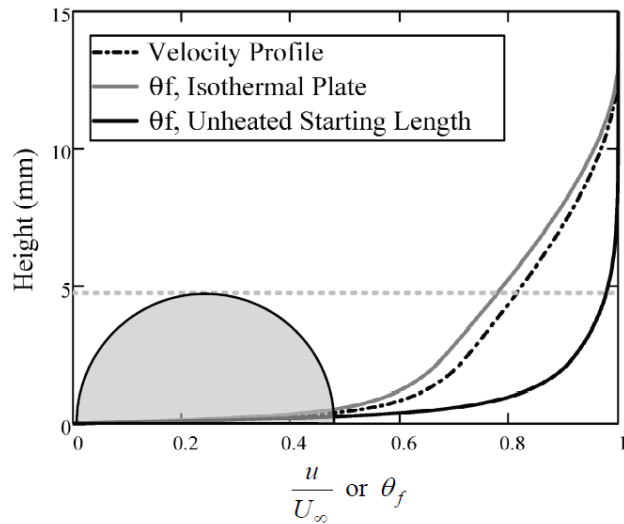


Figure 2.6: Viscous and thermal boundary layers for the scenarios of Figure 2.5 [16]

It is also important to consider the effects of roughness element thermal conductivity on convective heat transfer. Mart [33] constructed two identical surface roughness distributions using 9.53 mm diameter hemispherical elements arranged in a

sparse hexagonal pattern with a spacing-to-diameter ratio of 2.099. The only difference between the distributions was the material used in the construction of the elements; one was made of ABS plastic and the other was made of aluminum. The distributions were tested using the same flow and heating conditions. A set of results from Mart [33] is shown in Figure 2.7, comparing the temperature distributions for each distribution. The Biot number and thermal conductivity are also indicated for each distribution.

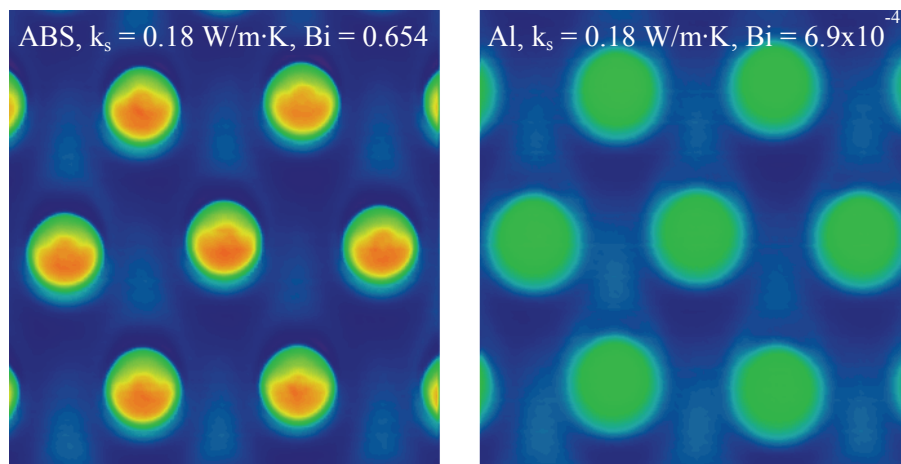


Figure 2.7: Comparison of ABS and aluminum roughness element temperature distributions from Mart [33]

Due to the much higher thermal conductivity of the aluminum elements their Biot number is much lower (by three orders of magnitude) than the ABS elements. As a result, there is no appreciable temperature gradient along the aluminum roughness element height. The decreased resistance to internal conduction also leads to higher overall surface temperatures on the aluminum elements to drive convection; therefore, the convective heat transfer is about 5% higher than the ABS surface.

There are several prevalent methods used to model the effects of surface roughness. The first is the sand-grain equivalent roughness model, proposed by

Schlichting [14]. While investigating the effects of various types of surface roughness over a flat plate in turbulent flow, Schlichting devised a way to generalize his findings through the use of a sand-grain equivalent roughness height [14]. This sand-grain height was determined by relating the skin friction for the roughness of interest to the results of a test case from Nikuradse [17], who performed studies on the effects of surface roughness caused by sand-grains on internal pipe flow. Although simplistic, this model is still widely used today.

Another prevalent roughness model is the discrete element model (DEM), also proposed by Schlichting [14]. This model considers the total drag on a rough surface as the sum of the smooth surface drag and the form drag on each of the individual elements. This argument can be extended to the convective heat transfer effects as well. An improvement to the DEM was suggested by McClain et al. [18] in the form of the extended surface discrete element model (ES-DEM). This model goes further than the DEM by treating the roughness elements as extended surfaces (i.e. fins). The ES-DEM allows additional heat transfer effects to be captured, such as the temperature variations along the roughness element height [18].

The final prevalent method to model the effects of surface roughness is through the use of grid-resolved CFD simulations. This approach can be problematic in its implementation due to the presence of different length scales which influence the computational model (model length scale, roughness length scale, and boundary layer length scale) [19]. Once a computational model has been validated against empirical data, it can be used to run simulations across a range of values, saving on experimental costs. However, as with any CFD simulation, increasing levels of complexity will lead to

more computationally expensive simulations in the form of computational storage requirements and simulation runtime.

Airfoils

As air flows around an airfoil its shape causes flow acceleration over the top surface and flow deceleration over the bottom surface. This velocity change creates a negative pressure region over the top surface of the airfoil and a positive pressure region over the bottom surface. Like the flat plate, the airfoil will also develop shear stresses at the wall due to the viscous boundary layer. The coupling of the forces from pressure and shear stress yields the resultant forces of lift and drag. A basic illustration of these forces is provided in Figure 2.8.

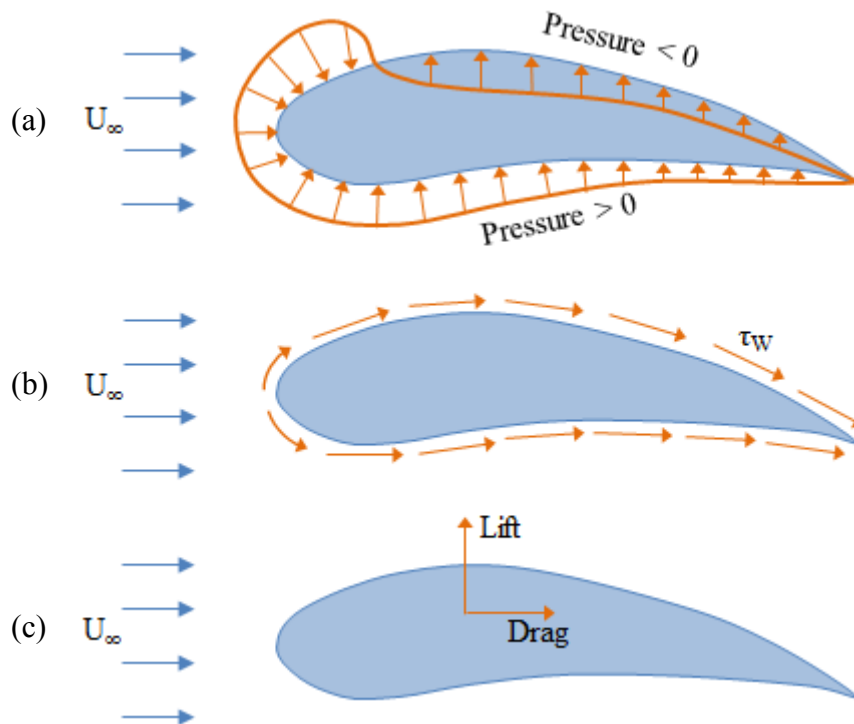


Figure 2.8: Forces on an airfoil (a) pressure, (b) viscosity, and (c) resultant

Unlike the flat plate boundary layer, the boundary layer that forms on the surface of an airfoil can eventually reach a point at which it will separate from the airfoil surface. This is due to the presence of an increasing adverse pressure gradient which will decrease the fluid momentum as it moves across the airfoil surface. The separation point is the location where the velocity gradient at the wall is zero. After the separation point a separation bubble (or wake region) will develop on the airfoil surface. Figure 2.9 illustrates the process of flow separation. As with the flat plate, surface roughness will affect the boundary layer development along an airfoil surface.

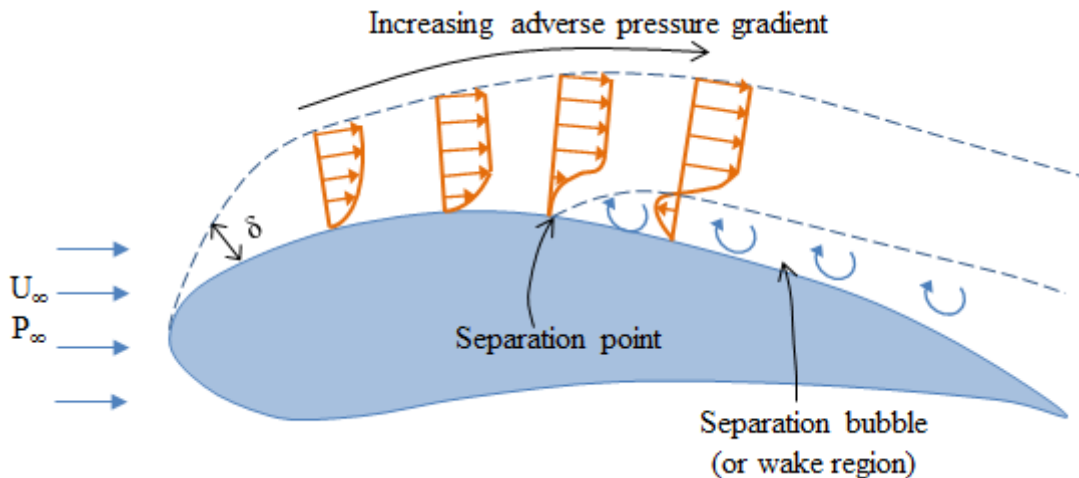


Figure 2.9: Boundary layer separation due to an adverse pressure gradient (not to scale)

The convective heat transfer coefficient for complex objects (such as an airfoil) must be determined experimentally; however, performing heat transfer studies on an airfoil can be difficult. Cylinders and flat plates are often studied instead to gain insight on airfoil heat transfer, with cylinders modeling the stagnation region and flat plates modeling the regions downstream of the stagnation point [21]. These studies are useful for several reasons. First, these models are a much simpler physical representation of the airfoil and are easier to manufacture. Another advantage is that cylinders and flat plates

have been studied extensively in fluids and heat transfer. This provides a wealth of data for comparison and validation. Once the simpler cases have been studied, complexity can be added as needed.

Ice Roughness Background

Ice roughness forms during the initial stages of icing before significant accretion has occurred. The presence of ice roughness on an airfoil will affect boundary layer development, and therefore skin friction and convective heat transfer. Its formation mechanism is through droplet impingement and coalescence on the icing surface. An ice roughness distribution is made up of many ice roughness elements, which vary in both size and spacing along the surface. Initially, ice roughness forms away from the stagnation region due to heating of the droplets caused by flow stagnation. This results in a symmetric smooth-zone about the stagnation point which transitions to roughness. Figure 2.10 presents a) a basic illustration of ice roughness terminology and b) an example of an ice roughness element distribution.

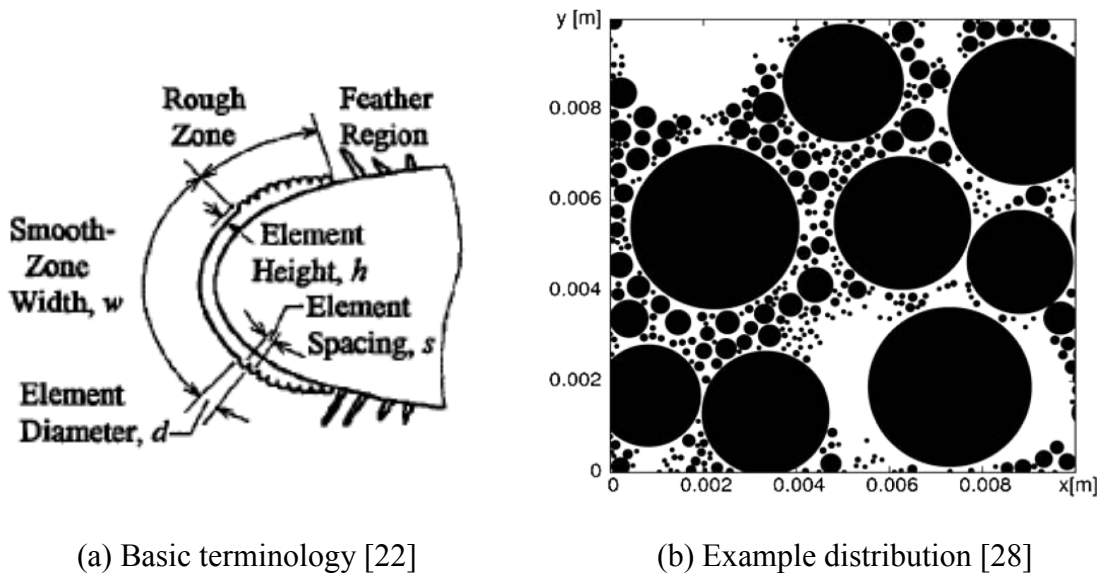
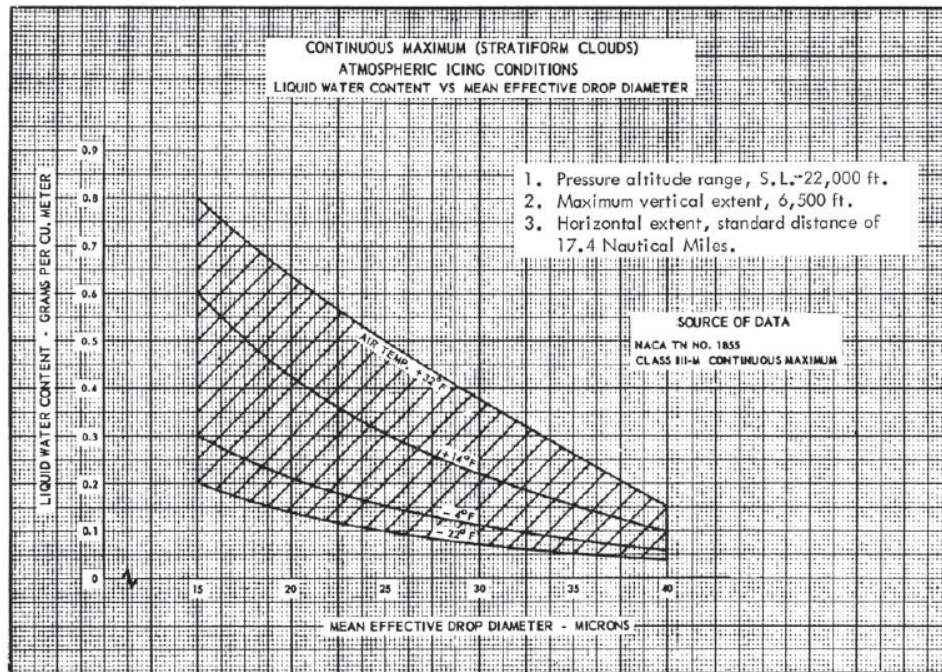
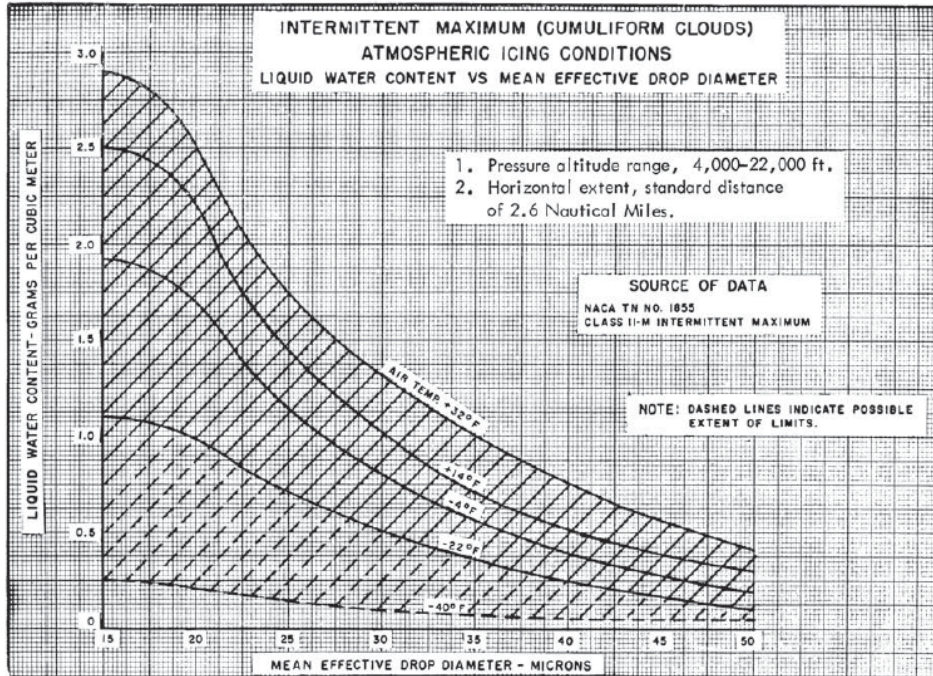


Figure 2.10: Ice roughness examples

Many atmospheric factors can influence the formation of ice roughness. Among these factors are the liquid water content and median volumetric diameter of an icing cloud. Liquid water content (LWC) is the mass of water droplets present in a unit volume of air. Higher values of LWC imply the need for more latent heat removal due to higher droplet density. Median volumetric diameter (MVD) is the diameter above and below which half of an icing cloud's volume (or mass) of droplets is contained [4]. For example, in an icing cloud with an MVD of 50 μm , half of the mass of water is contained in droplets having a diameter above 50 μm and the other half is below. MVD is the parameter most often used to describe the size of the droplets in an icing cloud. Figure 2.11 presents the Appendix C design envelopes for both continuous and intermittent exposure to icing conditions as a function of the MVD and LWC at varying air temperatures [6]. These envelopes present sets of icing conditions that an aircraft must be able to tolerate.



(a) Continuous exposure



(b) Intermittent exposure

Figure 2.11: Appendix C design envelopes [6]

Ice roughness formation is also impacted by the icing regime. Rime and glaze icing are the two main icing regimes. In rime icing, it is assumed that 100% of the impinging water droplets freeze on impact. This creates a white, opaque ice. In glaze icing, less than 100% of the impinging droplets freeze on impact. This leads to a layer of liquid water runback on the icing surface and produces a clearer ice. Rime icing usually occurs at air temperatures at or below 0 °F and glaze icing occurs at air temperatures closer to 32 °F, with transitional or mixed icing occurring at intermediate temperatures [1]. Addy [1] and Vargas [8] note that the aerodynamic degradation of an airfoil is more pronounced in the glaze icing regime than in the rime icing regime. This is because the ice shapes produced in each regime are different, possibly as a consequence of the much larger roughness elements that initially form in glaze icing [9].

The Messinger Model for Aircraft Icing

To fully understand the role of ice roughness in icing heat transfer, the foundational aircraft icing model developed by Messinger in 1953 [24] must be examined. The basis for the Messinger model is an energy balance performed at the icing surface. The Messinger model considers energy losses from convection, evaporation, and sensible cooling by impinging droplets. Energy gains are considered from latent heat release, viscous heating, and the kinetic energy of impinging droplet impacts. Figure 2.12 shows Messinger's representation of these energy transfer modes for a generic airfoil icing scenario.

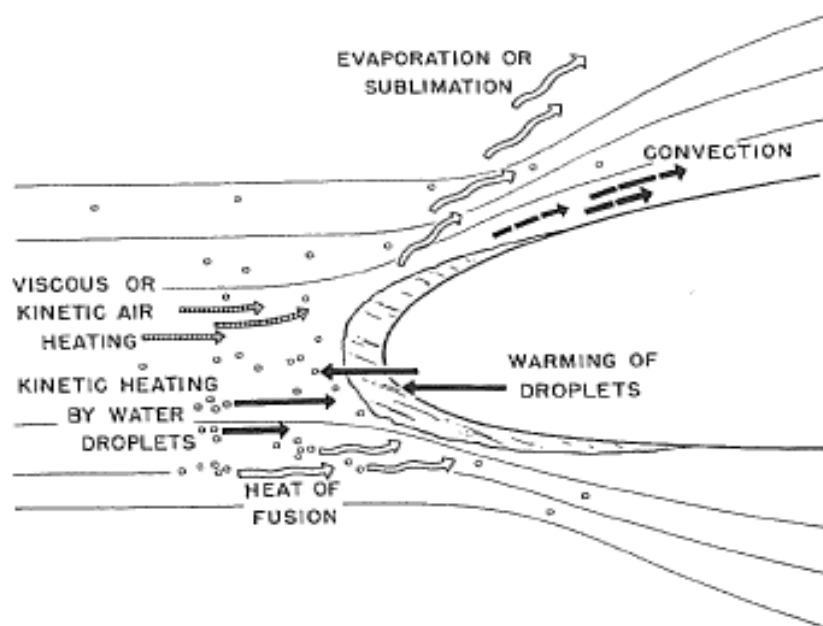


Figure 2.12: Modes of energy transfer on a generic airfoil [24]

Messinger also introduced the concept of the freezing fraction. The freezing fraction is a dimensionless parameter which is defined as the percentage of impinging liquid which freezes on an icing surface upon impact [24]. Its value is limited between zero and one. When the freezing fraction is equal to one all droplets freeze on impact

(i.e. rime icing). As the freezing fraction approaches zero fewer droplets freeze on impact, leading to water runback along the airfoil surface (i.e. glaze icing). Although several mechanisms for heat transfer exist on an airfoil, the prediction of ice growth rates and ice shape formation is most highly sensitive to convective heat transfer values since this is the predominant mode of heat transfer in icing [25].

The form of the Messinger model implemented in NASA's Lewis Ice Accretion Code, or LEWICE (currently in version 2.2.2), is shown in Eq. (2.13).

$$-(k_{\varphi} \frac{\partial T}{\partial \varphi})_{\varphi=0} = q''_C + q''_E - q''_{KE} - q''_L \pm q''_S \quad (2.13)$$

In this form evaporation is represented by q''_E , kinetic heating is represented by q''_{KE} , latent heat gain is represented by q''_L , and sensible cooling is represented by q''_S . The convective and viscous heating terms are combined and represented by q''_C , which is a net convective heat loss term. The thermal conductivity of the icing surface is represented by k_{φ} . Messinger [24] developed an algorithm for determining the freezing fraction given the icing conditions; this is the same basic algorithm used in LEWICE [7]. By solving Eq. (2.12) for the surface temperature distribution ($\partial T/\partial \varphi$) at the icing surface ($\varphi = 0$) and employing the algorithm of Messinger, the freezing fraction on a surface can be calculated. Using this information, along with other icing parameters, LEWICE makes a prediction of the ice growth and liquid water runback for each discretized control volume along the surface of an airfoil.

Ice Roughness in LEWICE

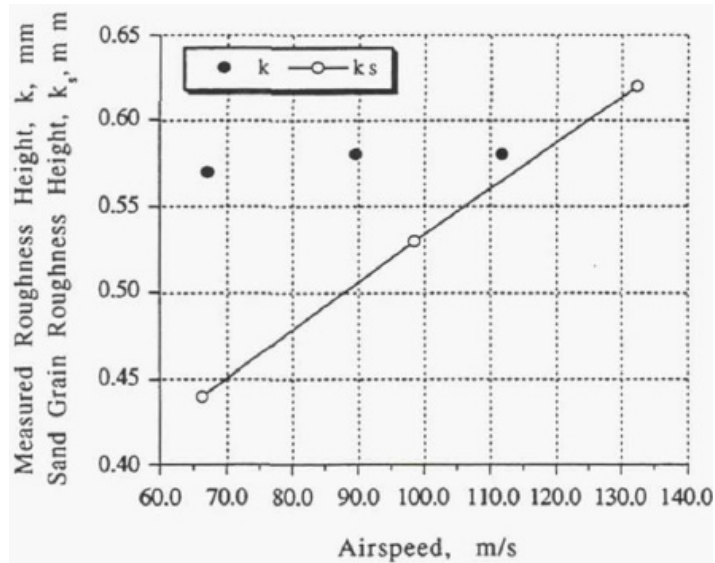
In LEWICE, an estimate of ice roughness height is established based on the sand-grain equivalent model [7]. Convective heat transfer coefficients are then determined

from an integral boundary layer calculation, which uses the equivalent sand-grain roughness height [7]. This information is then used to perform the Messinger heat balance at the icing surface [22,23]. The equivalent sand-grain roughness height (x_k) is determined by the empirical correlation shown in Eq. (2.14) [7].

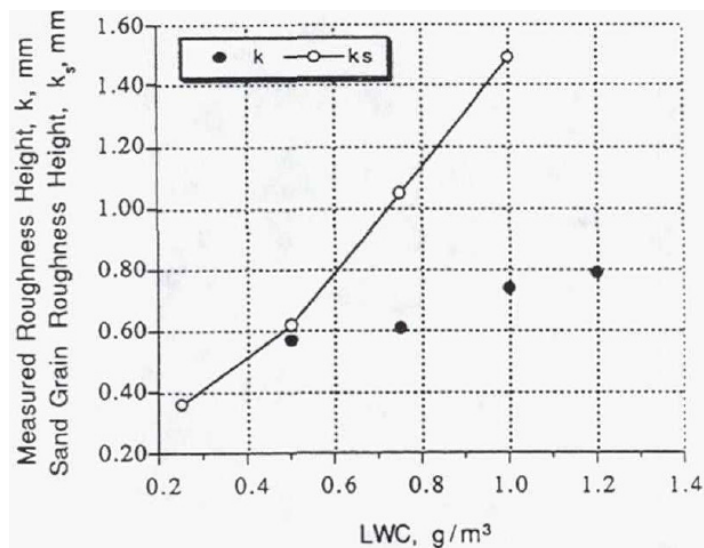
$$x_k = \frac{1}{2} \sqrt{0.15 + \frac{0.3}{N_{f,stag}}} \quad (2.14)$$

This correlation was determined from experimental measurements of roughness height as a function of the freezing fraction at the stagnation point ($N_{f,stag}$), which is calculated separately [7]. This correlation is used for all icing conditions.

This approach is suspect since sand-grain roughness is very different from realistic ice roughness in both size and distribution density [26]. Also recall that the sand-grain equivalent roughness model is based upon matching skin friction values and does not account for convective heat transfer effects. Although some relationship exists between skin friction and convective heat transfer through the Reynolds analogy, this does not mean that the sand-grain model is well suited to predict both parameters accurately [27]. The correlation in Eq. (2.14) is also very simplistic in its use of only one variable to estimate the roughness height for the entire range of icing conditions. Shin [26] performed comparisons of ice roughness height measured on an airfoil in the NASA Lewis Icing Research Tunnel (IRT) and the sand-grain height from LEWICE with matching icing conditions. He found that the predictions did a poor job of capturing roughness formation trends and magnitudes. Figure 2.13 shows comparisons of measured roughness versus sand-grain roughness as a function of (a) airspeed and (b) LWC.



(a) Roughness height versus airspeed



(b) Roughness height versus LWC

Figure 2.13: Comparison of measured and predicted roughness height [26]

Since convective heat transfer is so closely coupled to ice roughness, a change in the ice roughness characteristics (element size, element spacing, etc.) will drastically impact the convective heat transfer from a surface. When sparse models, like the sand-grain equivalent roughness, are used to model ice roughness, convective heat transfer is

under-predicted [25]. LEWICE is limited in its capabilities to accurately predict ice accretion due, in part, to the use of simplified ice roughness models which are based upon empirical correlations [28]. When the ice roughness parameter is varied in LEWICE different ice shapes and sizes are predicted [22].

In studying ice formation on swept-wing surfaces, Vargas [8] further demonstrated the need for better characterization of convective heat transfer from ice roughness in LEWICE. Results from a computational study using LEWICE were compared to ice shapes generated in the NASA IRT, with matched icing conditions. The ice shapes predicted computationally did not match well with the experimental results. The roughness parameter was arbitrarily varied to give better agreement between the results. Further, tests of lift and drag on the experimental ice shapes showed that LEWICE did not predict the full impact of the aerodynamic losses due to poor ice shape prediction.

LEWICE typically predicts ice shapes resulting from rime icing better than those from glaze icing [8,29]. This is because the glaze icing regime creates a three-phase condition at the icing surface, with frozen ice, liquid water runback, and impinging droplets. This leads to more complicated ice accretion mechanisms than exist in rime icing. It is also related to the much greater convective heat transfer from glaze ice roughness when compared to rime ice roughness due to the formation of larger roughness elements [9], leading to a larger magnitude of error in the predictions.

Improvements in Ice Roughness Modeling

The developers of LEWICE are quick to point out that improvements to the current ice roughness models are required; the modular nature of the code would make

such changes relatively simple in future versions [7]. Several prior studies have been undertaken to better understand the nature and effects of ice roughness in an attempt to improve the predictive models used in icing codes.

Anderson et al. [23] and Shin [26] measured and reported descriptive surface statistics for ice roughness distributions generated on a NACA 0012 airfoil (21" chord length) in the NASA IRT. After the ice roughness was generated, photographs were taken of the airfoil surface and optical techniques were used to measure the size and spacing of the roughness elements. The data of Anderson et al. [23] and Shin [26] is useful because it provides a comprehensive representation of ice roughness characteristics for a large range of Appendix C conditions.

Poinsatte et al. [21] investigated the effects of ice roughness on convective heat transfer from a NACA 0012 airfoil. Although these tests were performed on a real airfoil surface, they used a simplistic characterization of ice roughness. The roughness tested in these experiments was comprised of sparsely distributed, constant diameter elements, which is not characteristic of realistic ice roughness. Similar studies using non-realistic ice roughness showed congruent results [30,31]. Figure 2.14 shows two of the roughness distributions tested by Poinsatte et al. [21].

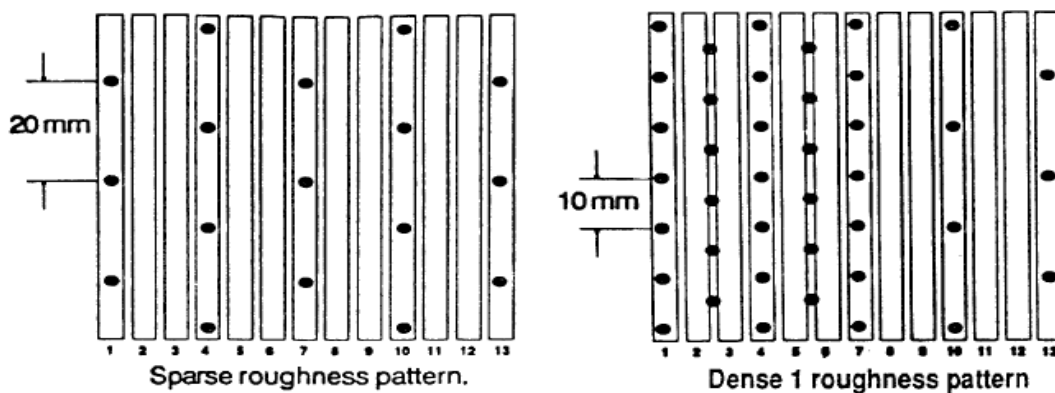


Figure 2.14: Simplistic ice roughness distributions used by Poinsatte et al. [21]

Dunkhan and Van Fossen [25] utilized more realistic ice roughness distributions in their convective heat transfer tests. Ice roughness was generated on an airfoil in the NASA IRT and a casting technique was used to manufacture a testable copy. Compared to Poinatte et al. [21] they found much higher heat transfer values. The higher convective heat transfer values were due, in part, to the use of a more realistic representation of ice roughness than Poinatte et al. [21]. Additionally, Bons [27] found that the use of non-realistic, simplistically distributed roughness models creates biases in convective heat transfer data not found when using more realistic distributions. Using realistic roughness allows the effects of diverse element interaction on boundary layer development and convective heat transfer to be captured [27].

Croce et al. [28] developed a more sophisticated ice roughness model which is used by the icing code FENSAP-ICE. The predictive model for ice roughness in FENSAP-ICE utilizes a Lagrangian technique of roughness evolution in order to reflect the physics of how realistic ice roughness is developed; that is, individual droplets are tracked as they impinge the surface and coalesce with other elements. The basis for the droplet coalescence model is based upon the observation that the droplet patterns formed during the early stages of icing are similar to those formed during the condensation of dew, as described by Beysens [32]. Although FENSAP-ICE has a more sophisticated method for modeling ice roughness formation, it still relies on correlations to obtain convective heat transfer data; therefore, the results are comparable to LEWICE.

Based on the above works, the need for an investigation of the convective heat transfer behavior of realistic ice roughness distributions is clear. In this study, a Lagrangian technique similar to that of Croce et al. [28] will be used to generate realistic

Appendix C ice roughness distributions based on the surface statistics provided by Anderson et al. [23] and Shin [26]. The convective heat transfer from these distributions can then be studied, using a flat plate to model a portion of a NACA 0012 airfoil. This process is detailed in Chapter Three.

CHAPTER THREE

Materials and Methodology

To investigate the convective heat transfer behavior of realistic ice roughness element distributions, a series of experiments was performed. These experiments required the construction of several apparatuses. This chapter describes the processes used in the design and construction of the experimental apparatuses, as well as the experimental procedures and instrumentation.

Instrumented Test Plate

The test plate was designed to model the region immediately downstream from the stagnation point of the 21" chord length NACA 0012 airfoil used in the experiments of Anderson et al. [23]. The roughness and test plate dimensions were chosen to match the Reynolds number along the leading edge of the airfoil. These dimensions were scaled up by a factor of ten so that the length of the test plate surface corresponded to the first 3.648" of the airfoil. Applying this scaling, the test plate exhibits Reynolds numbers matched to the first 17.4% of the airfoil when the test velocity is reduced by a factor of ten. This scaling is appropriate since ice roughness formation is typically limited to the region closest to the leading edge of an airfoil.

Test Plate Design

Figure 3.1 shows a conceptual model of the test plate used in this investigation. The plate includes an integrated floor for installation in a wind tunnel test section.

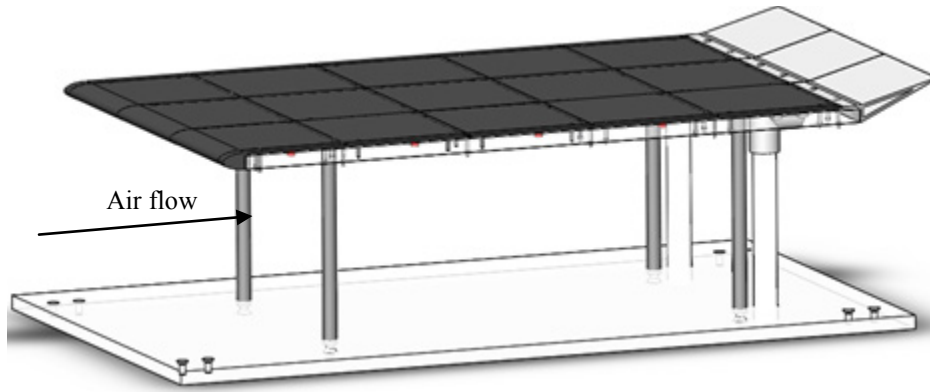


Figure 3.1: Conceptual design for the test plate

A design similar to that of Mart [33] was implemented, with several key improvements. Mart [33] affixed individual roughness elements directly onto the test plate, requiring the construction of a new test plate for each surface roughness tested. The current design eliminates this issue through the use of interchangeable surfaces installed on top of the main plate. Mart [33] also had one continuous heated section spanning the length of the plate in the flow direction; the current design has five independent heated sections. This allows for the option of varying the heat flux along the plate. Each heated section consisted of a gold deposited Mylar film heater powered by two copper electrodes which were connected to power supplies via terminal posts on the underside of the plate. Gold deposited Mylar film was used because it provides uniform heating across its surface area, allowing for the assumption of a constant heat flux boundary condition in each heated section.

Figure 3.2 shows a side view of the test plate model. Figure 3.3 shows an isometric view of the test plate model with some of the interchangeable surface plates removed to show otherwise hidden features. The test plate has two electrical junction boxes connected to PVC conduit to allow the substantial amount of instrumentation and

power wiring to run out of the wind tunnel through the bottom of the test section floor. Flow features of the test plate include a bullnose on the leading edge and a rigid flap on the trailing edge. The bullnose was added so that the test plate created a minimal flow disturbance in the wind tunnel. The flap was added to account for the blockage on the bottom of the plate due to the instrumentation and piping. This prevented preferential flow separation from the top of the plate by accounting for the frontal area of the blockages. The thermocouple channels on the top surface of the Plexiglas plate were used to install subsurface thermocouples, which monitored the heat loss through the test plate.

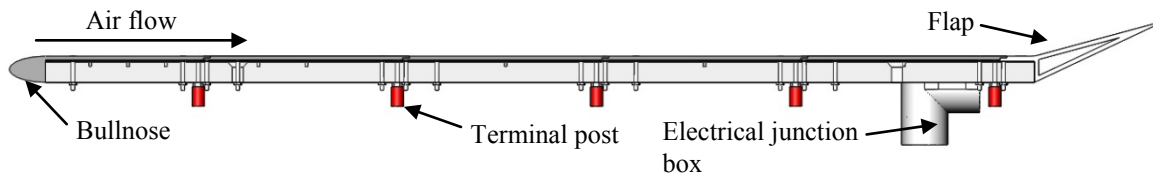


Figure 3.2: Side view of instrumented test plate model

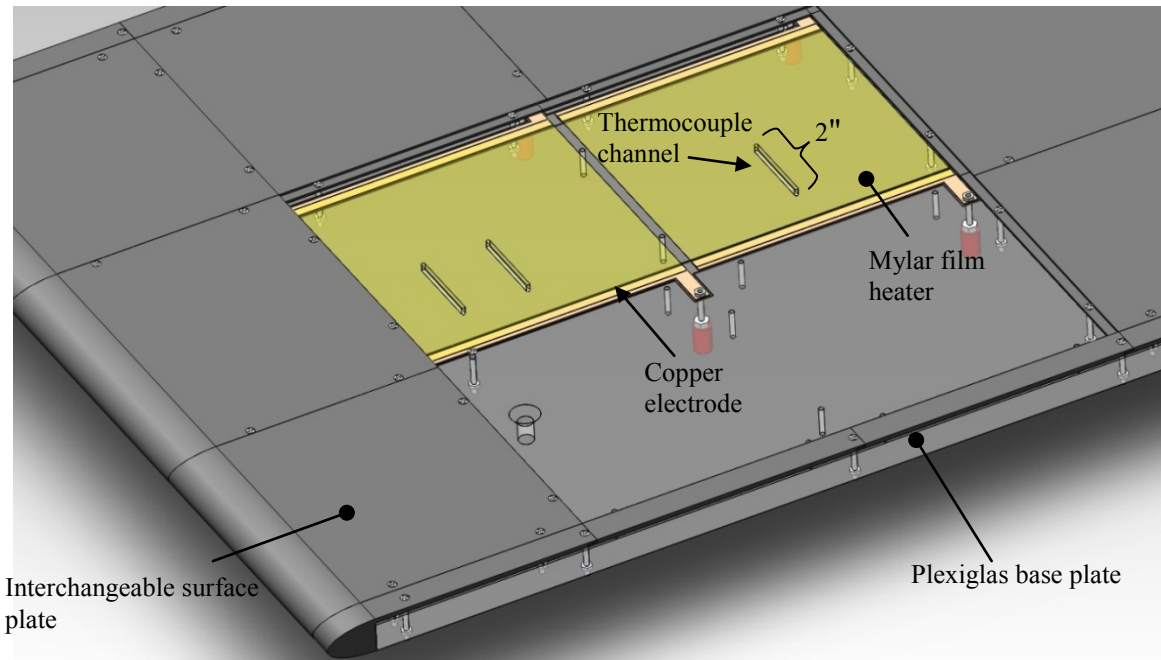


Figure 3.3: Isometric view of test plate with hidden features shown

Figure 3.4 shows the coordinate system and naming convention for the interchangeable surface plates. Each roughness surface consisted of 25 individual interlocking plates. The x-coordinate origin starts at the apex of the bullnose, wraps around the bullnose curve, and continues straight down the plate in the flow direction. The naming convention for the plates is such that there are five rows (A to E) and five columns (0 to 4); for example, the middle plate would be identified as C2. The heated sections are contained in the “C” row and are referred to simply as heated sections 0-4 going forward. The locations of the Mylar film heaters are also detailed in Figure 3.4, as indicated by the hatched areas. A 0.25" gap was required between each heated section to allow for through holes on the Plexiglas surface. The effect of these gaps was considered to be minimal due to their relatively small size. Due to the bullnose, there was an unheated starting length of 1.7285". The holes seen in this figure are the screw holes used to affix the surface plates to the Plexiglas.

Thermocouples were added to the center of each of the five heated sections to characterize the heat losses experienced during steady state testing. One thermocouple was installed in a channel just below the top of the Plexiglas surface and one was installed directly underneath, on the underside of the Plexiglas. Three additional thermocouple pairs were installed in the first two heated sections to identify any longitudinal conduction in the flow direction. The locations of these eight thermocouple pairs are identified in Figure 3.4. The measurement stations are numbered according to their heated section (0-4), with letters used to differentiate sections with multiple stations. Figure 3.20 details the x-locations of these thermocouple pairs.

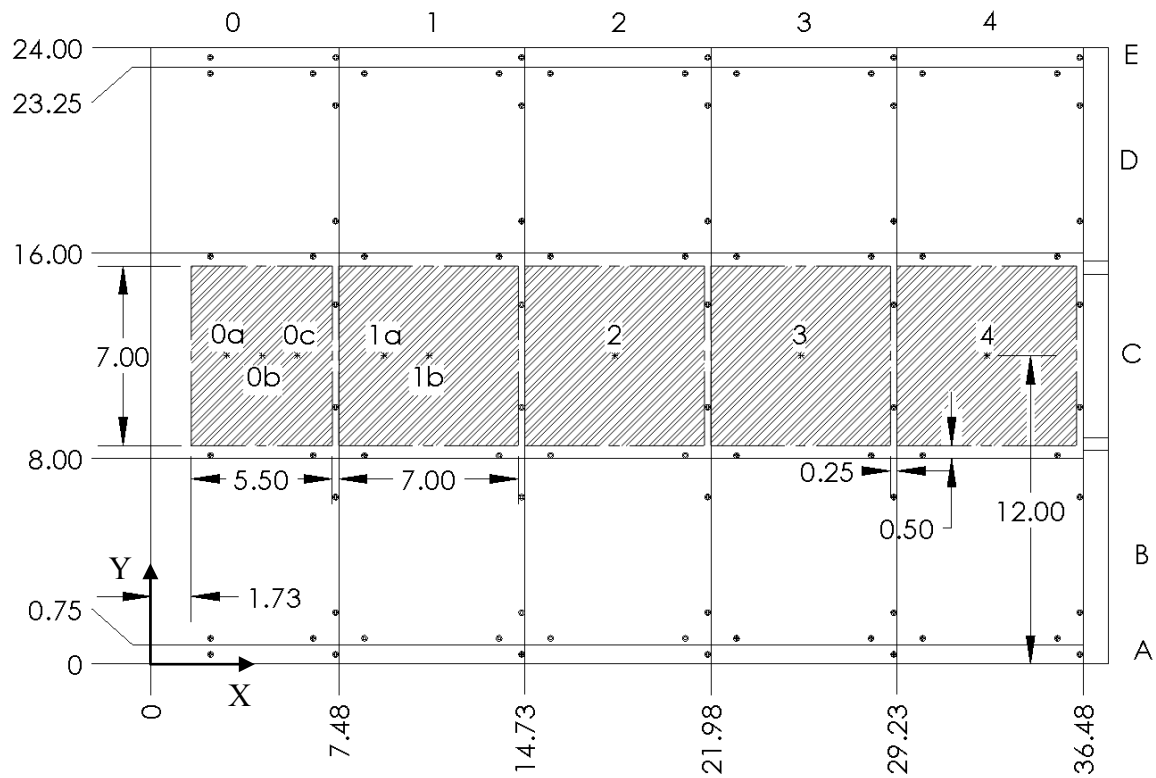


Figure 3.4: Surface plate grid and heated sections, dimensions are in inches

Required Tools and Materials

The special tools and materials required to construct the instrumented test plate are listed below:

1. 24" x 36" x 0.75" Plexiglas plate, for test plate
2. 25.5" x 43" x 0.75" Plexiglas plate, for test section floor
3. CPFilms FM gold deposited Mylar film, 8" wide by 0.0073" thick roll
4. Type K thermocouple wire
5. Self-adhesive Type K thermocouples
6. Electrical terminal posts
7. Single strand insulated copper wire, 22 gauge
8. Single strand insulated copper wire, 14 gauge

9. 12" x 12" x 0.035" copper sheet
10. 3M Super 77 spray adhesive
11. 3M Super 33 electrical tape
12. Loctite super glue (cyanoacrylate)
13. Loctite two-part plastic epoxy
14. SPI high-purity conductive silver paint
15. 80/20 Inc. framing, various sizes and lengths
16. 0.75" steel tube, four 12" sections
17. Schedule 40 PVC pipe, 1" diameter

Commonly available supplies are not included on this list.

Initial Test Plate Machining

Using a set of the interchangeable surface plates as a template (with a hand-drawn grid as additional verification) the 52 holes used to affix the surface plates were marked on the Plexiglas, which were then drilled using a drill press. Next, a meter stick and combination square were used to mark the tool paths for the channels used to install the subsurface thermocouples and copper electrode strips. A high speed handheld router with a 1/2" diameter straight bit was used to machine the copper electrode channels to a depth of 0.035". A 1/8" diameter straight bit was then used to machine the thermocouple channels to a depth of 1/8" on the top side of the plate. Holes were drilled at the far end of each thermocouple channel to provide an outlet for the thermocouple wires. Holes were also drilled in the copper strip channels to allow for connection of the terminal posts through the bottom of the plate. The test plate was then affixed to the wind tunnel floor

via four steel legs. Figure 3.5 shows the test plate after initial machining and attachment to the floor (obscured by the black felt sheet).



Figure 3.5: Plexiglas test plate after initial machining

Subsurface Thermocouple Installation

To characterize the heat loss through the Plexiglas at each heated section, a thermocouple was embedded into each of the eight machined channels and covered in epoxy. The thermal effects of the epoxy on the temperature readings was considered to be minimal since the epoxy thermal conductivity was higher than that of the Plexiglas. After preparing the thermocouples, the following installation procedure was used:

1. A thermocouple was placed into each channel through the hole in the bottom of the plate.
2. A large quantity of Loctite two-part plastic epoxy was mixed inside of a plastic sandwich bag. One corner of the bag was clipped to use as a hole to smoothly squeeze epoxy into the channels.

3. Working quickly to avoid letting the epoxy set, each thermocouple was lifted as its channel was filled with epoxy. The thermocouple was then pressed back into its channel using a flat wooden stick. The thermocouple beads were positioned such that they were in the centerline of the plate and as close to the Plexiglas surface as possible. This placement further minimized any effect of the epoxy on the temperature reading.
4. After allowing the epoxy to set for two days, a high speed sander was used to remove the excess epoxy and level the channels to the Plexiglas surface. Additionally, the entire middle section of the test plate was sanded in order to roughen the surface in preparation for installation of the Mylar film. The roughened surface provided a better surface for adhesion of the Mylar film.

Heated Section Preparation

Using a sheet metal press and a band saw, ten copper electrodes were cut out of the raw copper plate. After deburring the edges and flattening the strips with a rubber mallet, a sheet metal punch was used to create the through hole for the terminal post connection. The copper strips were then aligned and affixed inside of the previously machined channels on the test plate using a generous application of super glue. After allowing the strips to set overnight, the terminal posts were installed. Figure 3.6 shows heated section 0 prior to the application of the Mylar film.

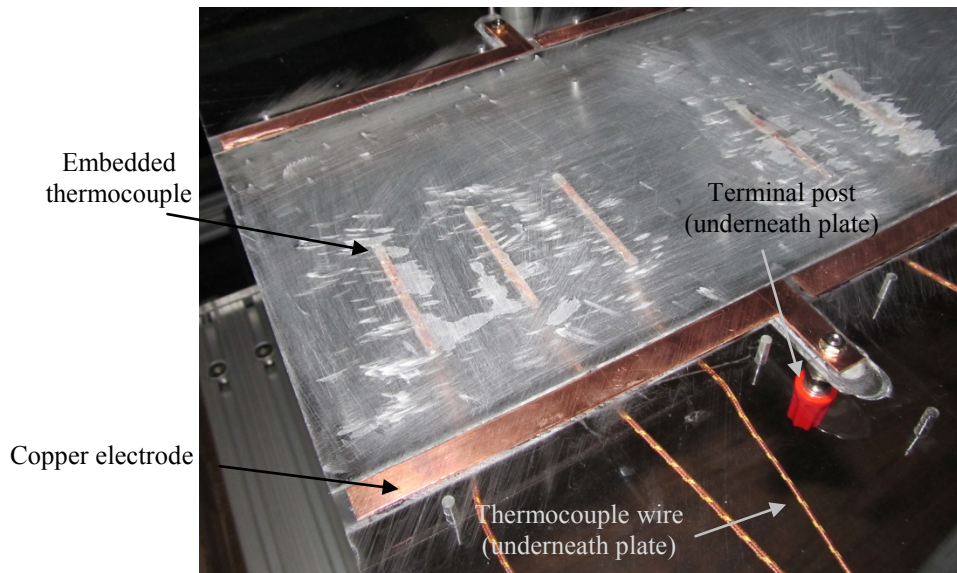


Figure 3.6: Heated section 0 prior to the Mylar film application

Gold Deposited Mylar Film Installation

Due to the fragile nature of the Mylar film, extreme caution was taken during this process. Latex gloves were worn at all times when handling the film and the gold deposited side was not touched, as this could damage the gold layer and create uneven heating. The following procedure was used to install the Mylar film:

1. Using an L-square ruler and marker, the bounding lines for the foil were marked on the test plate to guide the placement of the foil in later steps.
2. Newspaper and masking tape were used to protect the area outside of the heated section from the spray adhesive. Figure 3.7 shows a section partially prepared in this manner with the final target area for the adhesive outlined.

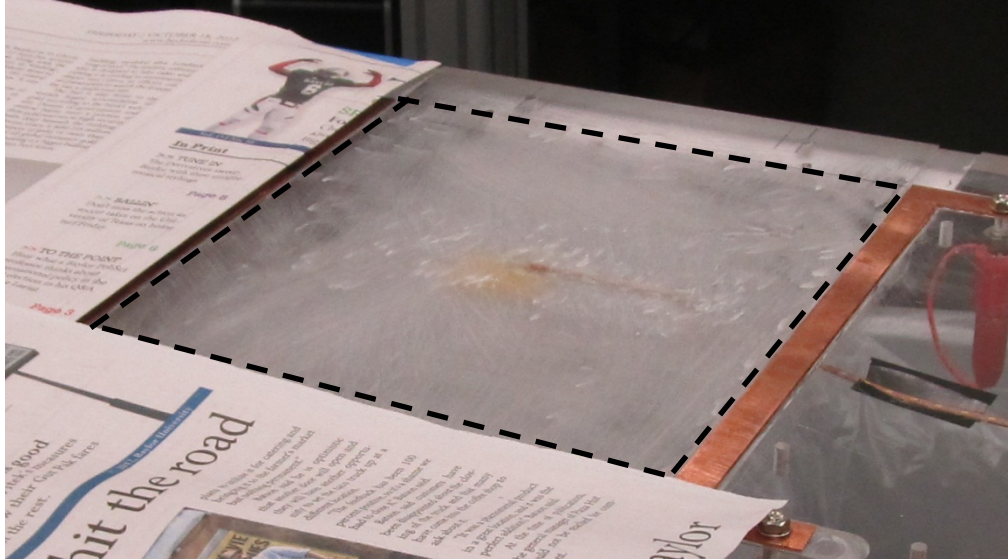


Figure 3.7: Heated section partially prepared for spray adhesive, target area outlined

3. The target surface was wiped down and blown with air to remove any residual debris.
4. An outline of the desired dimensions for the Mylar film was drawn onto a scrap piece of Plexiglas (which was used as a cutting surface) using an L-square ruler and marker. This outline was visible through the Mylar film and was used as the guideline for cutting.
5. While wearing latex gloves, the roll of Mylar film was carefully removed from its box and placed gold side up on the cutting surface. After properly aligning the Mylar film with the marker outline, masking tape was placed along the exposed edges to hold it in place. Figure 3.8 shows the Mylar film roll affixed to the cutting surface. The cutting guideline is highlighted by the dashed lines.

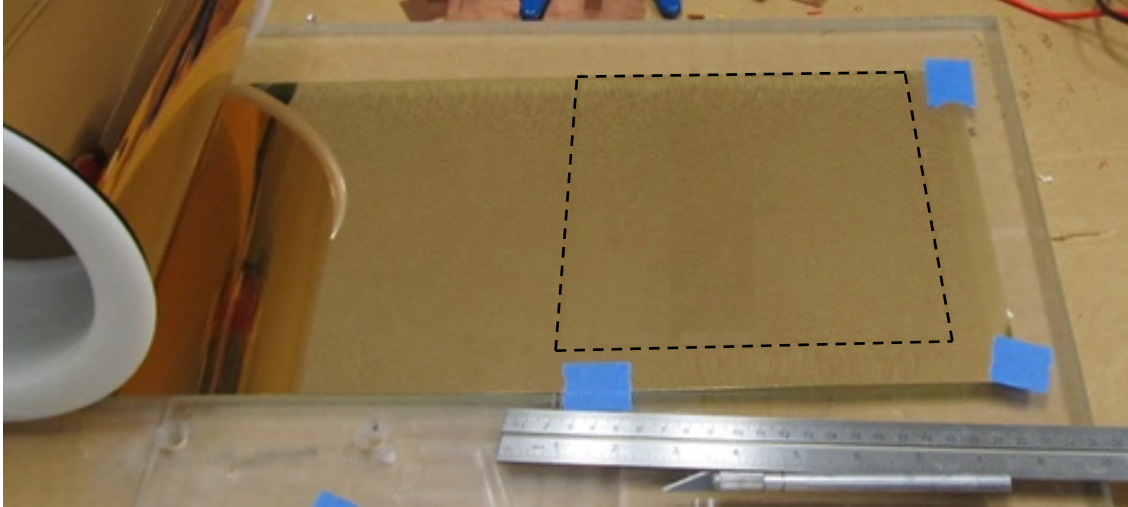


Figure 3.8: Mylar film prepared for cutting, cutting lines outlined

6. Working one edge at a time, a straight edge was placed along the marker line and an Exacto knife was used to perform the cut. The straight edge was always placed to the outside of the marker line to prevent damage to the final piece. This created about a one inch strip of waste material around each cut where the gold was touched and damaged.
7. After cutting the Mylar film, a generous layer of 3M Super 77 adhesive was applied to the previously prepared area on the test plate. Handling by the outer edges only, the cut Mylar film was carefully placed onto the test plate with the gold side down. A rubber brayer was then used to firmly affix the Mylar film and remove any air bubbles.
8. After allowing a day for the adhesive to set, the edges of the Mylar film were carefully lifted from the copper strips while a generous layer of conductive silver paint was applied. The silver paint reduced any contact resistance between the gold film and copper electrodes. Figure 3.9 shows a completed heated section after application of the silver paint.

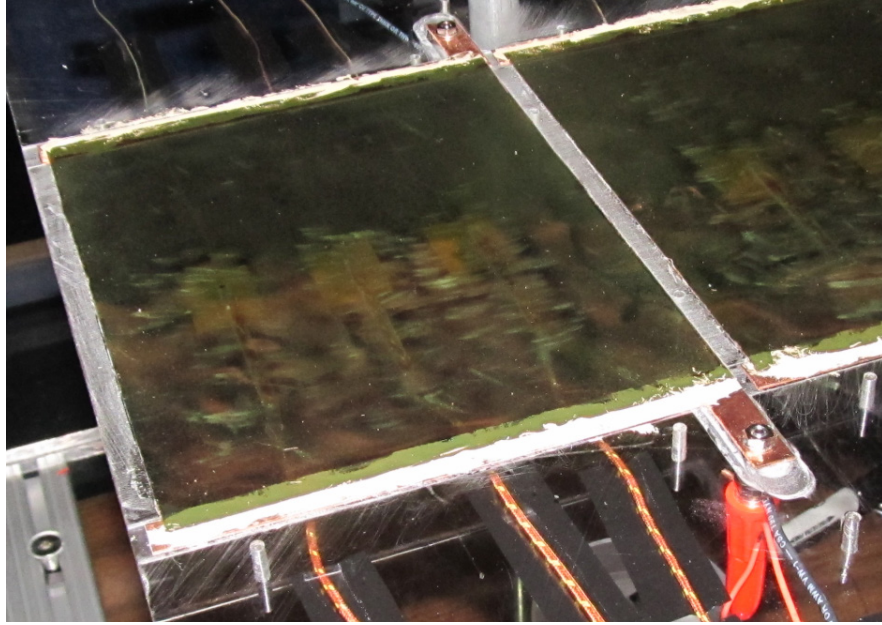


Figure 3.9: Completed heated section

Wiring

The final step in the construction of the test plate was to organize the power and instrumentation wiring. First, the PVC conduit and electrical junctions were attached to the test plate through the bottom of the test section floor. Next, 14 gauge wire was connected to the terminal connection of each terminal post to supply power to the heated sections. After tightening the terminal connections, banana plugs soldered to 22 gauge wire were connected to the bottom of each terminal post for voltage measurement. The wiring was then bound together and routed underneath the plate using electrical tape and wire supports. The wires were routed through one of the two PVC conduits and out of the wind tunnel test section. One conduit held the power supply (+), voltage measurement (+), and subsurface thermocouple wires; the other conduit held the power supply (-), voltage measurement (-), and underneath the plate thermocouple wires. Figure 3.10 shows the completed test plate prior to affixing the surface plates.

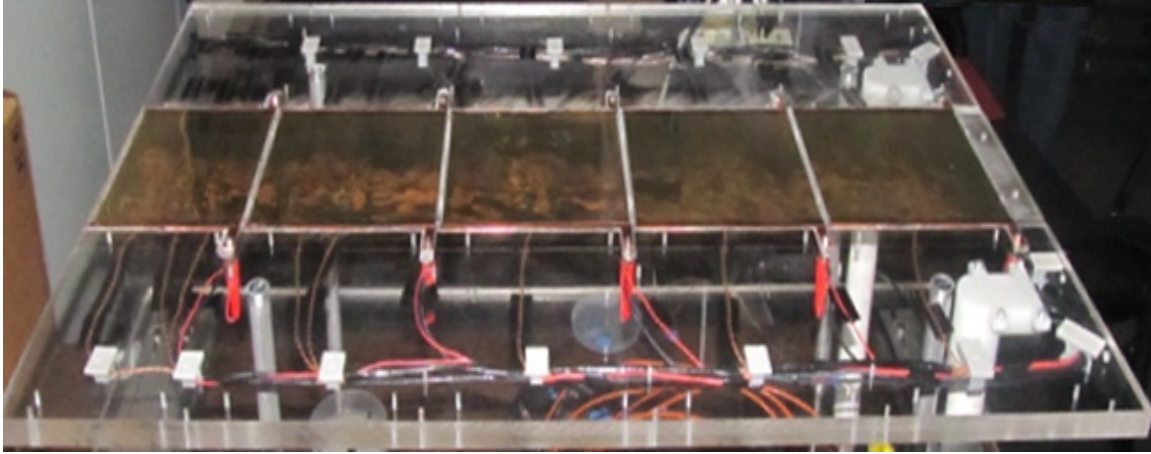


Figure 3.10: Completed instrumented test plate

Creation of Testable Ice Roughness

Lagrangian Droplet Simulator Development

The first step in the creation of realistic ice roughness distributions was the development of a Lagrangian droplet simulator which models the droplet impingement and coalescence processes. A Lagrangian droplet simulator which operates on the same basic principles as the droplet simulator described by Croce et al. [28] was programmed using Mathcad. The inputs required for the simulation are 1) the simulation area dimensions, 2) the impinging droplet diameter (which correlates to the MVD of the icing cloud), 3) the contact (or wetting) angle of the droplets on the surface, and 4) the number of droplets to impinge. After a droplet impinges on the surface it is referred to as an element. The output of the simulator is a data file which includes the final element location (x- and y-position) and size (radius and height). The basic algorithm used by the simulator is presented below:

- 1) The four required inputs are provided by the user. The program currently operates with a fixed impinging droplet diameter. The code could be modified to

- operate with a statistical distribution of impinging droplet diameters. For all simulations in the current investigation the contact angle was set to 90° , which yields hemispherical elements (i.e. radius is equal to the height).
- 2) The x-location and y-location for the droplet impingement is randomly selected within the simulation area.
 - 3) A check is made for droplet coalescence.
 - a) If the impinging droplet does not overlap with any existing elements, proceed to step 4.
 - b) If the impinging droplet does overlap with an existing element, perform the following coalescence subroutine:
 - i. Calculate the volume, radius, and height of the combined element. The center of the combined element is placed at the centroid of the original elements.
 - ii. Check if the newly formed element requires further coalescence. If so, return to step 3.b.i; if not, proceed to step 4.
 - 4) Return to step 1 until the desired number of droplets have impinged the surface.

An initial qualitative comparison to Croce et al. [28] is shown in Figure 3.11. This figure shows the number of elements and coverage fraction versus the number of impinged droplets (or time) for each simulator. The simulation run by Croce et al. [28] included a non-constant distribution of impinging droplet sizes, the mean droplet size was different, and the contact angle was different. Despite these differences in the simulation parameters, the qualitative comparison of the two simulations is encouraging. Both simulators exhibit two important features of realistic ice roughness formation. First, as

the number of impinging droplets increases the number of elements on the surface decreases. This is due to the coalescence of elements on the surface. Secondly, the coverage fraction of the surface approaches an asymptotic value of about 90% [28].

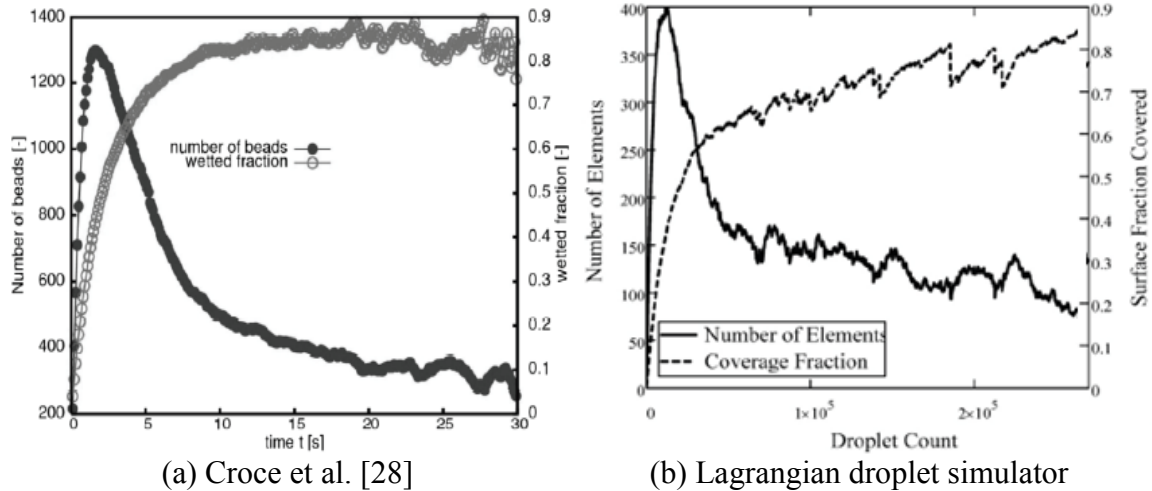


Figure 3.11: Comparison of simulator results

In the initial testing of the Lagrangian droplet simulator, a limitation of its usability was identified. For small impinging droplets, such as those found in Appendix C conditions, significant simulator runtimes (on the order of weeks) were required. To address the issue of long simulator runtimes, several simulations were run with different impinging droplet diameters. The results of the simulations indicated that following the initial surface coverage and after widespread coalescence had begun, the element diameter distribution on the surface becomes bimodal. The first mode corresponds to the impinging droplet size; the second mode represents the mean diameter of the elements that have coalesced multiple times. Figure 3.12 presents histograms of element diameter for a simulation with $170 \mu\text{m}$ droplets impinging a 1.5 cm by 1.5 cm area. The figure includes three histograms at increasing numbers of impinged droplets.

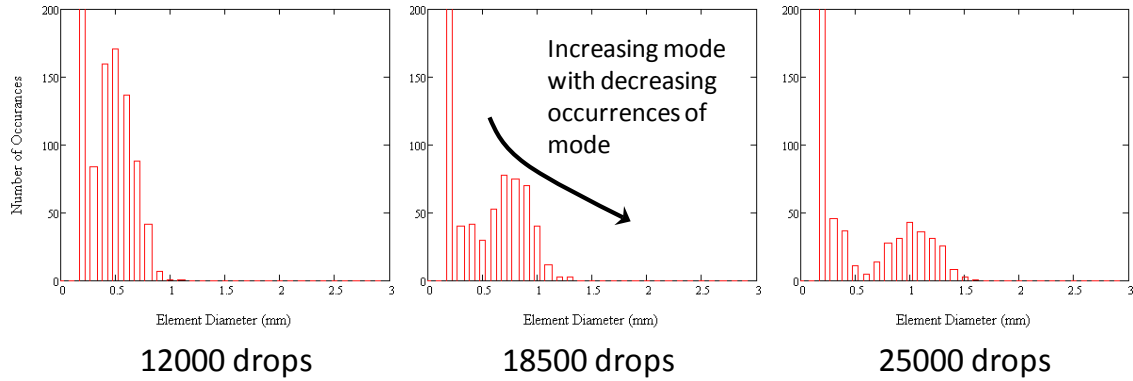


Figure 3.12: Histograms for three impinged droplet numbers showing the increasing second mode

Figure 3.12 illustrates that as the number of impinged droplets increases the second mode also increases, but the number of occurrences of the second mode decreases. This behavior was found to be independent of the initial droplet diameter. Consequently, any reasonable droplet size, about ten times smaller than the target average diameter, could be used to start a simulation. Thus, the runtime for the Lagrangian droplet simulator could be reduced by running at a droplet size larger than the MVD of the icing cloud, requiring less impinged droplets (i.e. time) to run to a target average diameter.

Matching to Reported Data

For the current investigation two simulated ice roughness surfaces were tested. Ice roughness data reported by Anderson et al. [23] and Shin [26] was used as a basis for the creation of these surfaces. The data of Shin [26] is used only to provide spacing-to-diameter values, which are lacking from the Anderson et al. [23] data. The spacing-to-diameter value was selected by using the mean diameter from Anderson et al. [23] and matching it as closely as possible to data from Shin [26]. The distributions chosen from the data are identified by Anderson et al. [23] as “5-29-96 Run 4” and “5-30-96 Run 1.”

These data sets were chosen because all of the relevant distribution statistics were reported along with histograms of the measured roughness element diameters. The selected cases also provided diversity in element size and accretion time. The “5-30-96 Run 1” surface also featured a smooth-zone width of 23.2 mm, allowing for investigation of the smooth to rough ice transition. For both of the selected cases the icing cloud MVD was about $30\ \mu\text{m}$ and the wind tunnel velocity was about 67 m/s. For “5-29-96 Run 4” the LWC was $0.6\ \text{g}/\text{m}^3$ and the accretion time was 94 s; for “5-30-96 Run 1” the LWC was $1.0\ \text{g}/\text{m}^3$ and the accretion time was 14 s. Images of the surfaces from the study are presented in Figure 3.13.

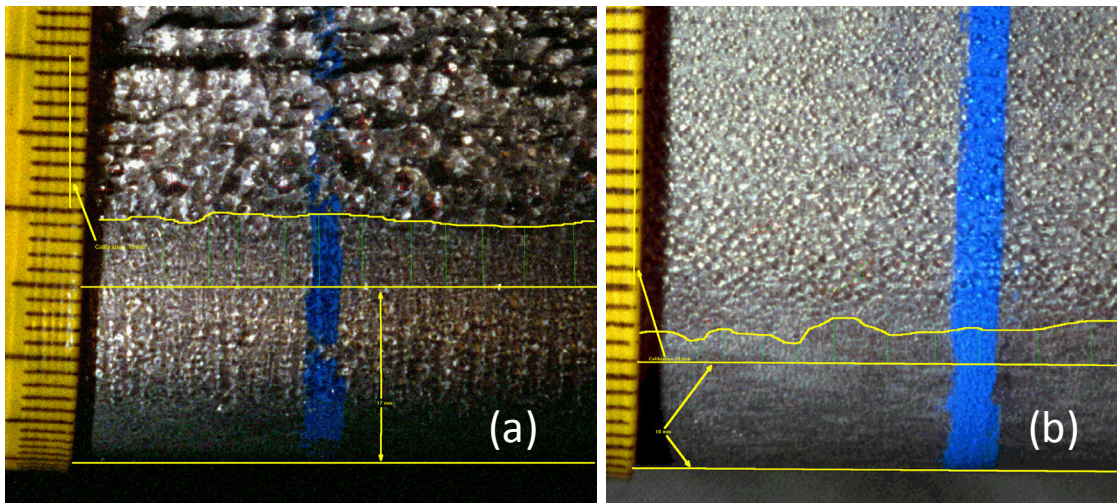


Figure 3.13: Images of roughness for cases (a) “5-29-96 Run 4” and (b) “5-30-96 Run 1” from the experiments of Anderson et al. [23]

The Lagrangian droplet simulator was run to match each case by starting with $170\ \mu\text{m}$ droplets impinging a 1.5 cm by 1.5 cm simulation area with a 90° contact angle, resulting in hemispherical elements ($H/D = 0.5$). This contact angle was appropriate for the cases selected since the reported height-to-diameter ratio for both was 0.515. The

simulations were run until the second mode of the distribution matched the reported average element diameter for each experimental data set.

Another limitation of the Lagrangian droplet simulator was that the distributions generated using the simulator differed from the target distributions in four key parameters: 1) distribution shape, 2) overall average element diameter, 3) diameter standard deviation, and 4) spacing-to-diameter ratio. The differences were not unexpected given that once a distribution of real ice roughness elements begins to freeze on an aircraft surface, element coalescence, which is the critical aspect of the Lagrangian simulator, essentially stops. Once coalescence stops, the elements grow in place by droplet impacts on the elements and freezing of water vapor on the element. Additionally, the simulator used a constant diameter for the impinging droplets.

To address the discrepancies in surface parameters, several data conditioning steps were applied. As previously mentioned, the simulated roughness distributions were bimodal. Since the experimentally measured distributions did not exhibit the first mode, this part of the distribution was truncated by removing the elements below the minimum probability density between the two modes. To adjust the simulated distribution to match the standard deviation of a measured surface, the element diameters of the simulated distribution were scaled. Eqn. (3.1) presents a method to linearly scale an element diameter (D_{old}) based on the original deviation from the mean ($D_{old} - D_{mean}$) by a linear factor (F_d) to yield a new diameter (D_{new}).

$$D_{new} = D_{mean} + F_d(D_{old} - D_{mean}) \quad (3.1)$$

Another important quantity to match was the simulation spacing-to-diameter ratio; however, there are several approaches to reporting spacing information. Two values of

spacing-to-diameter ratio were calculated: 1) the mean value of the minimum spacing of an element to its nearest neighbor divided by its diameter $((P/D)_{mean})$ and 2) the mean minimum spacing divided by the mean element diameter (P_{mean}/D_{mean}) . These are shown in Eqns. (3.2) and (3.3), respectively, where N_E represents the total number of elements, $P_{i,min}$ represents the minimum spacing of the i^{th} element in relation to all neighboring elements, and D_i is the diameter of the i^{th} element.

$$\left(\frac{P}{D}\right)_{mean} = \frac{1}{N_E} \sum_{i=1}^{N_E} \frac{P_{i,min}}{D_i} \quad (3.2)$$

$$\frac{P_{mean}}{D_{mean}} = \frac{\frac{1}{N_E} \sum_{i=1}^{N_E} P_{i,min}}{\frac{1}{N_E} \sum_{i=1}^{N_E} D_i} \quad (3.3)$$

To adjust the spacing-to-diameter ratio, the positions of the elements were scaled. The original position of each element (x_{old}, y_{old}) was scaled by a simple linear scaling factor (F_s) to yield a new position (x_{new}, y_{new}) . Eqns. (3.4) and (3.5) were used for this process.

$$x_{new} = F_s x_{old} \quad (3.4)$$

$$y_{new} = F_s y_{old} \quad (3.5)$$

Table 3.1 presents a comparison of the reported data for the “5-29-96 Run 4” case and the results of the Lagrangian simulation through each conditioning step. Figure 3.14 presents a visualization of the element distributions through each conditioning step; Figure 3.15 presents the histograms for the distributions shown in Figure 3.14.

Table 3.1: Comparison of unconditioned and conditioned simulator surface statistics to “5-29-96 Run 4” reported values

Parameter	Reported Data [23,26]	Unconditioned Simulator Data	Truncated	Truncated and Stretched	Truncated, Stretched, and Scaled
D_{mean} (mm)	0.936	0.583	1.037	1.037	1.037
S_E (mm)	0.372	0.410	0.254	0.254	0.381
$(P/D)_{\text{mean}}$	N/A	1.330	1.057	0.878	1.032
$P_{\text{mean}}/D_{\text{mean}}$	1.2	0.979	1.012	0.840	0.840
H/D	0.515	0.50	0.50	0.50	0.50

To adjust the simulated distributions to match the “5-29-96 Run 4” measurements, a truncation was performed at approximately 0.45 mm. The truncated distribution exhibited a mean value much closer to the measured distribution since the first mode does not exist in the experimental measurement and skews the results low. Matching the spacing-to-diameter value presented some difficulty. Shin [26] presents measurements of spacing-to-diameter ratios that approach 1.2 for cases similar to Anderson et al. [23]. However, Anderson et al. [23] qualitatively indicates that in almost all of the cases investigated the elements were “touching” their nearest neighbors. Figure 3.14(b) demonstrates that while the calculated spacing to diameter ratio is near unity for the truncated distribution, the elements are not touching. Given the appearance of the “5-29-96 Run 4” surface in Figure 3.13(a) and given the Anderson et al. [23] note, the truncated distribution was stretched (in this case shrunk) using a factor of 0.83, leaving the edges of the roughness elements touching. Finally, to match the standard roughness element diameter standard deviation, the distribution diameters were scaled by a factor of 1.5. Table 3.1 demonstrates that the important statistics of the “5-29-96 Run 4” case are well

matched by the “Truncated, Stretched, and Scaled” case. Figure 3.15(d) demonstrates agreement between the histograms for the experimentally measured distribution and the conditioned simulated distribution. Finally, Figure 3.14(d) demonstrates the appropriate spacing-to-diameter ratio.

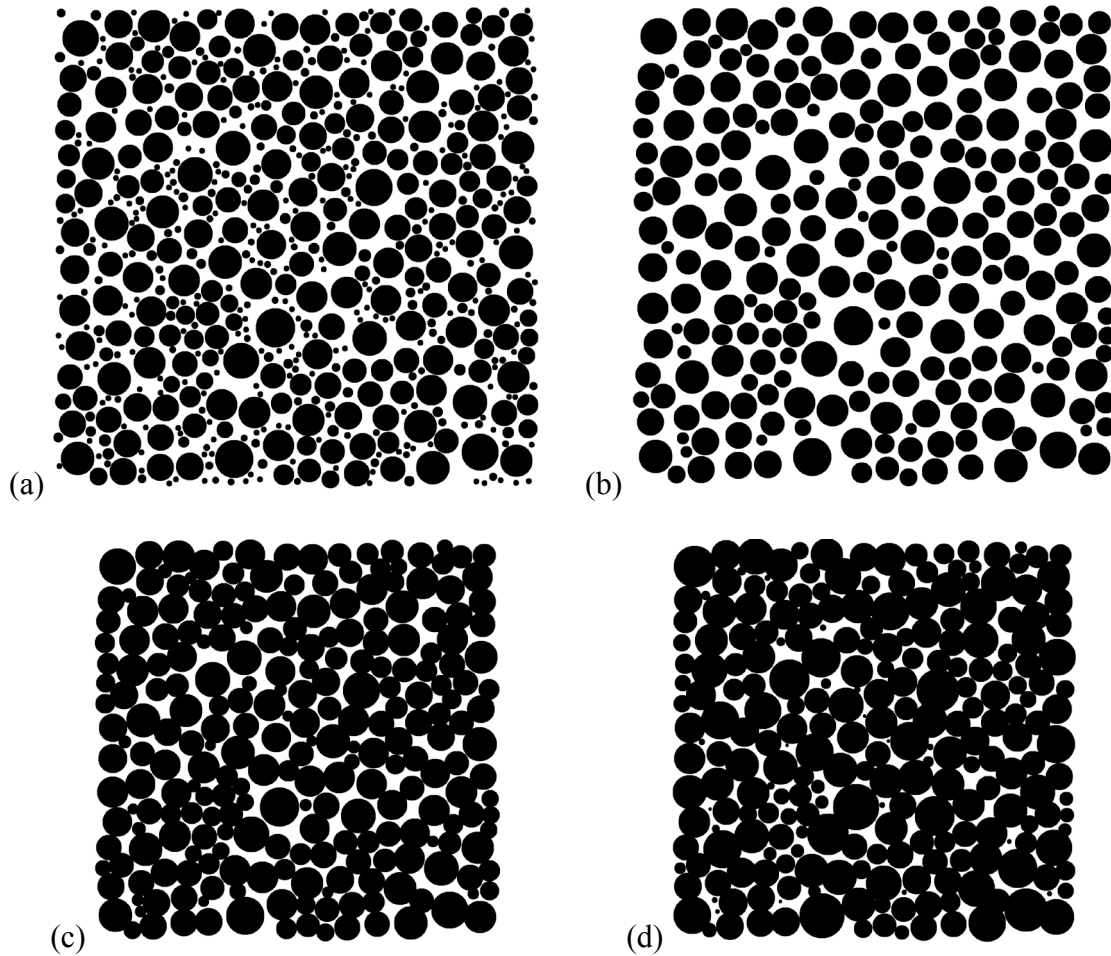


Figure 3.14: Comparison of droplet distributions for the “5-29-96 Run 4” case from (a) unconditioned data, (b) truncated data, (c) truncated and stretched data, and (d) truncated, stretched, and scaled data

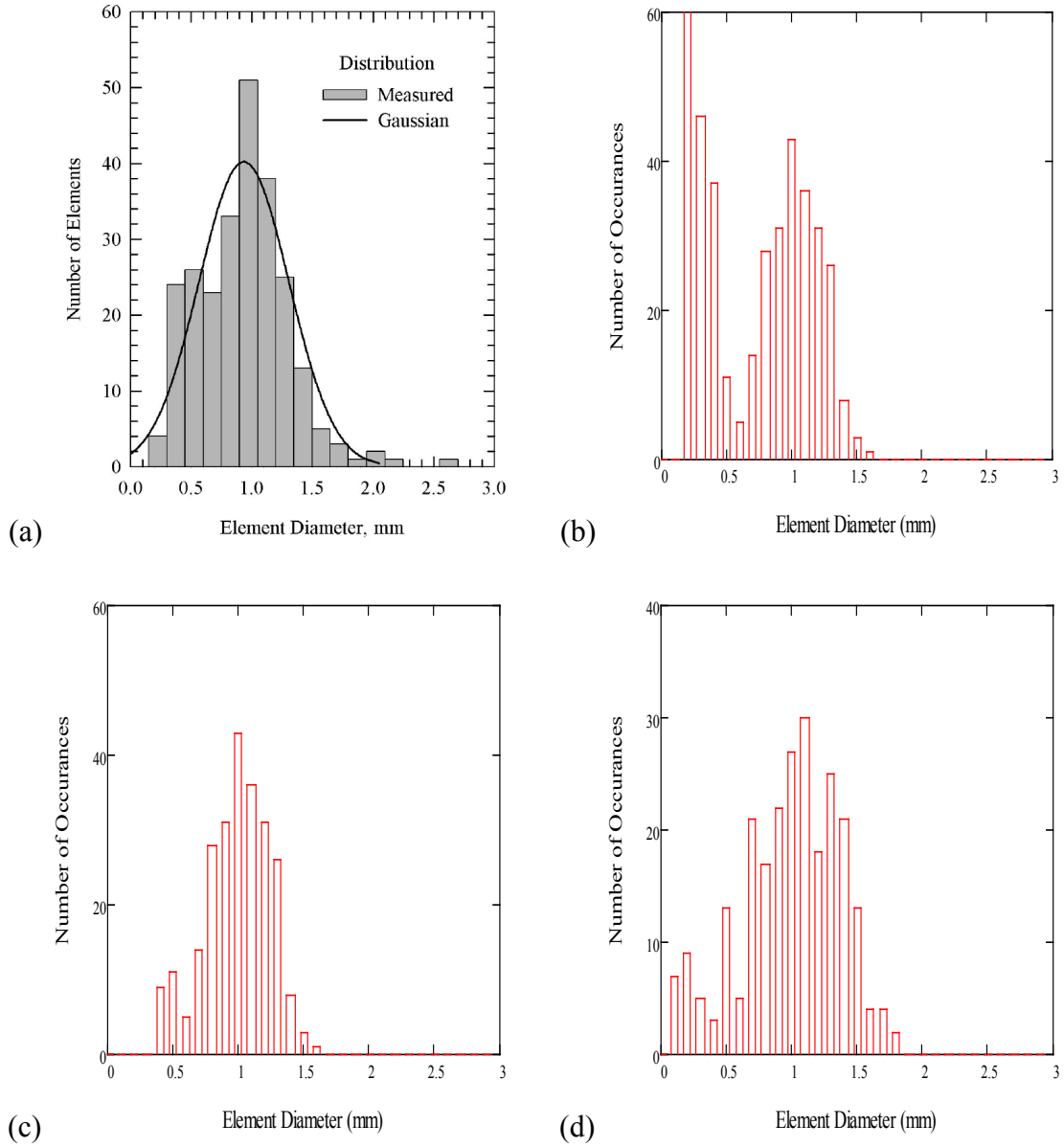


Figure 3.15: Comparison of droplet diameter distributions for the “5-29-96 Run 4” case from (a) Anderson et al. [23], (b) unmodified Lagrangian droplet simulator data, (c) truncated and stretched data, and (d) truncated, stretched, and scaled data

Table 3.2 presents a comparison of the “5-30-96 Run 1” measured statistics to the simulator results. The simulator results were first truncated by removing all elements less than 0.30 mm in diameter. The surface was then stretched using a factor of 0.787.

Because of the excellent agreement with the “Truncated and Stretched” case and the experimental measurements, the diameter distribution was not scaled in this case.

Table 3.2: Comparison of unconditioned and conditioned simulator surface statistics to “5-30-96 Run 1” reported values

Parameter	Reported Data [23,26]	Unconditioned Simulator Data	Truncated	Truncated and Stretched
D_{mean} (mm)	0.573	0.472	0.586	0.586
S_E (mm)	0.148	0.201	0.152	0.152
$(P/D)_{\text{mean}}$	N/A	1.143	1.143	0.870
$P_{\text{mean}}/D_{\text{mean}}$	1.2	1.014	1.014	0.840
H/D	0.515	0.50	0.50	0.50

It is important to note that although the data from the Lagrangian droplet simulator had to be conditioned, it still met the goal of providing stochastic distributions of coalesced elements. The droplet simulator is not made to be a completely accurate ice accretion model; therefore, data conditioning would be expected to match actual ice roughness data.

Manufacture of Testable Surfaces

The purpose of the above efforts was to further the creation of testable surfaces featuring realistic ice roughness distributions. As previously noted, a Reynolds number scaling was applied to the roughness and test plate surface to match the leading edge of a NACA 0012 airfoil. The scaling allowed the size of the ice roughness distribution from the Lagrangian droplet simulator to be increased by a factor of ten, bringing it to a more easily manufactured size; the scaling also allowed for testing at a velocity of 6.7 m/s

instead of the 67 m/s used by Anderson et al. [23]. After scaling, the surface was replicated in a 4x6 pattern so that it would be able cover the entirety of the target surface on the test plate (see Figure 3.4). The entire test plate surface had to be covered to prevent flow spanwise migration. Figure 3.16 shows the surface as it goes through the scaling and replication processes for the “5-29-96 run 4” case. The final surface for the “5-29-96 run 4” case is identified as 052996_run4_x10 going forward; the “5-30-96 run 1” case is identified as 053096_run1_x10.

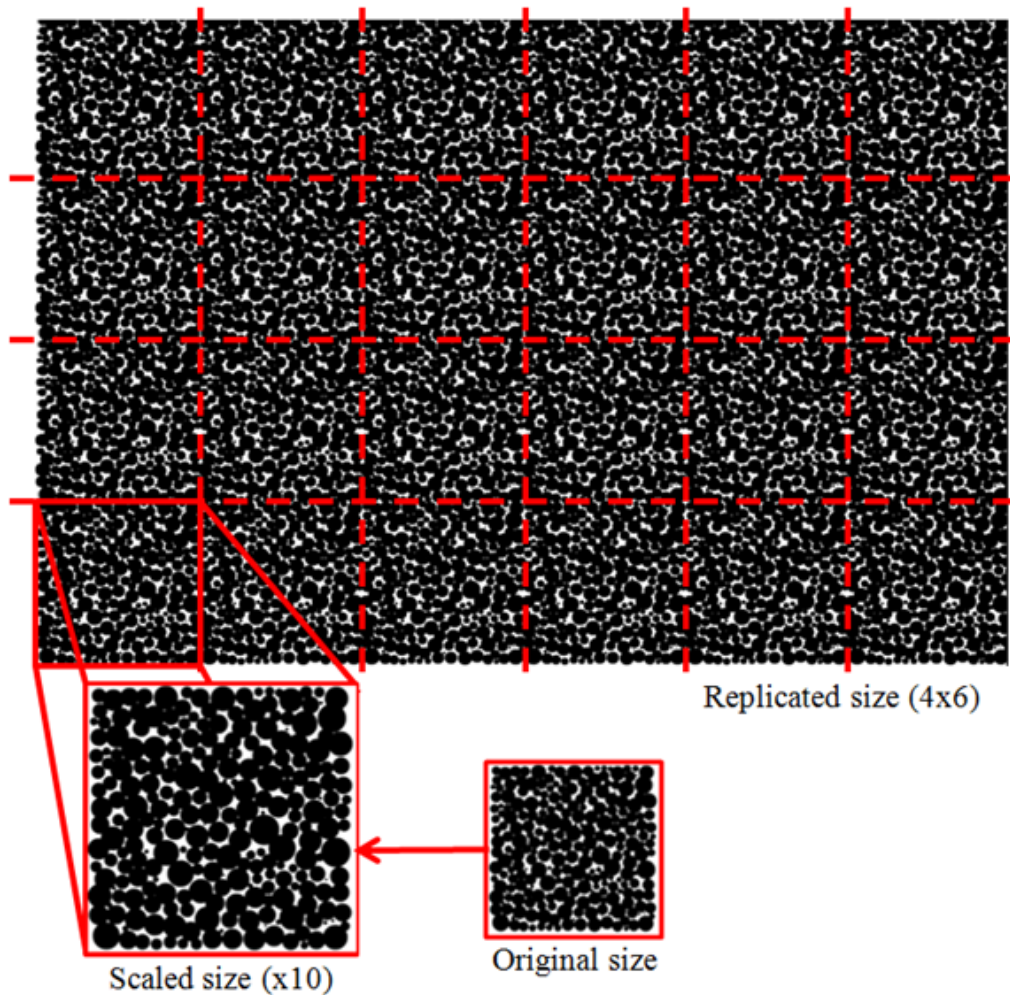


Figure 3.16: Scaling and replication of a roughness surface for “5-29-96 run 4” (not to scale)

The steps used to complete the manufacture of the interchangeable test plate surfaces after the surface scaling and replication are detailed below.

1. The 25 plates required to create the interchangeable surface were created as smooth templates in SolidWorks.
2. The final replicated surface data was output to a text file containing the x-location, y-location, and radius of each element in the distribution.
3. The surface data was parsed into 25 subsets, one for the elements covering each plate.
4. For each plate a SolidWorks macro was used which took in the roughness data subset and automatically generated the elements onto the blank template. A macro was used since it was impractical to have a user model thousands of individual surface elements.
5. The SolidWorks models were converted to stereolithography (STL) files using a linear resolution of 0.001" and an angular resolution of 5°. An STL repair program (Netfabb) was used to repair any errors in the STL files, such as degenerated triangles or split manifolds.
6. The STL models were uploaded to one of two rapid prototyping machines (i.e. 3D printers). An Objet 30 and a Dimension 768 SST were available for the manufacture of the plates. Both machines created testable models using ABS plastic.
7. After printing, 1/16" neoprene gaskets were adhered to the bottom of each plate. The gaskets were added to the heated section plates to reduce the contact resistance between the plate and the heater without using troublesome thermal

paste. The gaskets were installed on the plates outside of the heated sections simply to even out the surface height.

8. The heated section plates (C0-C4) were spray painted with a coat of flat black paint to provide a constant surface emissivity of 0.95.

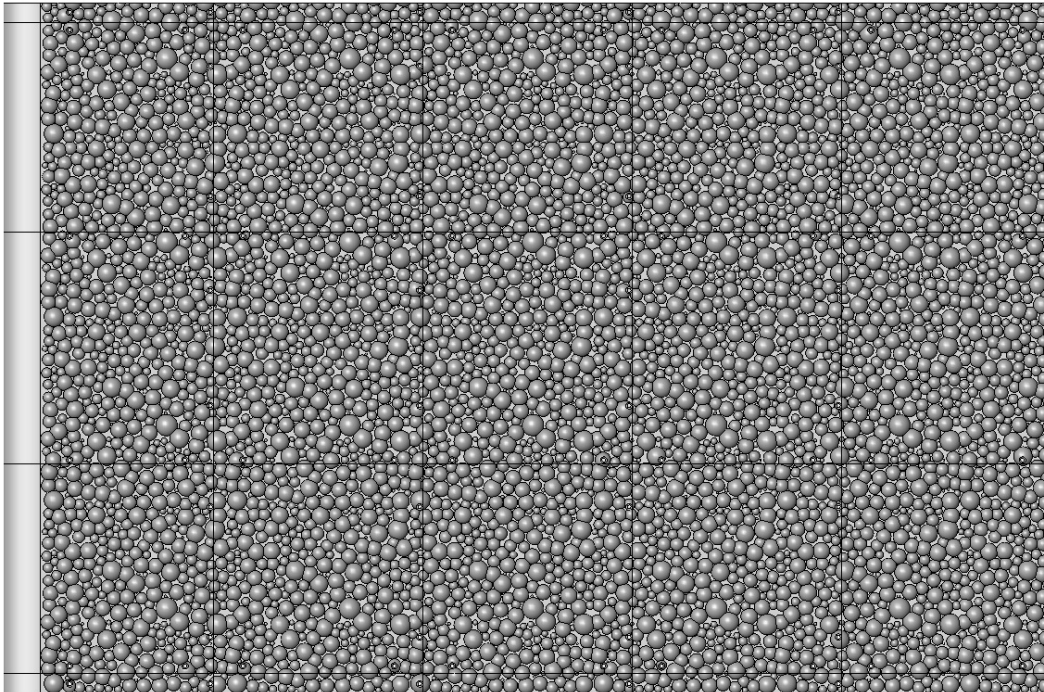
For the smooth validation test plates, steps 2-4 were unnecessary. Figures 3.17 and 3.18 compare the SolidWorks models for the 052996_run4_x10 and 053096_run1_x10 test plate surfaces to the final printed surfaces. Note the smooth area of 116 mm near the leading edge of the 053096_run1_x10 surface. This correlates to the reported smooth-zone width of 23.2 mm scaled up by a factor of 10 and then divided in half (since only one side of the smooth-zone is modeled by the flat plate).

Experimental Procedure and Instrumentation

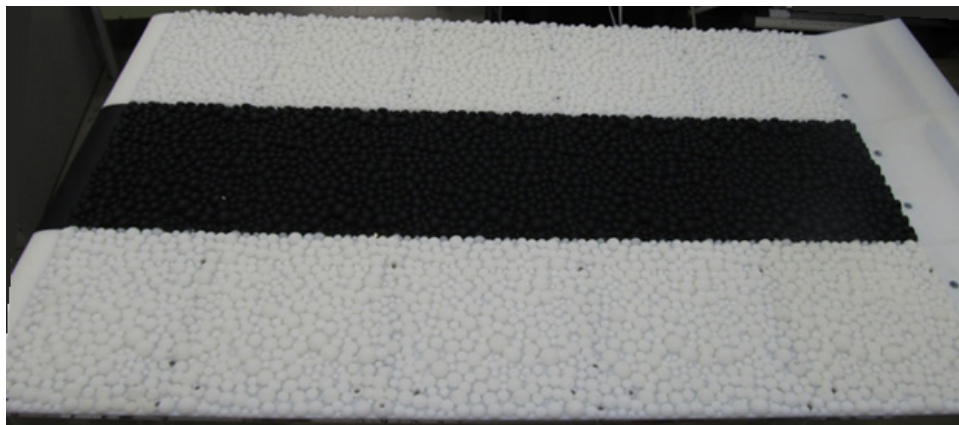
All testing described in the following procedures was performed in the Baylor University Subsonic Wind Tunnel. The wind tunnel is a Model 406B manufactured by Engineering Laboratory Design, Inc. The wind tunnel has a test section with cross-sectional dimensions of 24" by 24", spanning about 48". A 40 HP, variable speed electric motor drives a constant pitch fan. The wind tunnel is able to produce airflows ranging from 0.1 m/s to 50 m/s with a velocity variation over the test section of less than $\pm 1\%$. An inlet contraction ratio of 6.25:1, a precision honeycomb inlet, and three graduated, high-porosity screens provide a clean inlet turbulence intensity of approximately 0.2%.

A series of three experiments was performed for each surface: 1) steady state convective heat transfer coefficient measurement, 2) velocity boundary layer measurement, and 3) thermal boundary layer measurement. Three different surfaces were tested, a smooth validation surface and two rough surfaces (052996_run4_x10 and

053096_run1_x10). The smooth surface was tested in both the laminar and turbulent flow regime by adding a 0.10" square trip strip near the leading edge of the plate, giving two sets of validation data. The procedures and instrumentation used for each test are detailed in the following sections.

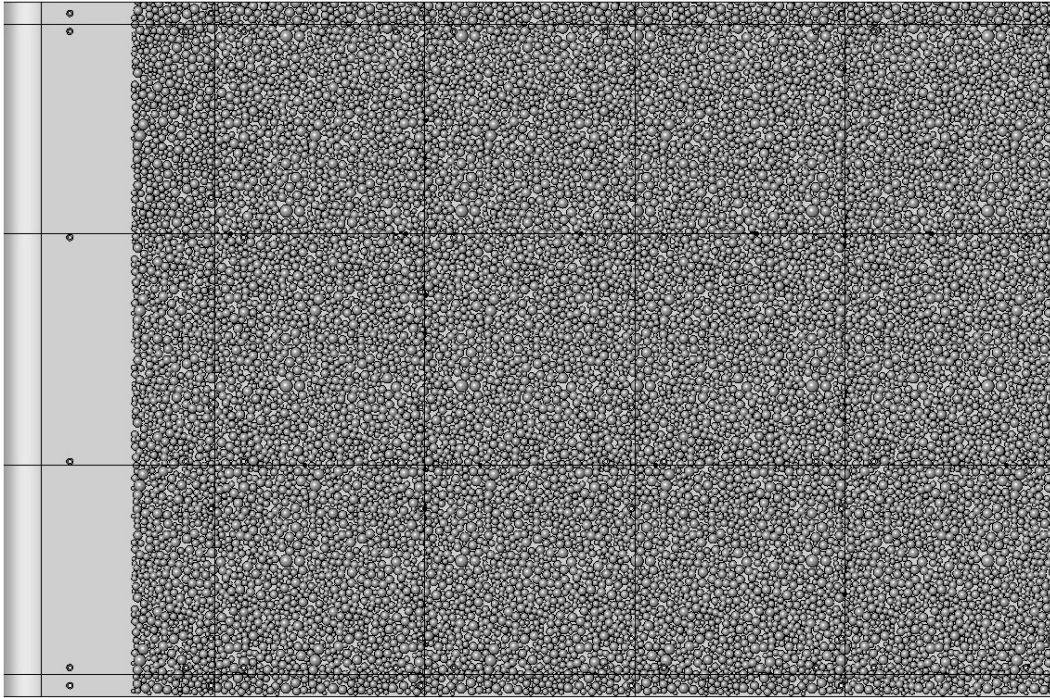


(a) Surface model in SolidWorks



(b) Printed surface installed on test plate

Figure 3.17: 052996_run4_x10 surface comparison



(a) Surface model in SolidWorks



(b) Printed surface installed on test plate

Figure 3.18: 053096_run1_x10 surface comparison

Steady State Convective Heat Transfer Coefficient Test

This test was performed to obtain the data necessary to calculate the convective heat transfer coefficients across each heated section. A FLIR SC4000 ThermoVision IR camera with a 25 mm lens was used to measure the surface temperatures. The SC4000

has an indium-antimonide (InSb) detector capable of generating highly resolved 320 by 256 pixel thermal maps of the test surface. At this resolution the camera has a maximum frame rate of 432 Hz. For the focal distance utilized in this experiment the pixel width was calculated as 0.02 in. Using this pixel width, the total viewing area for each image was 6.4" in the flow direction by 5.12" in the span direction. The data from the camera was read into an HP Compaq 8000 Elite PC running FLIR ExaminIR 1.40 software.

FLIR IRW-3C calcium-fluoride viewing windows were used to provide optical access to the regions of interest for heated sections 0-3. Due to equipment availability, Saran wrap was used to provide optical access to section 4. The windows were installed at a 30° incline to eliminate reflection from the IR camera's internal cooling signature. An aluminum mount was affixed to the traversing carriage of a Velmex BiSlide one-dimensional traversing system to support the IR camera. The camera's position on the traverse was controlled by a Velmex VXM programmable stepping motor controller. Figure 3.19 shows the IR equipment installed on a customized wind tunnel ceiling.

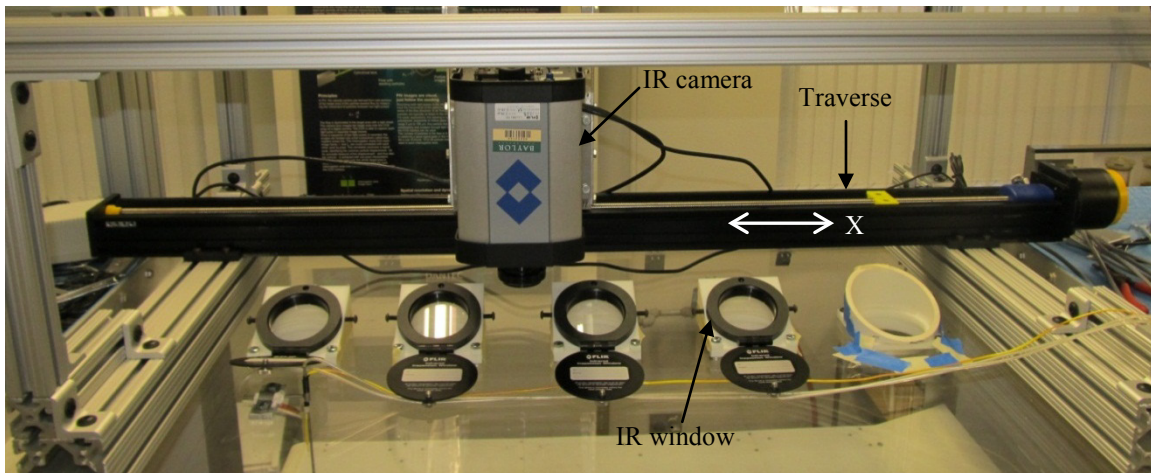


Figure 3.19: IR equipment installed on the wind tunnel ceiling

A 6" Pitot-static probe was used to monitor the freestream velocity. To measure the dynamic pressure difference at the Pitot-static tube, an Omega PCL-2A pressure transducer with a PCL-MA-01WC pressure module was used. An Omega zED-THP-LED wireless transmitter with a zTHP-P sensor was used to measure the temperature, pressure, and relative humidity of the air at the inlet of the wind tunnel.

As previously discussed, the test plate was instrumented with thermocouples to characterize the heat loss through the Plexiglas. These were all Type K thermocouples from Omega. Starting at the leading edge and moving downstream, the subsurface thermocouples were designated TC0-TC7 and the thermocouples under the plate were designated TC8-TC15. An additional thermocouple was used to measure the freestream temperature; its designation was TC16. The seventeen thermocouples (TC0-TC16) were connected to five National Instruments (NI) 9211 thermocouple modules mounted on an NI cDAQ-9172 chassis. Figure 3.20 shows the locations for each of the thermocouple pairs relative to the leading edge of the Plexiglas plate. This figure also details the relative locations of the centers for the IR window ports, indicated by dashed lines.

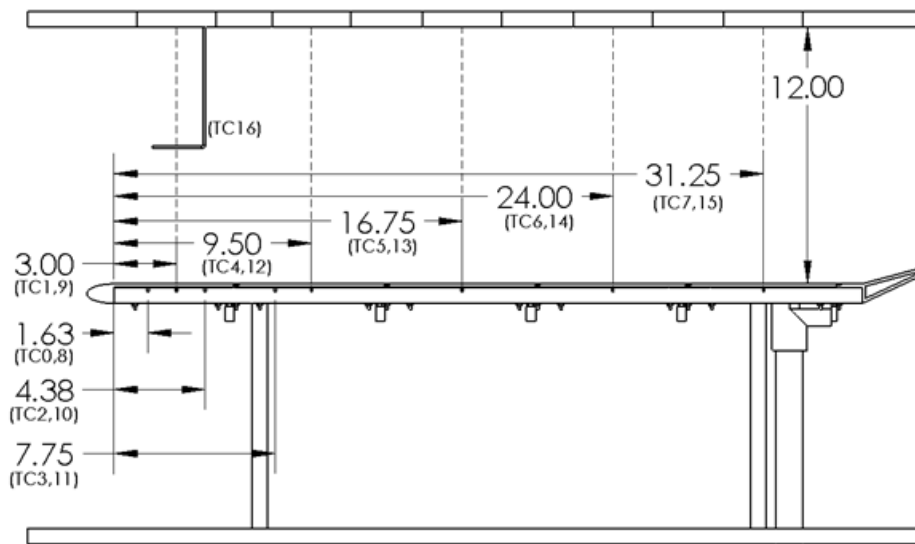


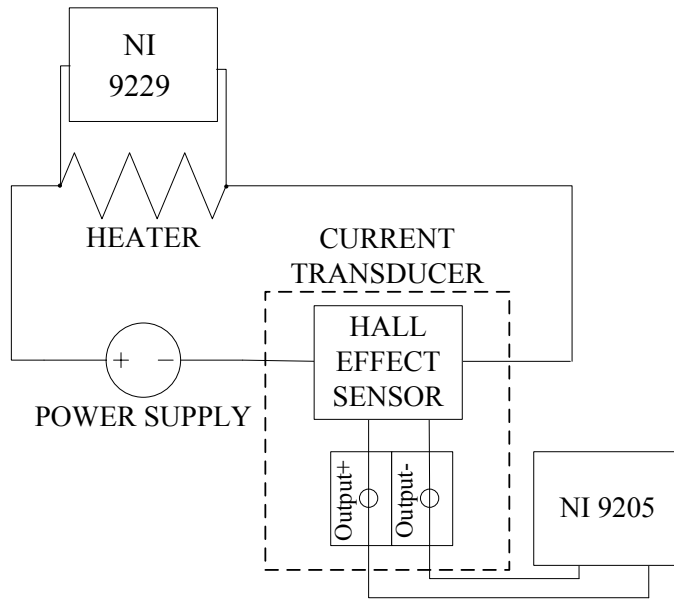
Figure 3.20: Thermocouple and IR window locations, dimensions are in inches

Each of the five heated sections was connected to a separate BK Precision power supply (model 1760A for sections 0, 1, and 4; model 1761 for sections 2 and 3). The power supplies were set to parallel tracking mode to provide the maximum available output current. This gave an operating range of 0-30 V with a 4 A current capability for the model 1760A and 0-35 V with a 6 A current capability for the model 1761. For the first four heated sections (sections 0-3), the voltage was measured across the Mylar film using an NI 9229 high voltage input module wired to the terminal post connections. The current through each heated section was measured using three Powertek CTH/10A/TH/24Vdc Type 1 current transducers (sections 1-3) and one Powertek CTH/20A/TH/24Vdc Type 1 current transducer (section 0). The negative wire from the power supply was passed through the sensor of the current transducer, with the output of the transducer read by an NI 9205 low voltage input module. Both of the data acquisition modules were mounted on an NI cDAQ-9172 chassis (separate from the one used for the thermocouple modules). Due to equipment availability, two Newport TrueRMS HHM290/N Supermeters periodically recorded by the operator were used to monitor the current and voltage in heated section 4. Figure 3.21 shows a wiring diagram for the powering and measurement of (a) sections 0-3 and (b) section 4.

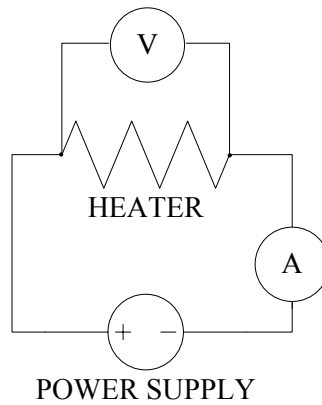
A modified wooden rolling cart was used to hold all of the power and measurement equipment. During testing it was rolled under the wind tunnel test section and wired to the test plate. Figure 3.22(a) shows the data acquisition cart wired to the test plate; Figure 3.22(b) shows the current transducer board prior to installation on the cart.

All of the thermocouple and voltage data was read into an HP Compaq 8000 Elite PC (separate from the one used for the IR data) running LabVIEW 11.0 software. The

LabVIEW program measured 21 samples at a rate of 3 samples per second for temperature measurements and 100 samples at a rate of 100 samples per second for voltage measurements. Table 3.3 presents the range and accuracy for each piece of data acquisition equipment mentioned above.

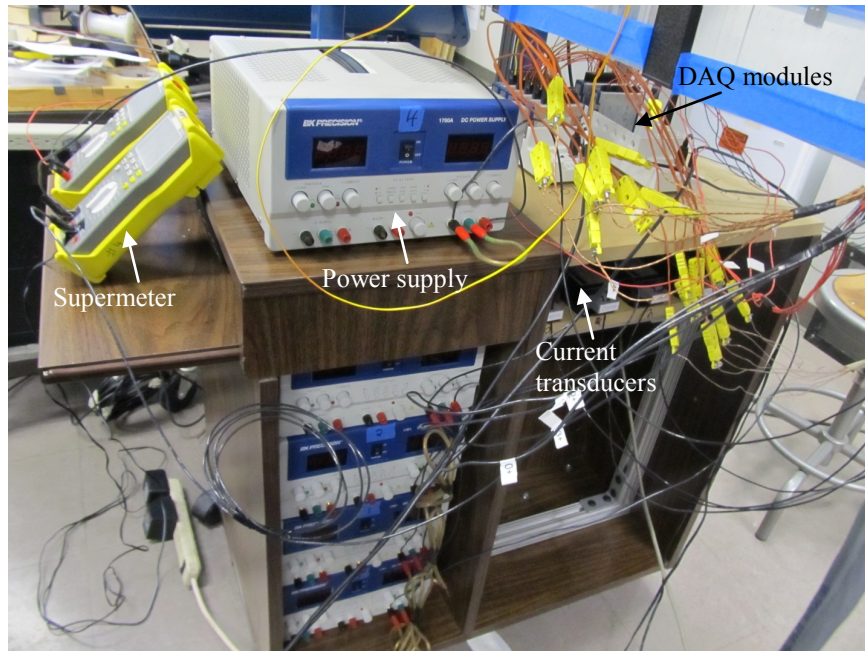


(a) Sections 0-3

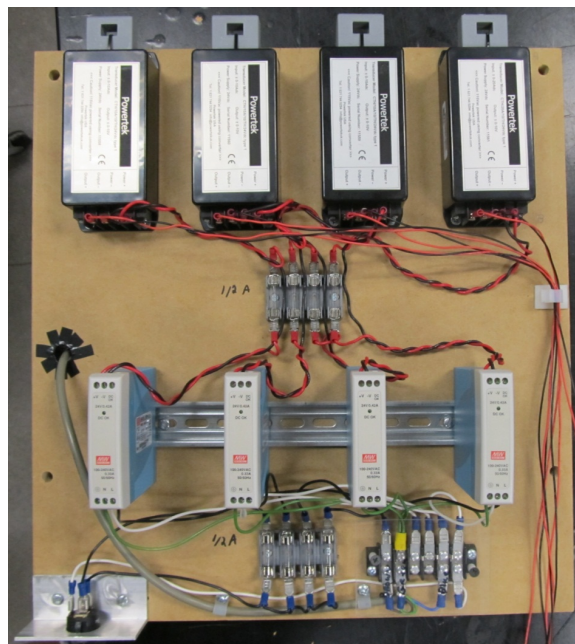


(b) Section 4

Figure 3.21: Wiring diagrams for power supply and measurement



(a) Data acquisition cart wired to test plate



(b) Current transducer board prior to installation in the cart

Figure 3.22: Data acquisition cart setup

Table 3.3: Stated ranges and accuracies of instrumentation

Instrument	Range	Accuracy
FLIR SC4000	-20 to 250 °C	2 K
Omega PCL-2A with PCL-MA-01WC module	0 to 1 inH ₂ O	0.0006 inH ₂ O
Omega zED-THP-LED with zTHP-P sensor	Relative humidity: 0 to 100% Temperature: -40 to 124 °C Pressure: 1 to 110 kPa	2% 0.5 °C 0.2 kPa
Powertek CTH/10A/TH/24Vdc Type 1 current transducer	0 to 10 A	0.05 A
Powertek CTH/20A/TH/24Vdc Type 1 current transducer	0 to 20 A	0.10 A
Newport TrueRMS HHM290/N Supermeter	Voltage: 0.43 to 1000 V Amperage: 430×10^{-6} to 10 A	0.25% of reading 2.5% of reading

Prior to performing the steady state heat transfer test, the instrumented test plate (with the surface of interest affixed) and IR equipment were installed in the wind tunnel test section. A black felt sheet was placed over the wind tunnel test section during testing to shield the IR camera from reflections caused by light contamination. The test section was allowed to sit undisturbed overnight prior to testing to ensure that all of the temperature readings were nominally equal. The procedure used for the steady state heat transfer test was as follows:

1. The pressure transducer, current transducers, motor controllers, IR camera, and data acquisition modules were powered on.
2. The necessary LabVIEW programs were started. For this experiment, one program was used to acquire all of the non-IR camera data (temperature, voltage,

- and pressure) while another program was used to control the IR camera position on the traverse.
3. The ExaminIR software was initiated and the camera was focused. A PC-side one point correction was applied at section 0. Calibration images were taken for each of the five sections using the IR camera. Seventy images were taken at a rate of 7 Hz for each section; these images were then averaged to create the final image.
 4. The PCL-2A was zeroed and then the wind tunnel started, set to a nominal air velocity of 6.7 m/s.
 5. All five power supplies were turned on. The power varied for each surface tested, but in all cases it met two requirements: (1) the flux generated in each heated section was nominally equivalent and (2) the center of the plate had a temperature increase of about 10 K at steady state. This was an iterative process, with the power supplies adjusted until the desired temperature difference was obtained.
 6. Using LabVIEW, the heat loss through the Plexiglas test plate was monitored until it reached steady state. In general, this took between one and two hours.
 7. Using the IR camera seventy steady state images were taken at a rate of 7 Hz for each section. The image set was averaged to create the final image.
 8. Beginning with the power supplies, all equipment was powered down.

Thermal Boundary Layer Measurement

These tests were performed to characterize the thermal boundary layer at the center of each heated section. The instrumentation and procedure used for this test was almost identical to the steady state heat transfer test. The main difference in instrumentation was the lack of the IR equipment, which was replaced by a Type T

thermocouple probe. A different ceiling was also installed, with a Velmex BiSlide two-dimensional traversing system to support the thermal boundary layer probe and an access slot down the centerline of the plate in the flow direction. The thermocouple was read by an NI 9211 thermocouple module mounted on an NI cDAQ-9172 chassis. Figure 3.23 shows the boundary layer traversing ceiling on the wind tunnel.

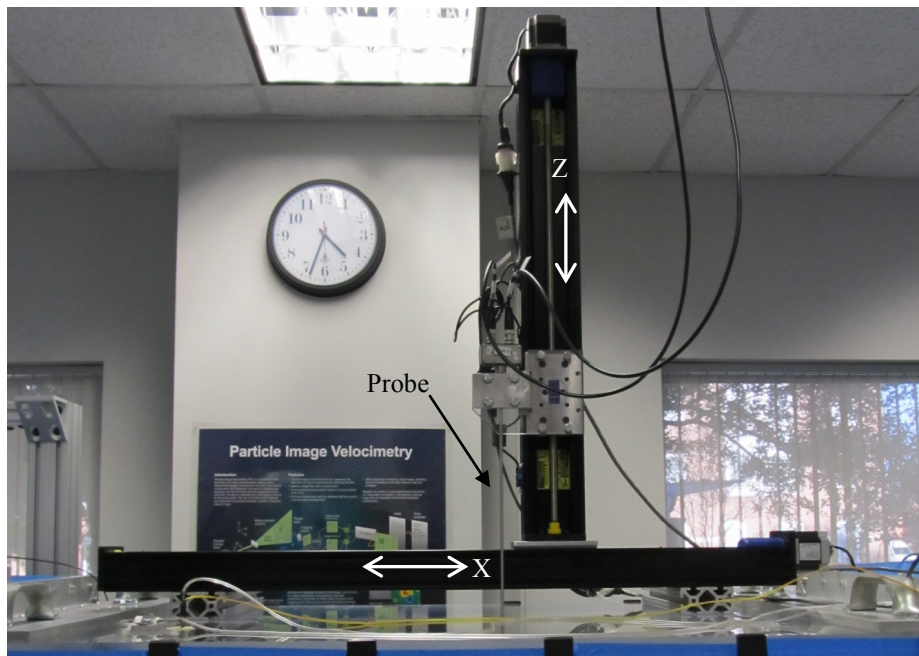


Figure 3.23: Boundary layer traversing ceiling installed on wind tunnel

The experimental procedure was the same as the steady state heat transfer test for steps 1-2 and 4-6. For this test, once steady state was reached the thermocouple probe was positioned as close to the surface of the plate as possible (within $1/64$ "). A LabVIEW program was then used to traverse the probe in the vertical direction through a 6", 101 point, geometrically expanding measurement grid with a geometric expansion factor of 1.07. At each of the 101 measurement points the temperature was acquired. For

each measurement, 140 samples were taken at a rate of 14 samples per second. This process was repeated at the center of each of the five heated sections.

Velocity Boundary Layer Measurement

These tests were performed to characterize the velocity boundary layer at the center of each heated section. The only instrumentation required from the previous tests was the Pitot-static tube, pressure transducer, and inlet air monitor. The sections were not heated for this test so temperature and power data did not have to be acquired. A model 1201 hot film probe powered by a TSI Inc. IFA300 constant temperature anemometry system was used to acquire velocity boundary layer data. A Dell Optiplex GX1 computer running ThermalPro software was used to initialize the IFA300 and to assign a channel to the probe.

The same ceiling was used as for the thermal boundary layer tests, replacing the thermocouple probe with the hot film probe. After setting the wind tunnel air velocity to 6.7 m/s, the hot film probe was positioned as close to the surface of the plate as possible (within 1/64"). A LabVIEW program was then used to traverse the probe in the vertical direction through a 6", 101 point, geometrically expanding measurement grid with a geometric expansion factor of 1.07. An NI PCI-6052E installed on the PC was used to acquire the velocity information at each of the 101 measurement points. For each measurement, 100,000 samples were taken at a rate of 50,000 samples per second. This process was repeated at the center of each of the five heated sections.

CHAPTER FOUR

Data Reduction and Uncertainty Analysis

This chapter details the methods used in the reduction of the data which was acquired during the convective heat transfer and boundary layer tests. The validity of the data reduction schemes is explored using the results of the smooth test surface. The quantification of uncertainty is also discussed.

Convective Heat Transfer Coefficient Measurements

The calculation of convective heat transfer coefficients from the measured data involved several steps, which are detailed below.

Air Properties

The acquisition of data was spread across several weeks. Therefore, a sophisticated analysis of the laboratory air properties was performed to eliminate any errors stemming from variations in atmospheric conditions. A technique identical to that of Mart [33] was used for this task. A Mathcad program was used which calculated the thermodynamic properties of moist air given the air temperature, pressure, and relative humidity. As detailed in Chapter Three, this data was acquired at the inlet of the wind tunnel using an Omega wireless transmitter. The Mathcad program is based upon a standard published by the International Association for the Properties of Water and Steam [34]; it also utilizes Sutherland's Law [35] and Wilke's equation for gas mixtures [36]. The calculated properties of interest for this investigation were the air density, dynamic

viscosity, thermal conductivity, and Prandtl number. Table 4.1 shows the results of this calculation for each of the surfaces.

Table 4.1: Air properties during convective heat transfer tests

Surface	Measured			Calculated			Pr
	T (K)	P (kPa)	Φ (%)	ρ (kg/m ³)	μ (kg/m·s)	k (W/m·K)	
Smooth Laminar	294.00	102.2	62.6	1.204	1.891E-05	0.02569	0.744
Smooth Turbulent	292.46	100.6	41.7	1.194	1.855E-05	0.02560	0.730
052996_run4_x10	292.02	99.0	2.46	1.181	1.181E-05	0.02562	0.709
053096_run1_x10	293.22	101.6	39.9	1.206	1.859E-05	0.02566	0.730

Temperature Calibration

An *in situ* calibration was performed to reference the thermocouple and IR camera temperature measurements to the measured freestream temperature. Eq. (4.1) shows the equation used to correct the subsurface and under the plate thermocouple measurements (TC0-TC15), where T_{TC} is the corrected thermocouple temperature, $T_{TC,S}$ is the uncorrected thermocouple measurement at steady state, $T_{TC,C}$ is the thermocouple measurement at calibration, and $T_{\infty,C}$ is the freestream temperature during calibration.

$$T_{TC} = T_{TC,S} - (T_{TC,C} - T_{\infty,C}) \quad (4.1)$$

The IR camera temperatures required a more rigorous calibration procedure to correct for the transmissivity (τ) of the viewing windows between the IR camera and the test surface. The IR camera has a detector which measures the heat flux generated at each pixel (W_S). This flux is then used to back out the measured steady state temperature at each pixel ($T_{IR,S}$) using Eq. (4.2), where $T_{IR,REF}$ is the IR detector reference temperature (77 K), ε is the surface emissivity, and σ is the Stefan-Boltzmann constant.

$$W_S = \sigma \varepsilon (T_{IR,S}^4 - T_{IR,REF}^4) \quad (4.2)$$

A flux correction (ΔW) can then be applied to correct the IR camera temperature using Eq. (4.3), where $T_{IR,C}$ is the measured IR temperature at calibration.

$$\Delta W = \tau \sigma \varepsilon (T_{\infty,C}^4 - T_{IR,REF}^4) - \sigma \varepsilon (T_{IR,C}^4 - T_{IR,REF}^4) \quad (4.3)$$

Applying this flux correction to the measured flux yields Eq. (4.4), where W_{COR} is the corrected IR flux.

$$W_{COR} = W_S + \Delta W = \tau \sigma \varepsilon (T_{IR}^4 - T_{IR,REF}^4) \quad (4.4)$$

Solving Eq. (4.4) for the corrected IR temperature at steady state (T_{IR}) yields Eq. (4.5).

$$T_{IR} = \left[\frac{T_{IR,S}^4 - T_{IR,C}^4}{\tau} + T_{\infty,C}^4 \right]^{1/4} \quad (4.5)$$

Applying Eq. (4.5) to each measured pixel temperature corrects for the effects of transmissivity and calibrates the IR measurements to the freestream temperature.

Heat Transfer Equation

Figure 4.1 shows the heat transfer modes during the steady state heat transfer experiments. Heat is added to the system via the Mylar film heater (Q_{GEN}). Some of the heat is lost to conduction through the Plexiglas (Q_{HL}). The rest of the heat is conducted through the Mylar, Neoprene, and ABS layers (Q_{COND}). At the surface of the ABS the conducted heat is lost through either convection (Q_{CONV}) or radiation (Q_{RAD}). Combining these terms yields Eq. (4.6); solving for the convective term yields Eq. (4.7).

$$Q_{GEN} = Q_{COND} + Q_{HL} = (Q_{CONV} + Q_{RAD}) + Q_{HL} \quad (4.6)$$

$$Q_{CONV} = Q_{GEN} - Q_{HL} - Q_{RAD} \quad (4.7)$$

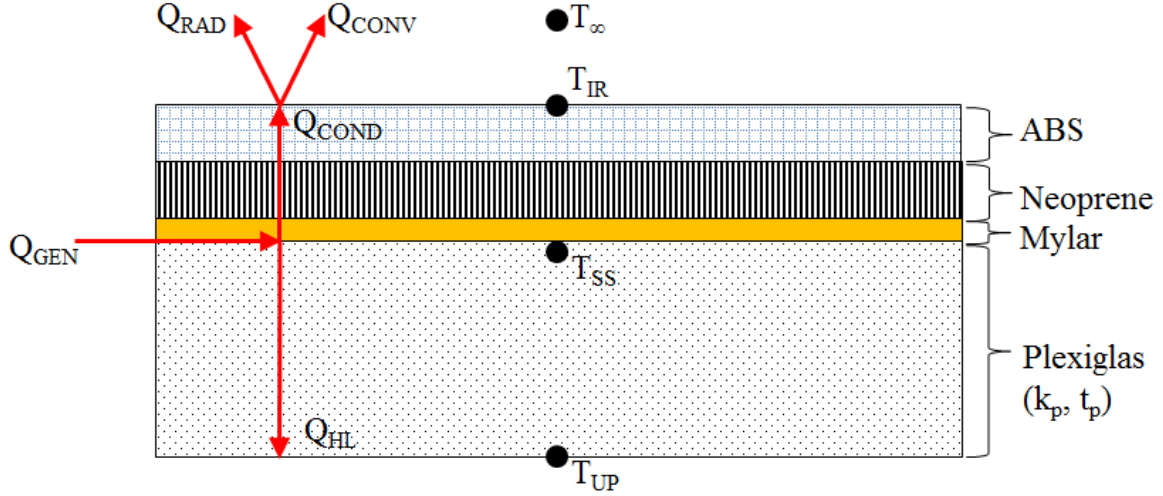


Figure 4.1: Heat transfer diagram (not to scale)

The convection term can be expressed per pixel as shown in Eq. (4.8), where h is the local pixel convective heat transfer coefficient, A_{pix} is the pixel area, T_{IR} is the corrected pixel surface temperature, and T_{∞} is the calibrated freestream temperature.

$$Q_{CONV} = hA_{pix}(T_{IR} - T_{\infty}) \quad (4.8)$$

The generation term can be expressed per pixel as shown in Eq. (4.9), where E is the voltage applied to the heated section, I is the current through the heated section, and A_t is the total area of the heated section.

$$Q_{GEN} = EI \frac{A_{pix}}{A_t} \quad (4.9)$$

The conduction heat loss through the Plexiglas can be expressed per pixel as shown in Eq. (4.10), where k_p is the thermal conductivity of Plexiglas, t_p is the Plexiglas thickness, T_{SS} is the calibrated subsurface Plexiglas temperature measurement, and T_{UP} is the calibrated Plexiglas temperature measured under the plate.

$$Q_{HL} = \frac{k_p}{t_p} A_{pix}(T_{SS} - T_{UP}) \quad (4.10)$$

The radiation term can be expressed per pixel as shown in Eq. (4.11).

$$Q_{RAD} = \varepsilon\sigma A_{pix}(T_{IR}^4 - T_{\infty}^4) \quad (4.11)$$

Substituting Eqs. (4.8)-(4.11) into Eq. (4.7) and solving for local convective heat transfer coefficient at each pixel yields Eq. (4.12).

$$h = \left[\frac{EI}{A_t} - \frac{k_p}{t_p}(T_{SS} - T_{UP}) - \varepsilon\sigma(T_{IR}^4 - T_{\infty}^4) \right] (T_{IR} - T_{\infty})^{-1} \quad (4.12)$$

This is the data reduction equation used to calculate the local convective heat transfer coefficients from the measured data. Eq. (4.13) presents a similar equation for the area averaged convective heat transfer coefficients, where \bar{h} is the area averaged convective heat transfer coefficient and $\overline{T_{IR}}$ is the area averaged IR temperature measurement.

$$\bar{h} = \left[\frac{EI}{A_t} - \frac{k_p}{t_p}(T_{SS} - T_{UP}) - \varepsilon\sigma(\overline{T_{IR}}^4 - T_{\infty}^4) \right] (\overline{T_{IR}} - T_{\infty})^{-1} \quad (4.13)$$

There are several assumptions built into Eqs. (4.12) and (4.13):

- The effects of lateral conduction in the spanwise direction are negligible.
- The heat flux generated by the Mylar film is constant across the heated section.
- The heat loss through the Plexiglas is constant across the heated section, as measured by the thermocouples in the middle of the heated section.

Smooth Surface Validation

The smooth surface test data allowed for validation of the data reduction methodology by comparison to flat plate correlations. Since the smooth surface was tested in both laminar and turbulent flow, two validation data sets were available. A check of the Reynolds number at the end of the plate for the given conditions gave a value of about 4×10^5 , which is below the transitional value of 5×10^5 . This confirms that

the flow over the plate should be laminar unless a transition to turbulent flow is forced.

Appendix A shows an example of the MATLAB code used to perform the data reduction.

Figures 4.2 and 4.3 show the steady state temperature and convective heat transfer coefficient surface maps for the validation surfaces. These figures present the data for each of the five heated sections side-by-side, with the black dashed lines indicating the extent of the Mylar film heaters. Figure 4.2 indicates that the last two heated sections of the laminar flow case had appreciable lateral temperature gradients, which violates one of the basic assumptions for Eq. (4.12). The lateral gradients were caused by the relatively low convective heat transfer coefficients in these sections, allowing lateral heat loss effects to occur. Figure 4.3 shows that the lateral heat loss in the last heated sections is not seen in the turbulent case since the convective heat transfer is higher than in the laminar case, allowing for less heat transfer in the lateral direction. Since any rough surface would also have more dominate convective heat transfer in these sections, the lateral heat loss assumption for Eq. (4.12) is still valid for all other test cases. Figure 4.3 also indicates an area of reduced convective heat transfer near the leading edge of the plate for the turbulent flow case. This was caused by a boundary layer separation in the first heated section due to the use of a trip strip to force flow transition over the plate.

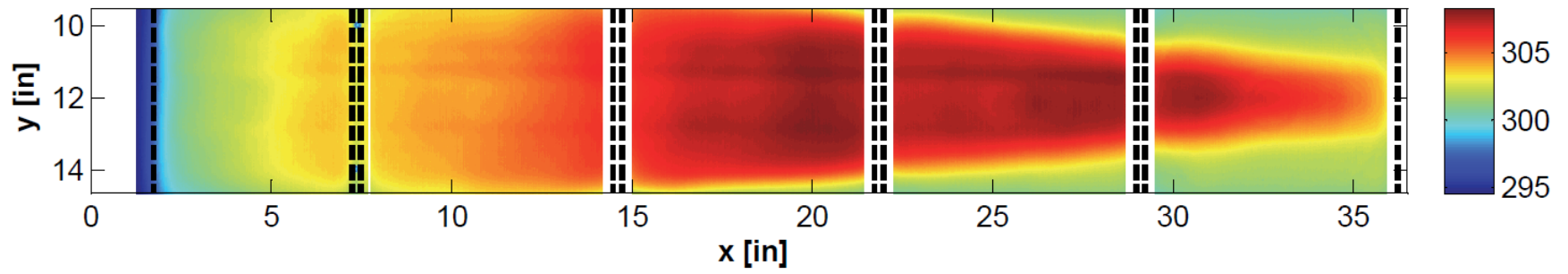
A spanwise average of the convective heat transfer coefficient values was taken along the centerline ± 0.5 ". Using the correlations for laminar and turbulent flow over a smooth flat plate with constant heat flux boundary conditions (see Eqs. (2.10) and (2.11), solved for h), a comparison to the experimental data was made. A correction factor was applied to account for the unheated starting length of 1.7285". Figure 4.4 shows a

comparison of the measured and theoretical centerline convective heat transfer coefficients for both validation cases.

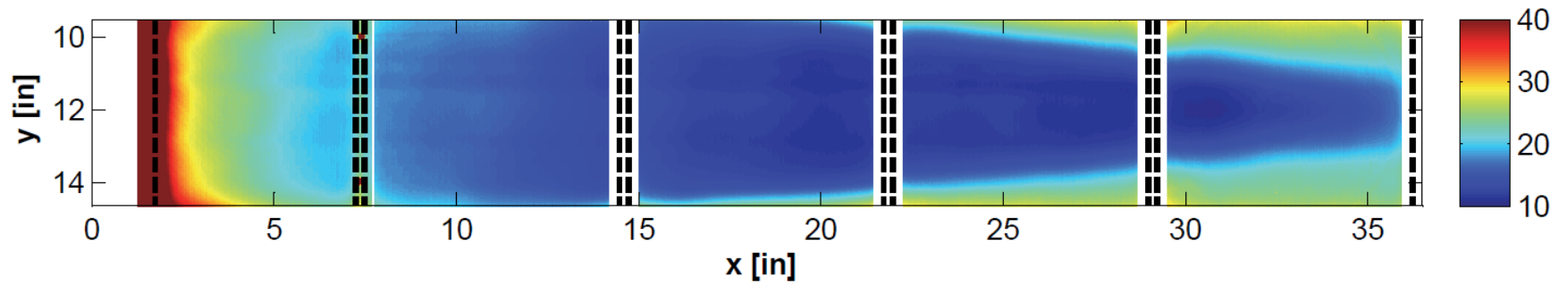
Since the IR windows did not have a published transmissivity, this value was determined iteratively by applying the data reduction scheme with varying transmissivity values until the smooth turbulent centerline average was well matched to the correlated values in heated section 2. The transmissivity value was determined to be 0.82 using this methodology. Applying this value to the laminar data yielded reasonable results, providing confidence in the value.

For both flow regimes, the measured data is generally well matched to the theoretical values in both magnitude and trend, with three main exceptions:

- The laminar case is elevated in the last heated section. This is due in part to the lateral heat loss indicated in Figure 4.2. The flow could also be experiencing transition since the Reynolds number is close to the critical value. A flow interaction with the flap on the trailing edge of the plate could also effect heat transfer in the last heated section (as noted in the viscous boundary layer measurements, presented below).
- The turbulent case exhibits an odd trend in the first heated section due to separation and reattachment of the boundary layer caused by the trip strip, indicated by a region of reduced convective heat transfer near the leading edge.
- Both cases are affected at the start of the first heated section due to the large unheated mass of the bullnose causing longitudinal heat loss along the surface.

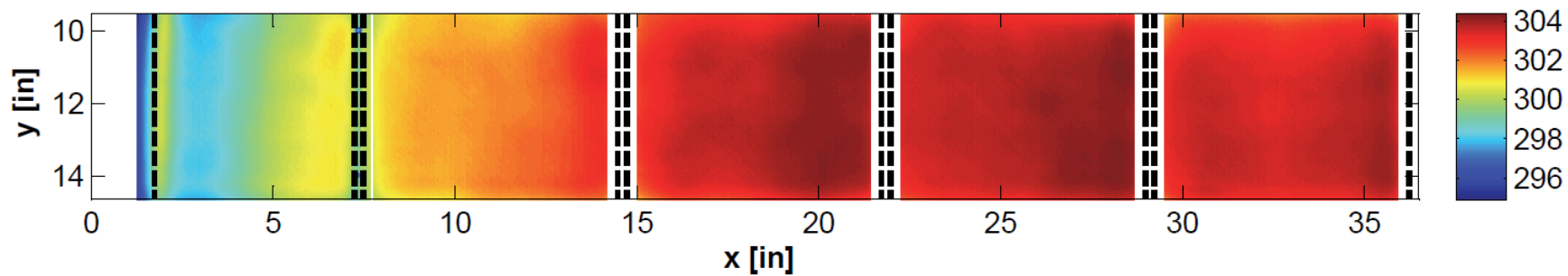


(a) Steady state temperature [K]

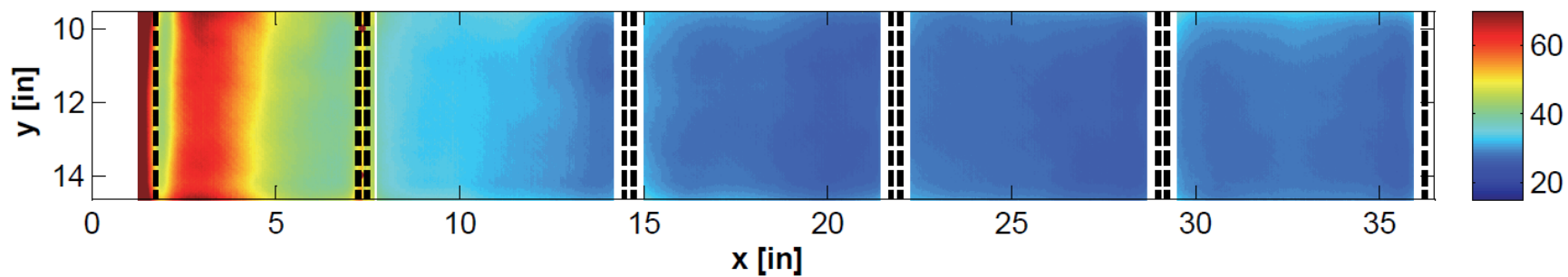


(b) Convective heat transfer [$\text{W}/\text{m}^2 \cdot \text{K}$]

Figure 4.2: Surface maps for the smooth laminar surface

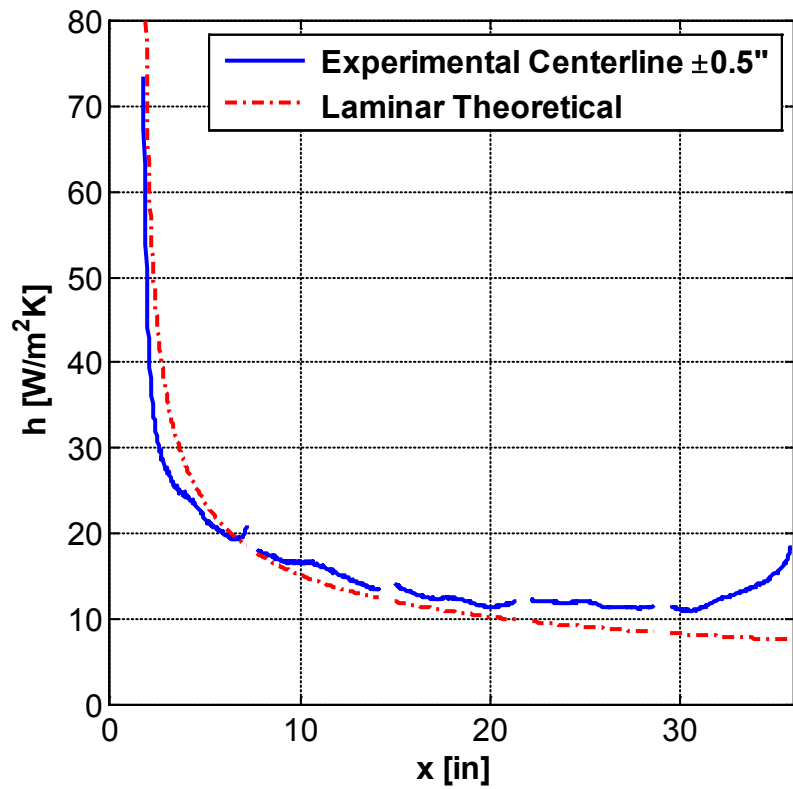


(a) Steady state temperature [K]

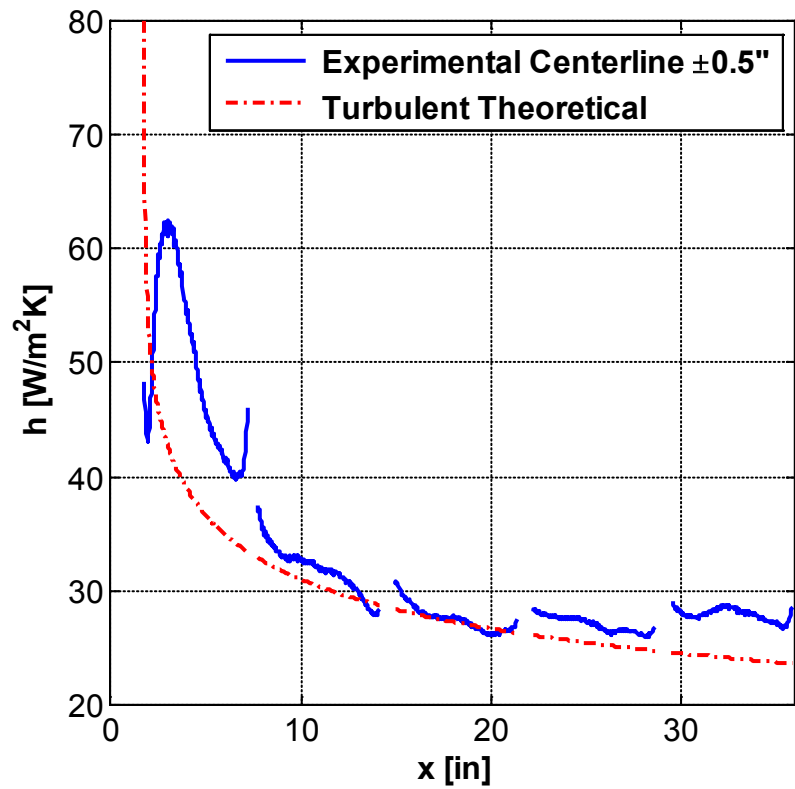


(b) Convective heat transfer [$\text{W}/\text{m}^2 \cdot \text{K}$]

Figure 4.3: Surface maps for the smooth turbulent surface



(a) Smooth laminar



(b) Smooth turbulent

Figure 4.4: Comparison of centerline experimental and theoretical heat transfer

Evaluation of Uncertainty

The uncertainties of the area averaged convective heat transfer coefficients were determined using the large sample size approach of Coleman and Steele [37], which is an extension of the work of Kline and McClintock [38]. Table 4.2 shows a summary of the total uncertainty associated with each variable.

Table 4.2: Total uncertainties and components

Variable	Total Uncertainty	Uncertainty Components
E	$\sqrt{U_{E_fixed}^2 + \left(\frac{tS_E}{\sqrt{N}}\right)^2}$	$U_{E_fixed} = 0.03\% E$ (sections 0-3) $U_{E_fixed} = 0.25\% E$ (section 4)
I	$\sqrt{U_{I_fixed}^2 + \left(\frac{tS_I}{\sqrt{N}}\right)^2}$	$U_{I_fixed} = 0.1 A$ (section 0) $U_{I_fixed} = 0.05 A$ (sections 1-3) $U_{I_fixed} = 2.5\% I$ (section 4)
A_t	$\sqrt{(U_{d_fixed}W_{ha})^2 + (U_{d_fixed}L_{ha})^2}$	$U_{d_fixed} = 1/32''$
t_p	U_{d_fixed}	$U_{d_fixed} = 1/32''$
T_{IR}	$\sqrt{\left(\frac{tS_{T_{IR}}}{\sqrt{N}}\right)^2 + \left(\frac{tS_{T_{\infty}}}{\sqrt{N}}\right)_c^2 + B_T^2}$	$B_T = 1.4 K$
T_{SS}	$\sqrt{\left(\frac{tS_{T_{SS}}}{\sqrt{N}}\right)_s^2 + \left(\frac{tS_{T_{SS}}}{\sqrt{N}}\right)_c^2 + \left(\frac{tS_{T_{\infty}}}{\sqrt{N}}\right)_c^2 + B_T^2}$	$B_T = 1.4 K$
T_{UP}	$\sqrt{\left(\frac{tS_{T_{UP}}}{\sqrt{N}}\right)_s^2 + \left(\frac{tS_{T_{UP}}}{\sqrt{N}}\right)_c^2 + \left(\frac{tS_{T_{\infty}}}{\sqrt{N}}\right)_c^2 + B_T^2}$	$B_T = 1.4 K$
T_{∞}	$\sqrt{\left(\frac{tS_{T_{\infty}}}{\sqrt{N}}\right)_s^2 + \left(\frac{tS_{T_{\infty}}}{\sqrt{N}}\right)_c^2 + B_T^2}$	$B_T = 1.4 K$

In Table 4.2, the random uncertainties are represented as the standard deviation (S) times the Student's t-value (t) divided by the square root of the sample size (N). There is no random uncertainty associated with the voltage/current measurements in section 4, heated area measurement, or Plexiglas thickness since these values are taken as single sample measurements. Also of note is the use of a correlated uncertainty (B_T) in the calculation of the temperature uncertainties; this was necessary since all of the temperature measurements are correlated to the freestream temperature during the calibration procedure. Appendix B shows a detailed example of the Mathcad code used to calculate the experimental uncertainty.

Boundary Layer Thickness Measurements

Viscous Boundary Layers

The viscous boundary layer data was analyzed by first determining the offset of the probe from the surface. For the smooth surfaces this was set at 1/64". For the rough surfaces the offset was estimated by using the height of the roughness element over which the probe was placed. The measured velocities were then nondimensionalized by dividing the measured velocity by the freestream velocity at each station (u/U_∞). The freestream velocity at each station was determined by averaging the measured velocity along the top 4" of the boundary layer trace. The boundary layer height was then determined by finding the height at which the nondimensional velocity passed 0.99. Figure 4.5 shows a comparison of the measured viscous boundary layer for the validation cases to the smooth plate correlations presented in Eqs. (2.2) and (2.3). Figure 4.6 shows the nondimensional velocity profiles for the smooth validation cases.

In general, the viscous boundary layers developed as expected. The theoretical laminar profile is well matched by the measured values, except at the last station. This is due to flow interaction with the flap at the trailing edge of the plate. The measured turbulent boundary layer is about twice as large as expected, with a similar flap interaction noted at the last station. The increased boundary layer height is due to the trip strip adding a height offset, which is consistent across the first four stations.

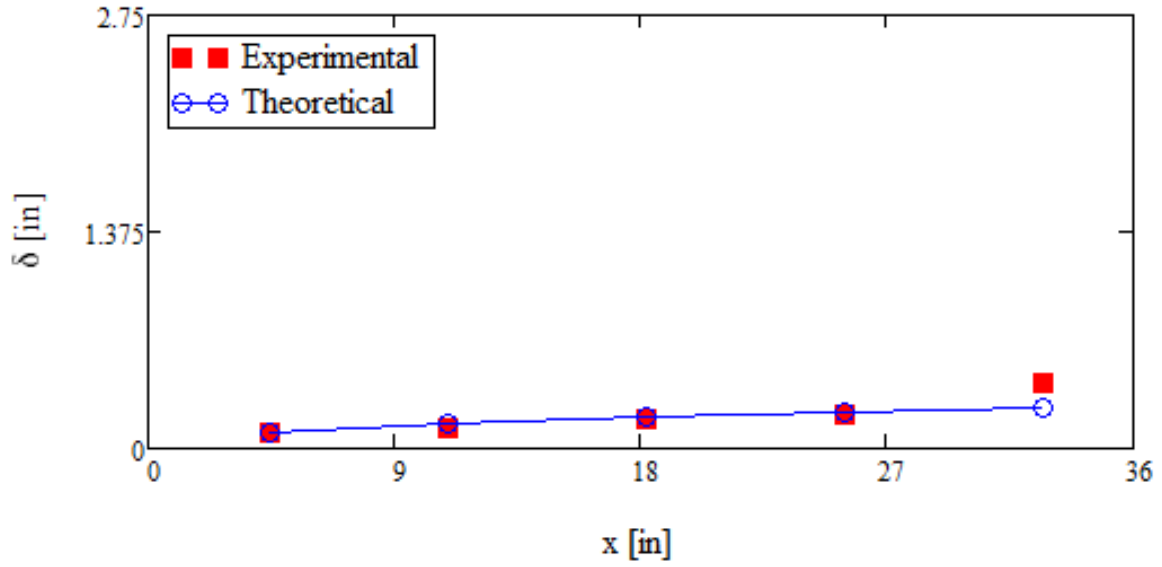
Thermal Boundary Layers

The thermal boundary layer data was analyzed by first determining the offset of the probe from the surface. The same offset values were used as those determined for the velocity boundary layer measurements. The measured temperatures were then nondimensionalized using Eq. (4.14), where θ is the nondimensional temperature, T_{BL} is the temperature measured by the probe, and T_S is the wall/surface temperature at the probe location.

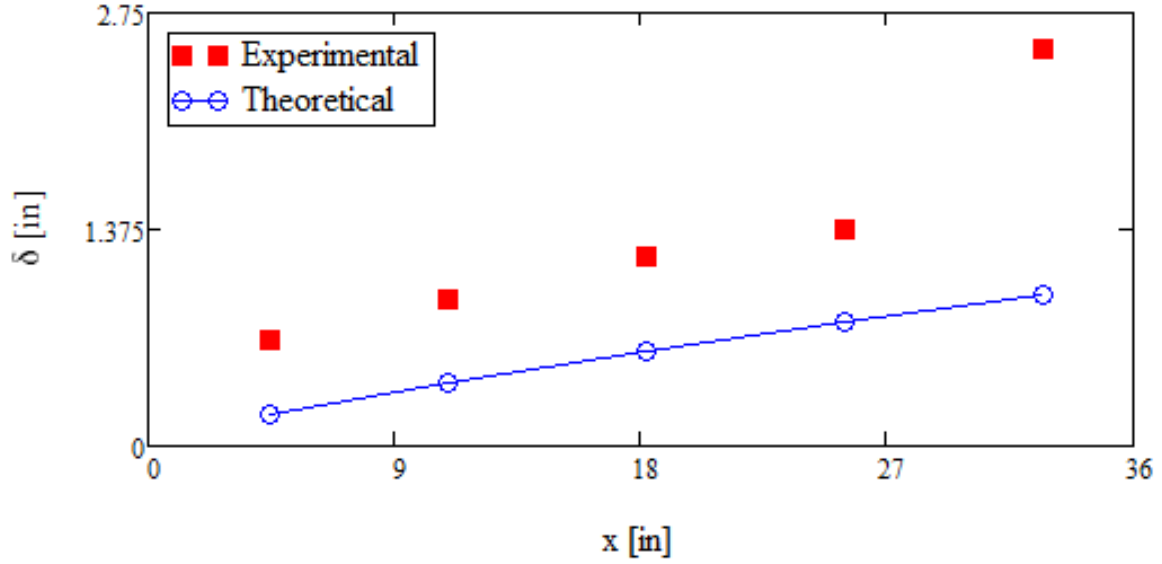
$$\theta = \frac{T_{BL} - T_S}{T_\infty - T_S} \quad (4.14)$$

Since the boundary layer measurements were performed without the IR camera, the surface temperature had to be estimated by using the calculated convective heat transfer coefficients and Eq. (4.13), solving for \overline{T}_{IR} . The boundary layer height was then determined by finding the height at which the nondimensional temperature passed 0.99. Figure 4.7 shows a comparison of the measured thermal boundary layer for the validation cases to the smooth plate correlations presented in Eqs. (2.2) and (2.3), scaled using the calculated Prandtl number to solve for δ_T (see Eq. (2.8)). Figure 4.8 shows the

nondimensional temperature profiles for the smooth laminar and turbulent validations cases.

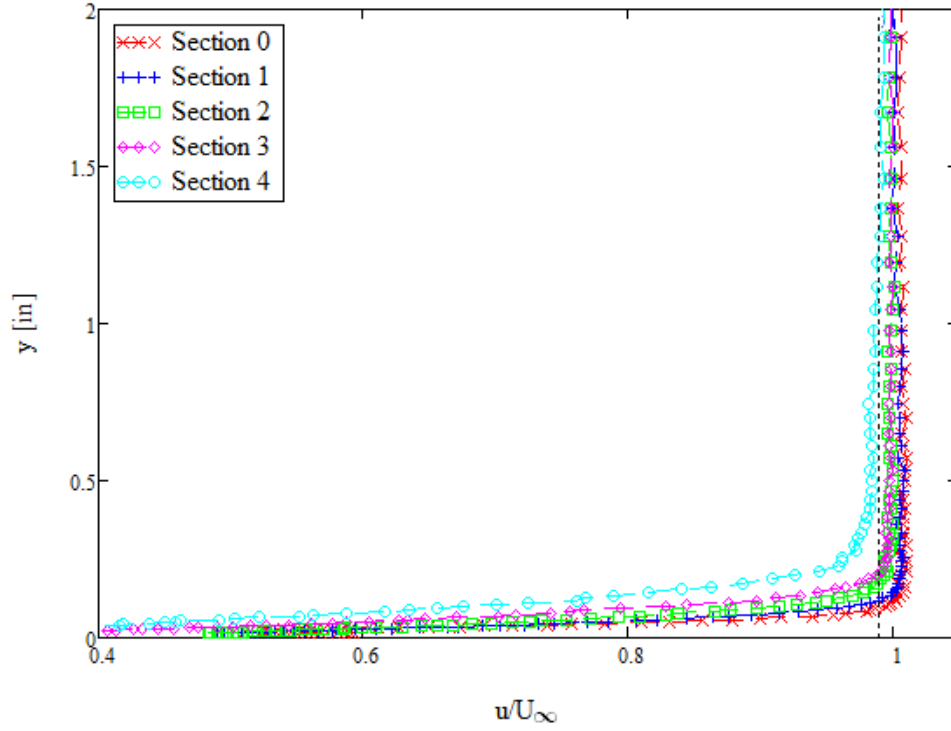


(a) Smooth laminar

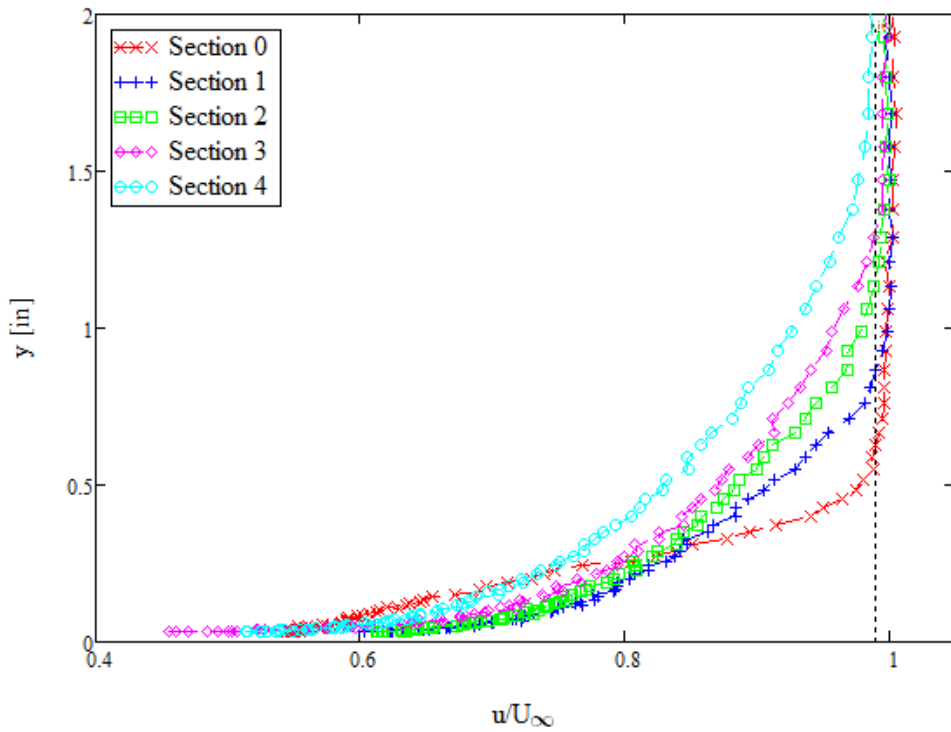


(b) Smooth turbulent

Figure 4.5: Measured and theoretical viscous boundary layer comparisons for the smooth surfaces

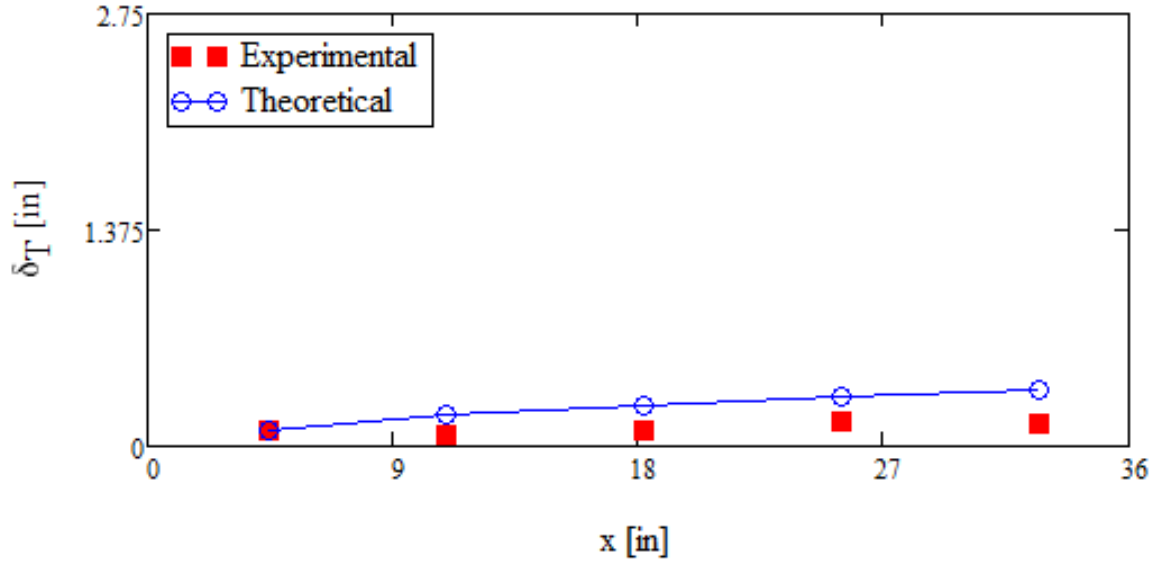


(a) Smooth laminar

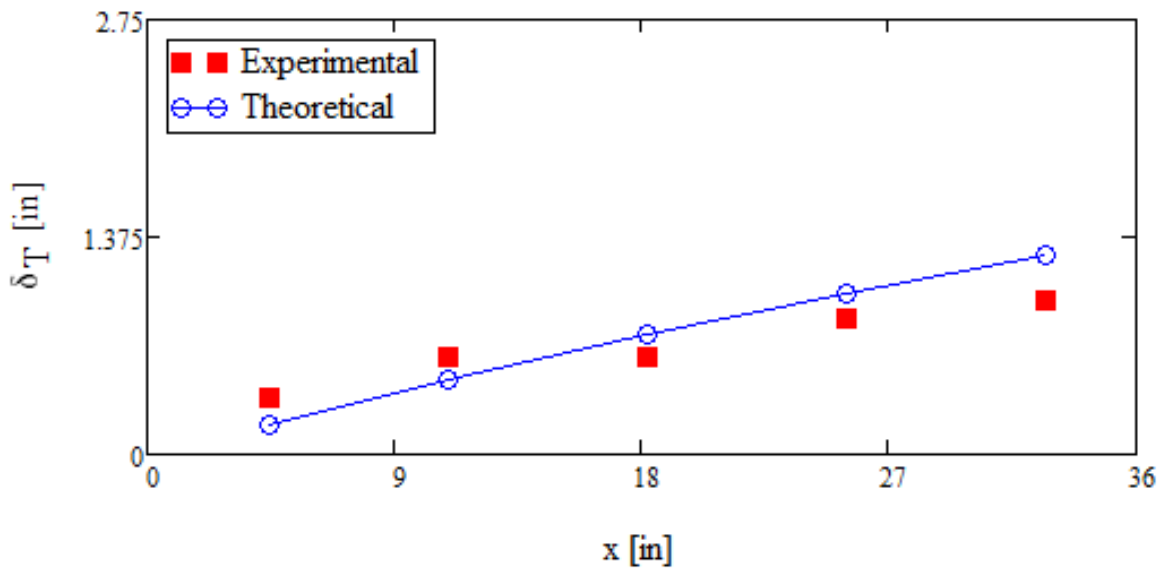


(a) Smooth turbulent

Figure 4.6: Nondimensional velocity profile traces for the smooth surfaces

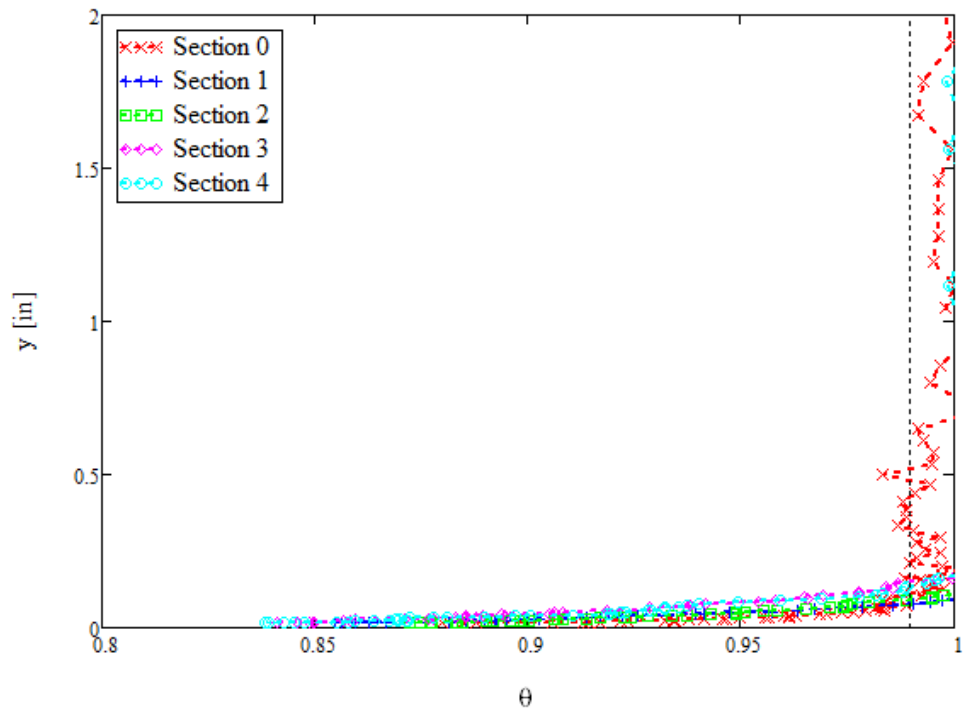


(a) Smooth laminar

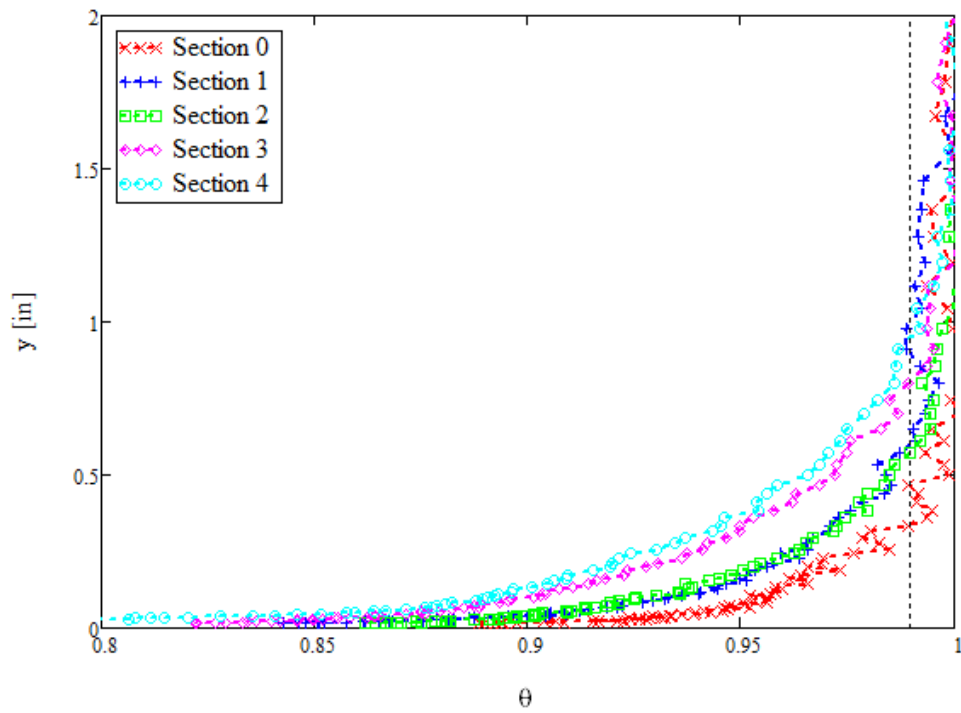


(a) Smooth turbulent

Figure 4.7: Measured and theoretical thermal boundary layer comparisons for the smooth surfaces



(a) Smooth laminar



(a) Smooth turbulent

Figure 4.8: Nondimensional temperature profile traces for the smooth surfaces

In general, the thermal boundary layers developed as expected. The main deviation from the theoretical value occurred on the smooth laminar surface, where a thinner than expected boundary layer was measured. This deviation is likely due to the limitations of the thermocouple probe, which lacked the ability to provide well resolved measurements in a boundary layer as thin as the laminar case. The thermal boundary layer was also affected by the unheated starting length, which delayed the starting point of the boundary layer formation.

CHAPTER FIVE

Results and Discussion

This chapter presents and discusses the results of the convective heat transfer and boundary layer tests on the rough surfaces. The data reduction methods developed in Chapter Four were applied to the raw data which was acquired during these tests.

Convective Heat Transfer Results

Tables 5.1 through 5.4 present the raw data acquired during the convective heat transfer tests for each of the four surfaces (smooth laminar, smooth turbulent, 053096_run1_x10, and 052996_run4_x10). The data is presented at the eight measurement stations shown in Figure 3.4. These tables include the values for each of the variables required to calculate the area averaged convective heat transfer coefficient presented in Eq. (4.13) for a 1" by 1" area centered about each subsurface thermocouple location. All temperatures presented in the tables have been calibrated and corrected. The area averaged convective heat transfer coefficient is also presented, along with the calculated uncertainty.

Figures 5.1 and 5.2 present the local steady state surface temperature and convective heat transfer coefficient maps for the 052996_run4_x10 and 053096_run1_x10 surfaces. Figure 5.3 shows a comparison of the centerline ± 0.5 " spanwise averaged convective heat transfer coefficients for the rough surfaces. The smooth surface theoretical values (see Eqs. (2.10) and (2.11), solved for h) are also shown to illustrate the enhancement provided by the roughness.

Table 5.1: Smooth laminar surface test data

Variable	0a	0b	0c	1a	1b	2	3	4
x (in)	3.1035	4.4785	5.8535	9.2285	10.9785	18.2285	25.4785	32.7285
A_t (in ²)	35.0625	35.0625	35.0625	44.6250	44.6250	44.6250	44.6250	44.6250
ε	0.95	0.95	0.95	0.95	0.95	0.95	0.95	0.95
σ (W/m ² ·K ⁴)	5.67E-08							
t (in)	0.72	0.72	0.72	0.72	0.72	0.72	0.72	0.72
E (V)	4.5273	4.5273	4.5273	4.5171	4.5171	4.5358	4.4923	4.5970
I (A)	1.6356	1.6356	1.6356	2.0881	2.0881	2.0838	2.1212	2.078
T_{SS} (K)	304.23	304.22	304.73	306.02	306.99	306.33	306.94	307.41
T_{UP} (K)	296.45	295.35	295.75	296.34	296.66	297.13	297.51	297.58
T_∞ (K)	294.16	294.16	294.16	294.17	294.17	294.13	293.88	293.66
\overline{T}_{IR} (K)	301.46	302.39	303.41	304.18	304.39	307.19	307.33	306.37
\bar{h} (W/m ² ·K)	28.647± 2.801	23.465± 2.496	20.088± 2.221	17.432± 0.916	16.313± 0.910	12.345± 0.670	11.856± 0.679	12.674± 0.763

Table 5.2: Smooth turbulent surface test data

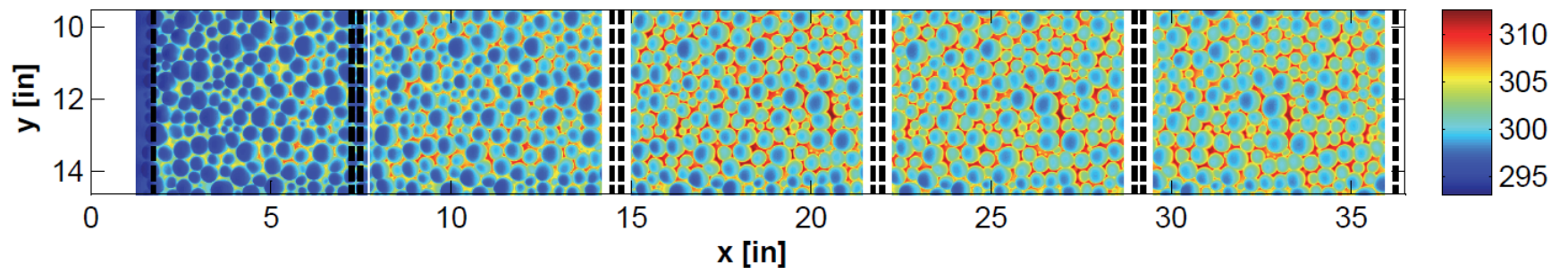
Variable	0a	0b	0c	1a	1b	2	3	4
x (in)	3.1035	4.4785	5.8535	9.2285	10.9785	18.2285	25.4785	32.7285
A_t (in ²)	35.0625	35.0625	35.0625	44.6250	44.6250	44.6250	44.6250	44.6250
ε	0.95	0.95	0.95	0.95	0.95	0.95	0.95	0.95
σ (W/m ² ·K ⁴)	5.67E-08							
t_p (in)	0.72	0.72	0.72	0.72	0.72	0.72	0.72	0.72
E (V)	5.5213	5.5213	5.5213	5.5313	5.5313	5.5966	5.4585	5.6180
I (A)	1.9910	1.9910	1.9910	2.5351	2.5351	2.5065	2.5694	2.4840
T_{SS} (K)	304.45	304.02	304.70	307.40	308.86	307.37	307.64	309.28
T_{UP} (K)	295.30	293.86	294.32	295.11	295.50	296.04	296.49	296.87
T_∞ (K)	292.42	292.42	292.42	292.42	292.42	292.39	292.32	292.75
\overline{T}_{IR} (K)	298.17	299.29	300.48	301.55	301.78	303.61	303.78	303.64
\bar{h} (W/m ² ·K)	69.392± 4.353	50.671± 3.655	42.055± 3.116	34.447± 1.253	32.314± 1.245	27.758± 1.013	27.233± 0.972	27.597± 1.279

Table 5.3: 052996_run4_x10 surface test data

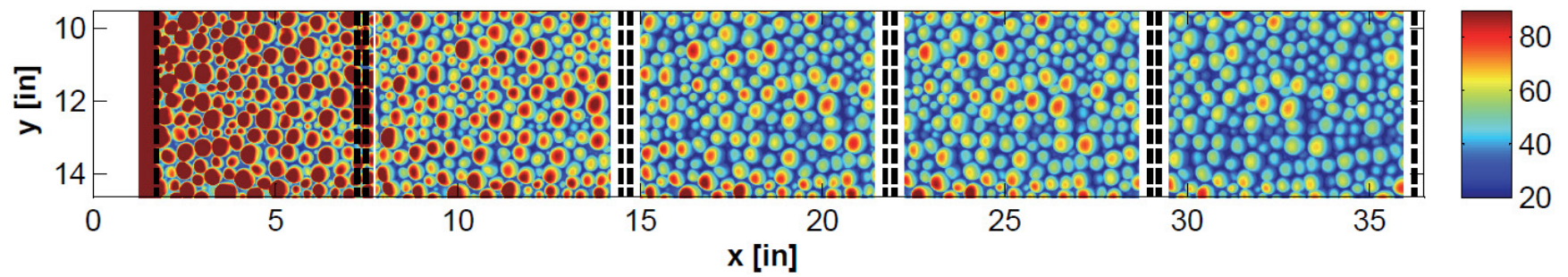
Variable	0a	0b	0c	1a	1b	2	3	4
x (in)	3.1035	4.4785	5.8535	9.2285	10.9785	18.2285	25.4785	32.7285
A_t (in ²)	35.0625	35.0625	35.0625	44.6250	44.6250	44.6250	44.6250	44.6250
ϵ	0.95	0.95	0.95	0.95	0.95	0.95	0.95	0.95
σ (W/m ² ·K ⁴)	5.67E-08							
t_p (in)	0.72	0.72	0.72	0.72	0.72	0.72	0.72	0.72
E (V)	6.1559	6.1559	6.1559	6.1646	6.1646	6.2743	6.1221	6.2370
I (A)	2.2183	2.2183	2.2183	2.8274	2.8274	2.8025	2.8546	2.7890
T_{SS} (K)	310.17	309.85	309.65	309.43	310.35	312.14	310.31	313.20
T_{UP} (K)	296.42	296.00	296.31	295.74	295.93	297.23	297.39	297.95
T_∞ (K)	292.03	292.03	292.03	292.02	292.02	292.07	292.00	291.98
\overline{T}_{IR} (K)	297.64	298.97	299.67	300.86	300.66	301.70	301.98	301.79
\bar{h} (W/m ² ·K)	78.030± 5.202	61.828± 4.233	56.288± 3.838	47.628± 1.645	48.016± 1.675	42.494± 1.512	42.428± 1.411	40.645± 1.852

Table 5.4: 053096_run1_x10 surface test data

Variable	0a	0b	0c	1a	1b	2	3	4
x (in)	3.1035	4.4785	5.8535	9.2285	10.9785	18.2285	25.4785	32.7285
A_t (in ²)	35.0625	35.0625	35.0625	44.6250	44.6250	44.6250	44.6250	44.6250
ϵ	0.95	0.95	0.95	0.95	0.95	0.95	0.95	0.95
σ (W/m ² ·K ⁴)	5.67E-08							
t_p (in)	0.72	0.72	0.72	0.72	0.72	0.72	0.72	0.72
E (V)	5.9179	5.9179	5.9179	5.9039	5.9039	5.9053	5.8447	5.9730
I (A)	2.1184	2.1184	2.1184	2.7052	2.7052	2.7008	2.7303	2.6510
T_{SS} (K)	309.51	310.41	308.08	306.98	308.19	308.80	307.56	310.165
T_{UP} (K)	296.403	295.14	295.46	295.74	296.03	296.91	297.07	297.64
T_∞ (K)	293.06	293.06	293.06	293.18	293.18	293.23	293.30	293.30
\overline{T}_{IR} (K)	307.14	308.90	304.74	302.07	302.35	303.81	303.84	304.35
\bar{h} (W/m ² ·K)	24.377± 1.925	19.615± 1.734	31.041± 2.338	44.327± 1.418	41.788± 1.381	35.575± 1.187	37.051± 1.165	32.855± 1.435

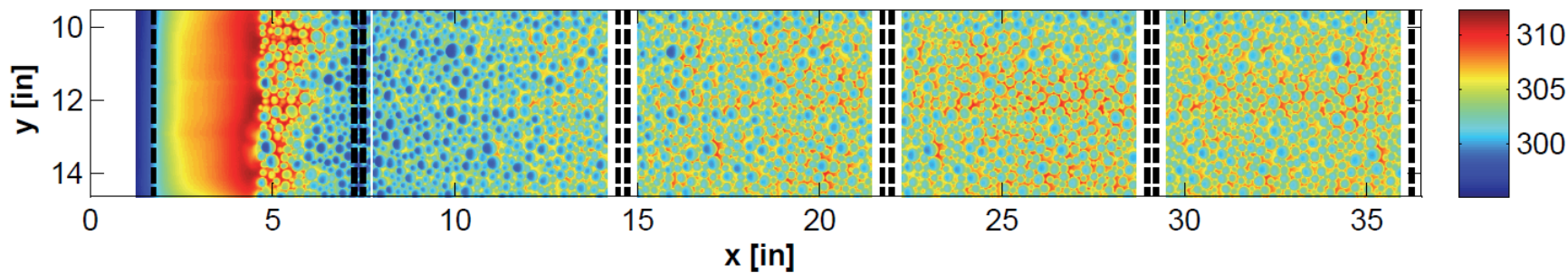


(a) Steady state temperature [K]

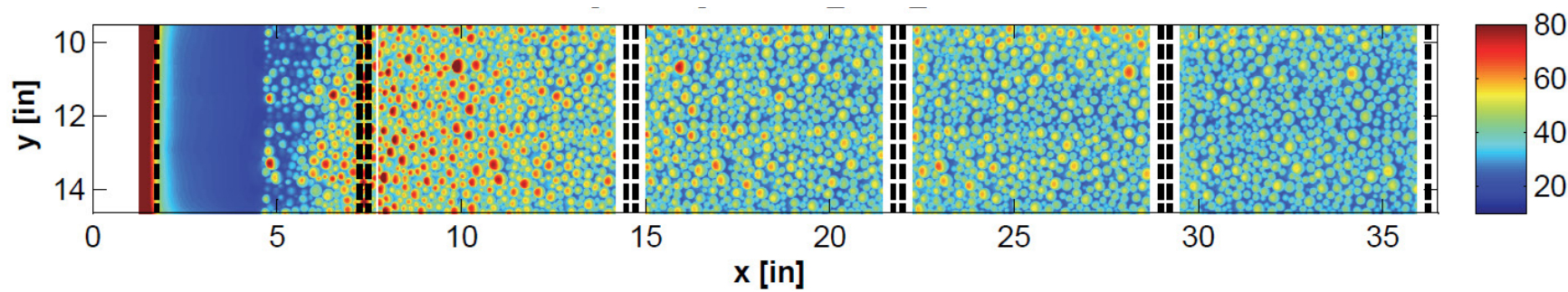


(b) Convective heat transfer [W/m²·K]

Figure 5.1: Surface maps for the 052996_run4_x10 surface

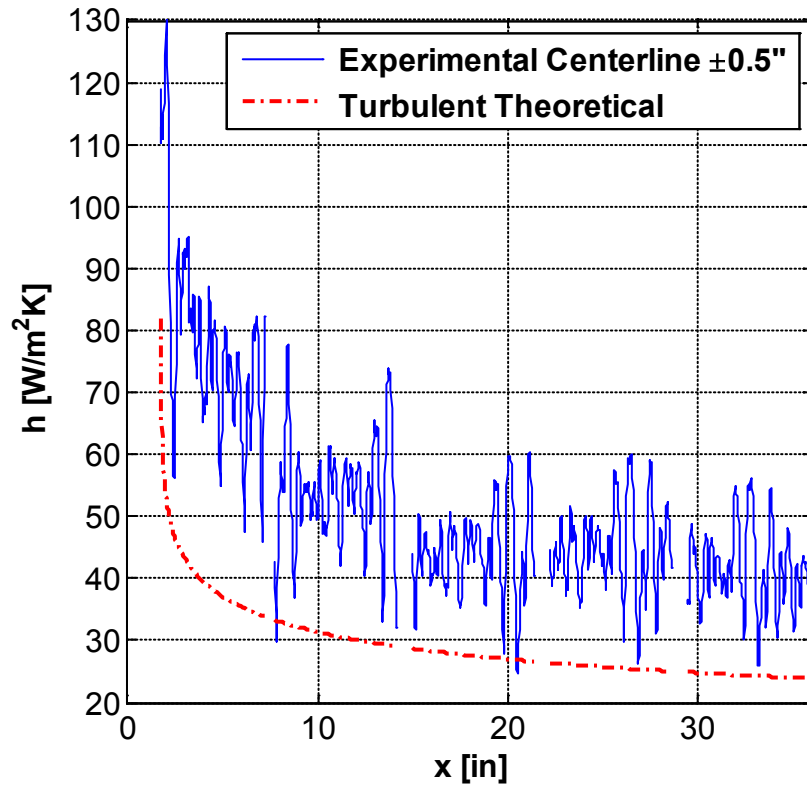


(a) Steady state temperature [K]

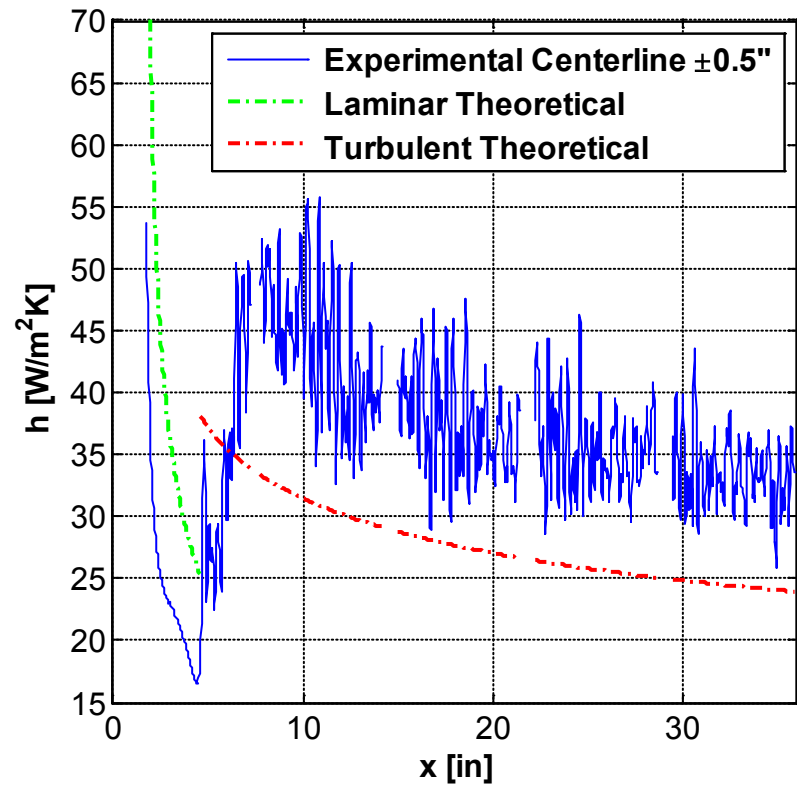


(b) Convective heat transfer [W/m²·K]

Figure 5.2: Surface maps for the 053096_run1_x10 surface



(a) 052996_run4_x10



(b) 053096_run1_x10

Figure 5.3: Centerline $\pm 0.5''$ spanwise averaged convective heat transfer coefficients

Figures 5.1-5.3 reveal several important trends for the rough surfaces. For both surfaces, the roughness elements exhibit higher convective heat transfer on their upstream side than on their downstream side. This is due to flow stagnation on the upstream side and flow separation on the downstream side of the element. Also, the smooth areas (or floor sections) between the roughness elements have drastically lower convective heat transfer rates than the surfaces of the roughness elements; the heat transfer in these areas is even below the expected value for a completely smooth surface at the same x-location. This decrease in heat transfer at the floor section is caused by the separation of the boundary layer from surface due to roughness element flow effects. Although overall convective heat transfer is enhanced on the rough surfaces, it is reduced at the floor of the surface. For both surfaces, taller roughness elements have higher apparent convective heat transfer relative to other elements along the same x-location. Since they protrude further into the boundary layer they experience a fluid temperature closer to the freestream value (see Figure 2.6), providing a larger temperature difference to drive convection.

In general, there is a decrease in the overall convective heat transfer as flow moves away from the leading edge (i.e. as the boundary layers grow). The exception to this is seen on the 053096_run1_x10 surface. Due to the smooth-zone near the leading edge of this surface, the transition from laminar to turbulent flow was captured in the IR images. The convective heat transfer values confirm that the flow begins as laminar before being forced into transition by the roughness. There is also a clear transition region visible in Figures 5.2 and 5.3. As a result, the highest convective heat transfer is seen at the end of the transition region instead of near the leading edge.

Both surfaces also exhibit significant surface temperature variations across the height of the individual roughness elements. This is due to a relatively high roughness element Biot number (on the order of 0.1), indicating resistance to internal conduction across the element height. Due to the difference in both length scale and thermal conductivity between the experimental surface ($k_{ABS} = 0.18 \text{ W/m}\cdot\text{K}$) and actual ice roughness ($k_{ICE} = 2.25 \text{ W/m}\cdot\text{K}$) [11], the surface temperatures would not be expected to vary as greatly along the height of actual ice roughness elements. This is best illustrated by a comparison of the Biot numbers between the experimental roughness (Bi_{ABS}) and actual ice roughness (Bi_{ICE}). This comparison is shown in Eq. (5.1), where the characteristic length for Bi_{ABS} is ten times greater than the characteristic length for Bi_{ICE} due to the Reynolds number scaling.

$$\frac{Bi_{ICE}}{Bi_{ABS}} = \frac{hL_{c,ICE}}{k_{ICE}} \frac{k_{ABS}}{hL_{c,ABS}} = \frac{k_{ABS}}{10k_{ICE}} = 0.008 \approx 0.01 \quad (5.1)$$

Although the value for the convective heat transfer coefficient will vary slightly between the Bi_{ICE} and Bi_{ABS} cases, it is assumed to be constant in this comparison since the magnitude of this change would be negligible when compared to the effects of the length scale and thermal conductivity.

This comparison indicates that the Biot number for actual ice roughness elements would be two orders of magnitude (0.01) below the experimental roughness surfaces (on the order of 0.001). As a result, much smaller temperature gradients would develop along the surface of the actual ice roughness elements, leading to less variation in the surface temperature across the height of individual elements. Further, the decreased resistance to internal conduction for actual ice roughness would lead to higher overall surface temperatures. As a result, the convective heat transfer from actual ice roughness

elements would be higher than the values measured for the experimental roughness elements.

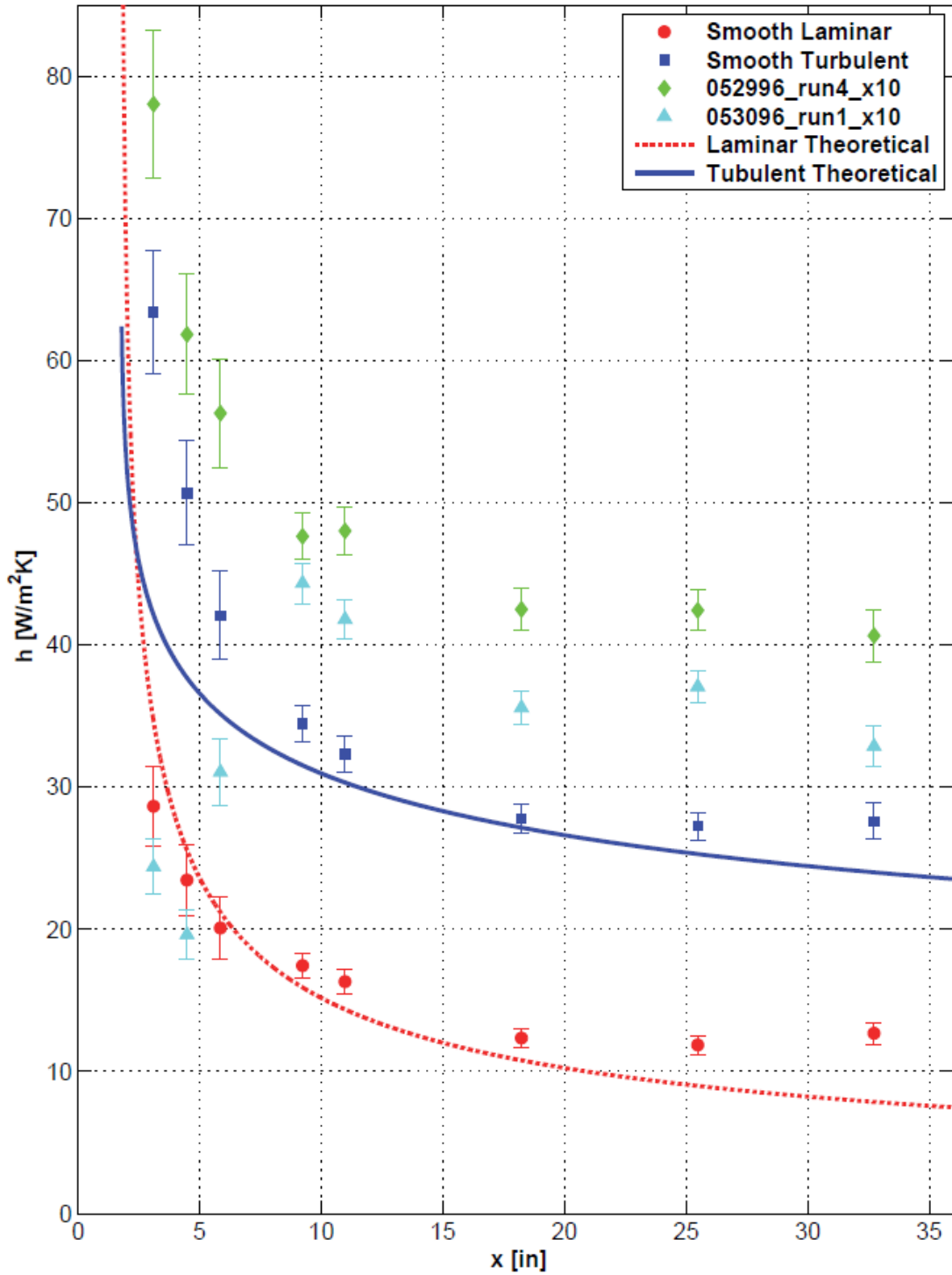


Figure 5.4: Area averaged convective heat transfer coefficient comparison

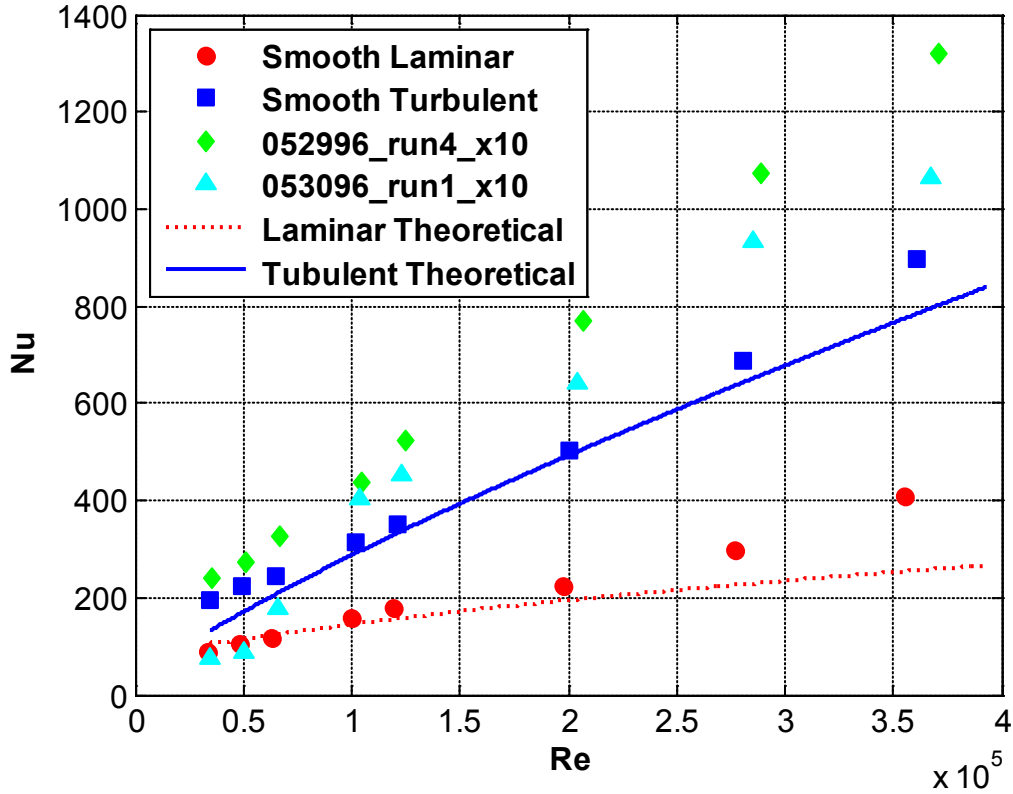


Figure 5.5: Nondimensional convective heat transfer coefficient comparison

Figure 5.4 shows a comparison of the eight area averaged convective heat transfer coefficients for each of the four surfaces compared to the laminar and turbulent smooth plate correlations. Figure 5.5 shows the same information as Figure 5.4, but nondimensionalized as Nusselt number versus Reynolds number. Figures 5.4 and 5.5 show that the area averaged values capture the important trends noted from the detailed maps of Figures 5.1 and 5.2. As expected, the 052996_run4_x10 surface had the highest convective heat transfer at every point since it also had the largest roughness elements. For the 053096_run1_x10 surface, the first two points are clearly laminar, while the third point is in the transition region. After the first three points, the flow is fully turbulent and the values trend above the smooth turbulent surface but below the 052996_run4_x10 surface.

Convective Heat Transfer Enhancement

The convective heat transfer enhancement provided by the surface roughness at each of the eight points in Figure 5.4 was calculated using the turbulent smooth plate value as a baseline (\bar{h}/h_{smooth}). These values were compared to the enhancement values reported by Mart [33] for hemispherical ABS and aluminum roughness elements. Figure 5.6 shows the calculated enhancement values compared to the values of Mart [33] across a range of Reynolds number. An enhancement value above one indicates greater convective heat transfer than the smooth surface.

The enhancement from the 052996_run4_x10 surface agrees well with the ABS elements of Mart [33]. This is reasonable since the surfaces have roughly the same average element diameter (10.37 mm vs. 9.53 mm) and are manufactured from the same material, leading to well matched Biot numbers. However, it is also a somewhat surprising result since the elements on the 052996_run4_x10 surface are much more closely packed than the elements of Mart [33]. Although the sparse ABS roughness distribution of Mart [33] captures the magnitude of enhancement provided by the 052996_run4_x10 surface due to well matched element size and Biot numbers, the mechanisms for enhancement are very different. The sparse spacing of the roughness elements of Mart [33] allowed the formation of a flow separation and reattachment region directly behind each roughness element at the surface floor. This reattachment region accounted for a significant amount of the convective heat transfer enhancement from the surface. The much closer spacing of the roughness elements in the current investigation does not allow the formation of a reattachment region. As previously noted, the surface floor between the roughness elements actually exhibits a reduction in convective heat

transfer. The main mechanism for enhancement for the roughness distributions of the current investigation is from the roughness elements themselves, which are much more densely spaced than those of Mart [33]. As expected, the 053096_run1_x10 surface provides the least enhancement since it has the smallest elements.

The aluminum elements of Mart [33] exhibit the highest convective heat transfer enhancement. This is because the aluminum elements have a much higher thermal conductivity ($k_{Al} = 180 \text{ W/m}\cdot\text{K}$) than the ABS elements; consequently, the Biot number is three orders of magnitude lower than for the ABS elements. This supports the conclusion that a distribution of actual ice roughness would exhibit a higher magnitude of convective heat transfer than the tested surfaces due to a much lower Biot number.

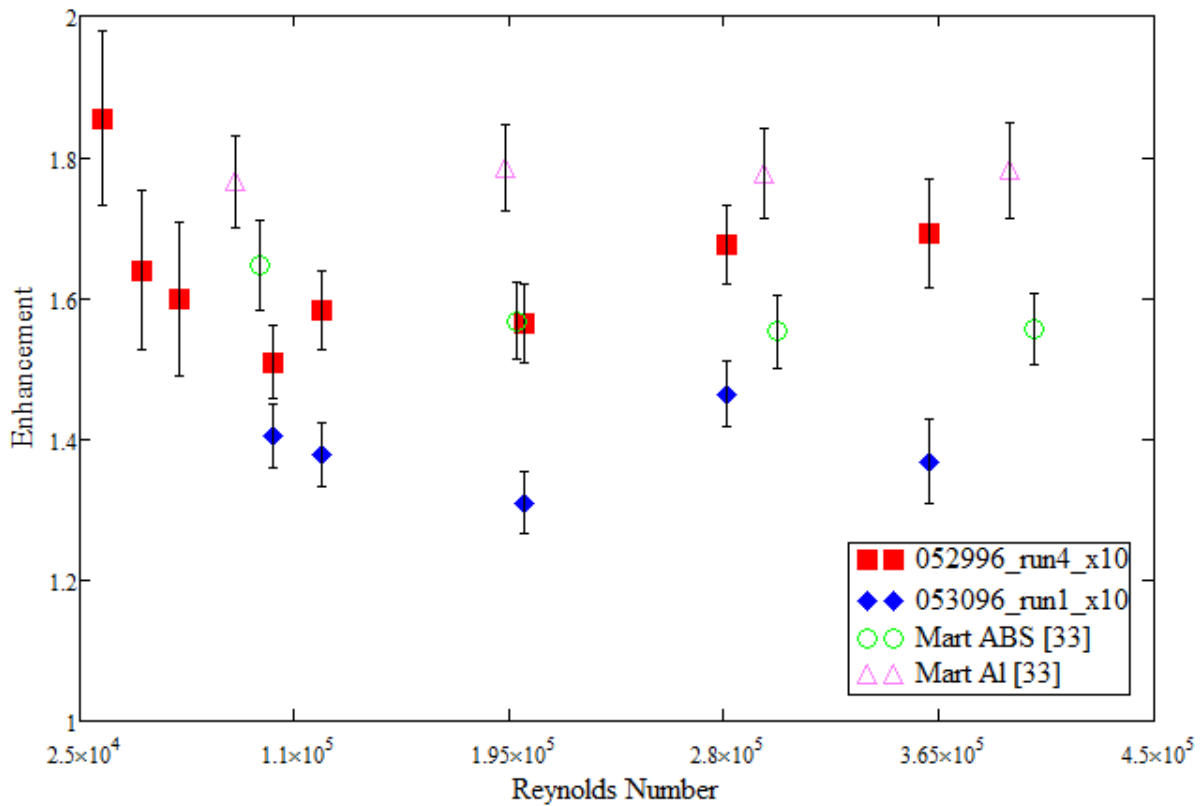
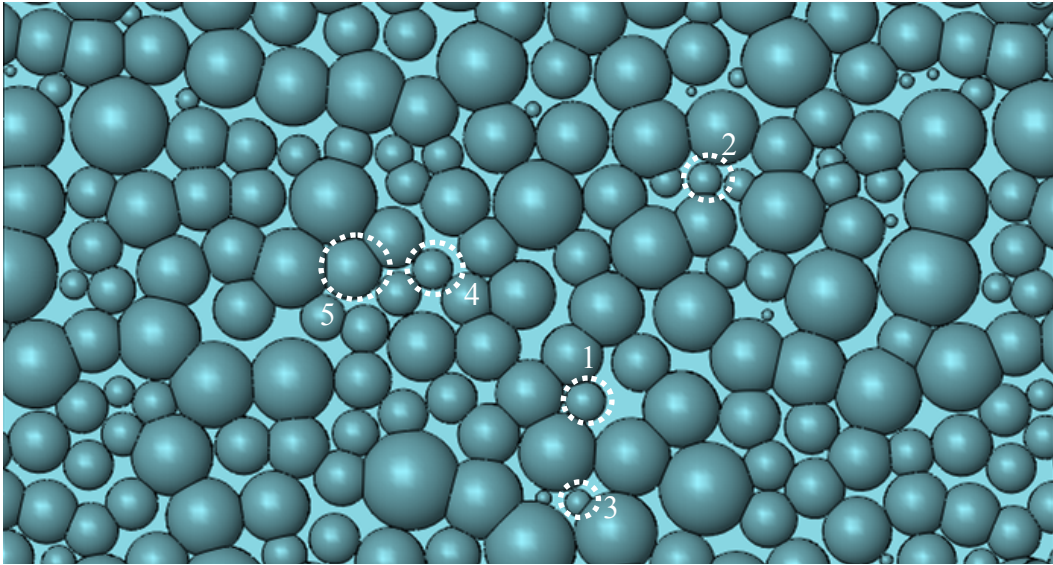


Figure 5.6: Convective heat transfer enhancement comparison

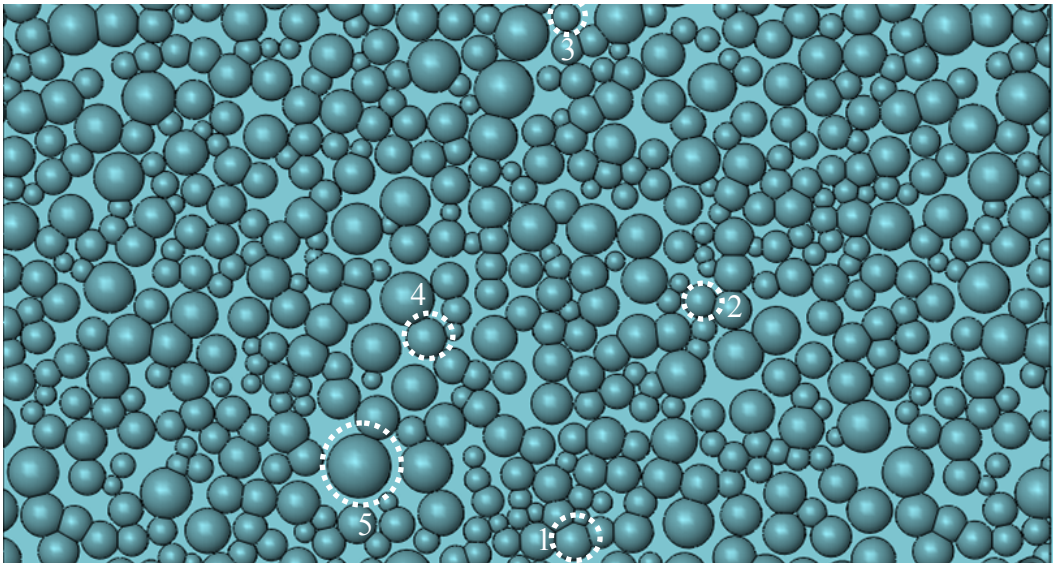
Element Interaction Effects

Since the largest roughness elements on the 053096_run1_x10 surface were about the same size as the smallest elements on the 052996_run4_x10 surface, a study of the importance of relative element height and element-to-element interaction on heat transfer could be performed. Taking a representative section of roughness from the second heated section, a comparison of similar elements was made between the two rough surfaces. Five pairs of similar elements were selected from each surface by approximately matching both the element height and x-location on the plate. Figure 5.7 shows the element locations on each surface and identifies each pair with a reference number. This figure also shows the size and location of the element relative to neighboring elements. Tables 5.5 and 5.6 show the element height, x-location, and the maximum local convective heat transfer coefficient on the element.

Element pairs 1 through 4 have nearly identical convective heat transfer values (within 10% of each other). This is in spite of the fact that the elements on the 052996_run4_x10 surface were surrounded by much larger upstream elements. This indicates that the impact of larger upstream elements on relatively small elements is negligible. The only major difference is seen in element pair 5, where the convective heat transfer from the 053096_run1_x10 surface is much higher. This is likely because it is one of the largest elements on the surface. This indicates that there are localized areas on the surfaces where element interaction is important, especially when the element is relatively large.



(a) 052996_run4_x10 element locations and number



(a) 053096_run1_x10 element locations and number

Figure 5.7: Element pair locations, flow is from left to right

Table 5.5: 052996_run4_x10 element data

Reference Number	Height (in)	x-location (in)	h (W/m ² ·K)
1	0.138	11.49	49.1
2	0.117	12.31	55.3
3	0.0907	11.45	39.8
4	0.139	10.44	58.6
5	0.213	9.92	65.5

Table 5.6: 053096_run1_x10 element data

Reference Number	Height (in)	x-location (in)	h (W/m ² ·K)
1	0.136	11.44	52.8
2	0.115	12.30	56.4
3	0.0969	11.38	39.1
4	0.140	10.42	64.4
5	0.220	9.94	93.2

Heat Loss Modes

An analysis of the heat loss due to each mode was also conducted to study their relative importance; the results are shown in Table 5.7 for average values. The heat lost through conduction is relatively constant for the three turbulent cases and is largest for the laminar case, where convection is the least aggressive. As the surface roughness height increases, the convective heat transfer increases at the expense of radiation. The results also confirm the importance of accounting for the radiation and conduction heat losses in the data reduction equations.

Table 5.7: Percentage of heat transfer by mode

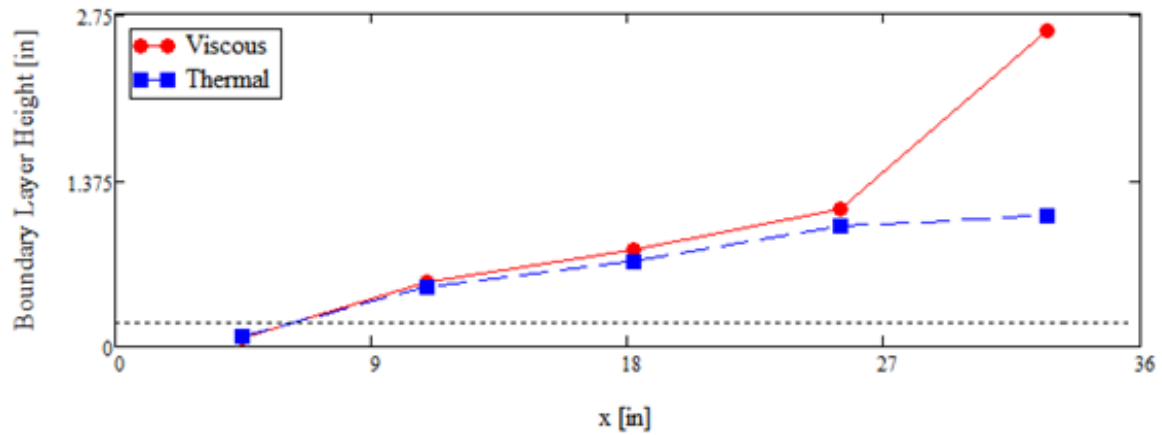
Surface	Radiation (at the surface)	Conduction (through Plexiglas)	Convection (at the surface)
Smooth laminar	18.55%	27.74%	53.71%
Smooth turbulent	10.57%	22.82%	66.61%
053096_run1_x10	11.96%	22.06%	65.98%
052996_run4_x10	7.76%	22.79%	69.45%

Boundary Layer Results

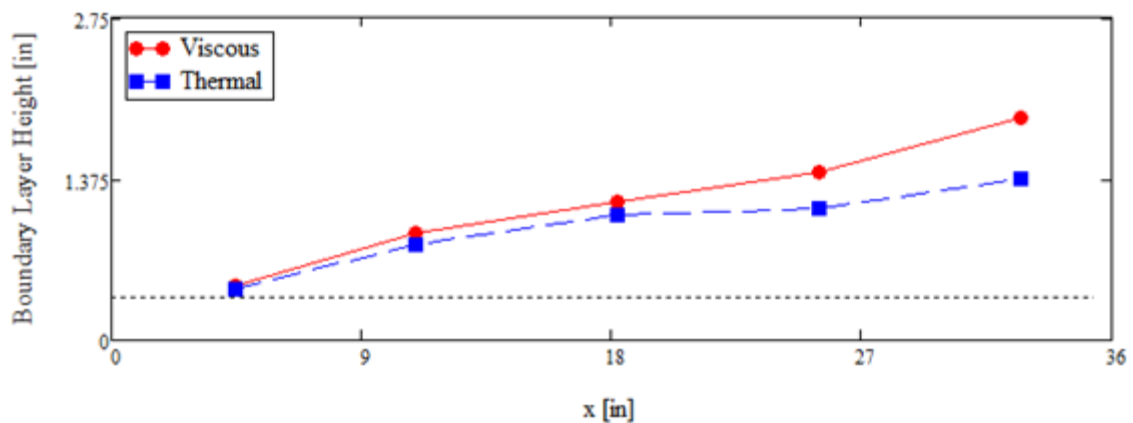
The results of the viscous and thermal boundary layer analysis for the rough surfaces are presented in Figure 5.8, with the average roughness height indicated by the horizontal dashed lines. In general, the viscous boundary layers developed as expected along the rough surfaces. The 053096_run1_x10 surface exhibits laminar behavior at the first station before transitioning to turbulent flow. Both surfaces exhibit a flow interaction with the flap in the last heated section, indicated by a spike in the boundary layer height. The thermal boundary layers also developed as expected, with the 053096_run1_x10 surface again exhibiting both laminar and turbulent behavior. The thermal boundary layer is slightly thinner than the viscous boundary layer due to the unheated starting length, which delays the start of the thermal boundary layer. Figure 5.9 provides a comparison of the measured viscous and thermal boundary layer thicknesses for each of the four surfaces tested.

Figures 5.10 and 5.11 show the nondimensional velocity and temperature profile traces for each of the rough surfaces. The average element height is indicated by the horizontal dashed line and the vertical dashed line indicates the 0.99 threshold. Note that

for section 0 on the 053096_run1_x10 surface (located near the transition point) the velocity boundary layer trace does not indicate a clear height; therefore, the boundary layer was assumed to end at the first measured point. This velocity profile indicates flow acceleration in the smooth region of this surface caused by the upstream roughness elements. This flow acceleration also explains the slightly lower than expected convective heat transfer seen in the laminar region of Figures 5.3(b) and 5.4 for the 053096_run1_x10 surface.

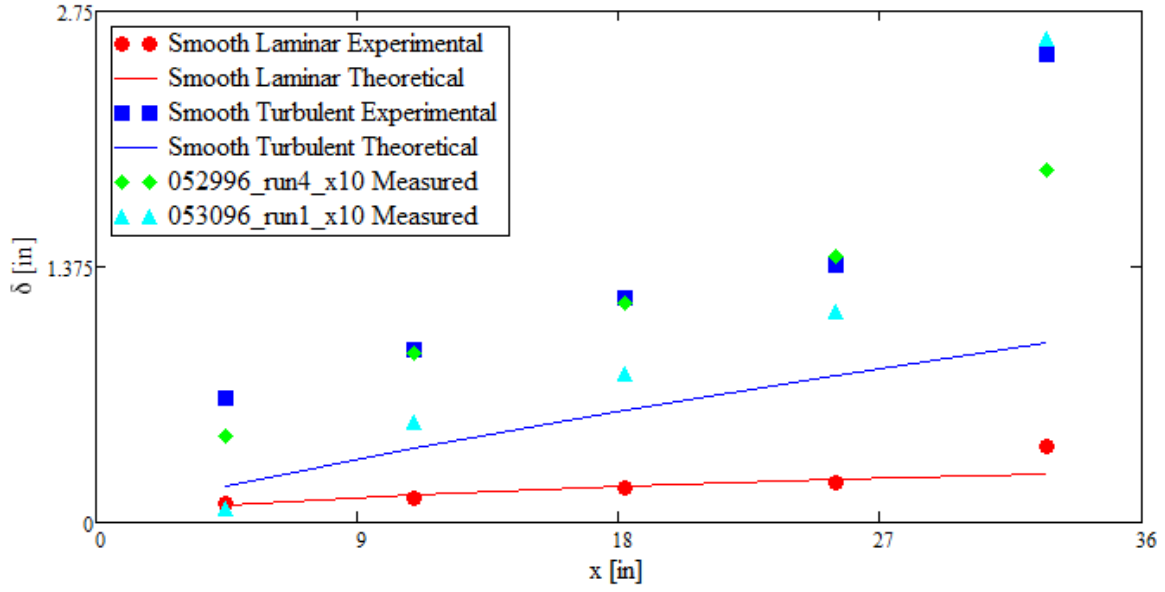


(a) 053096_run1_x10

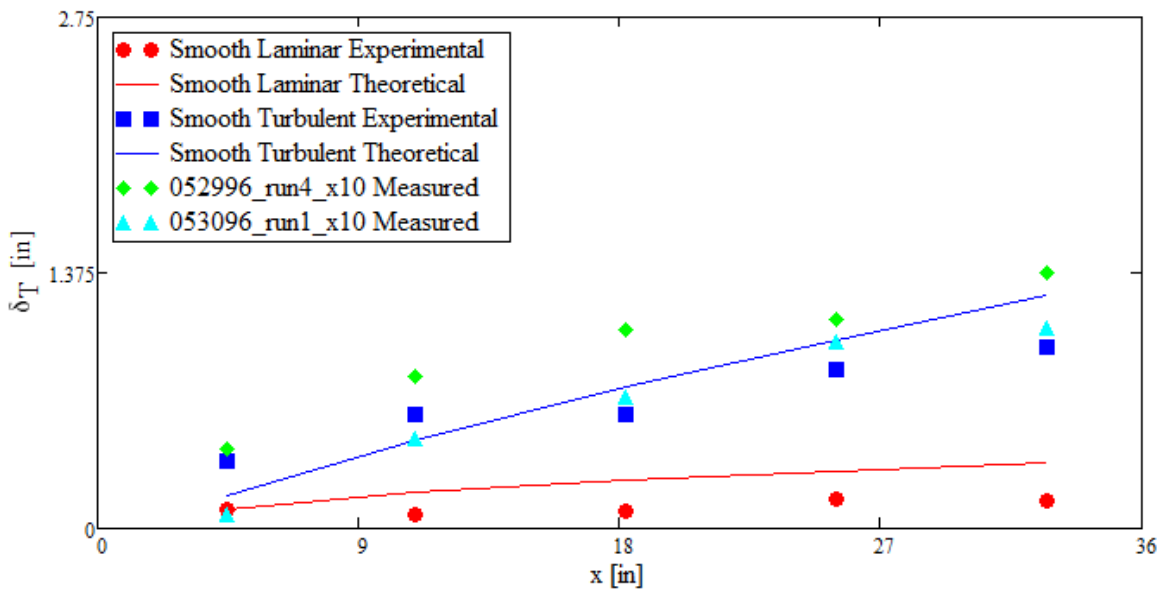


(b) 052996_run4_x10

Figure 5.8: Viscous and thermal boundary layer thicknesses for the rough surfaces

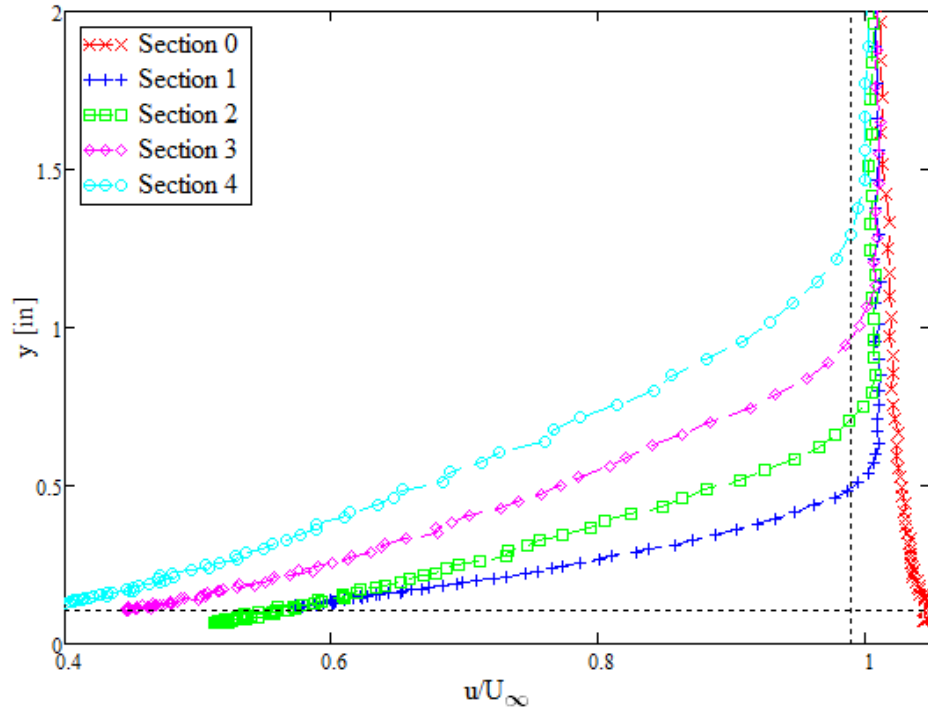


(a) Viscous boundary layers

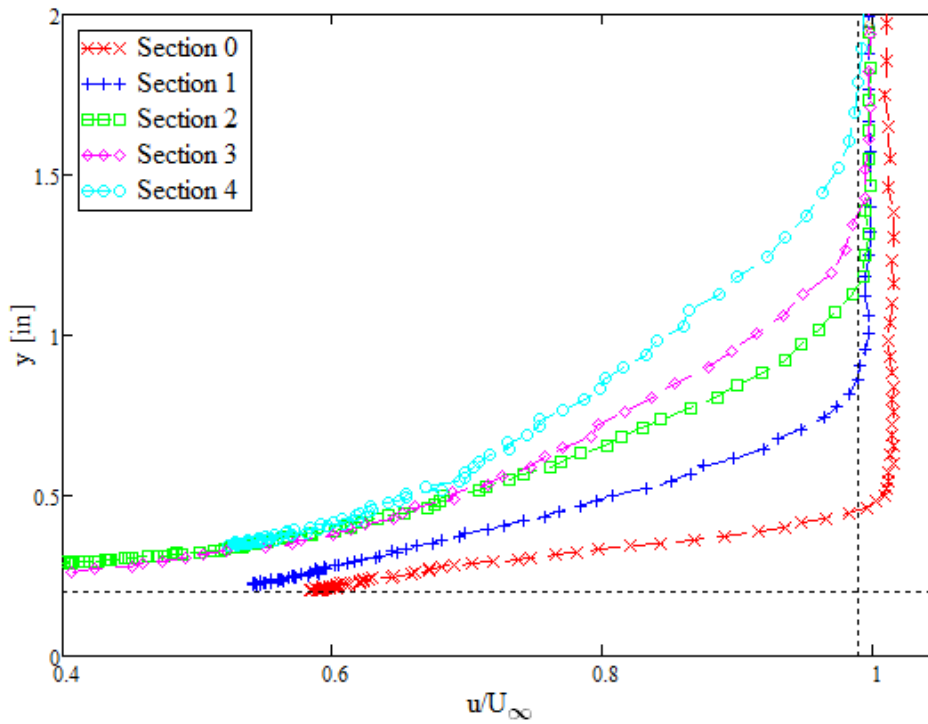


(b) Thermal boundary layers

Figure 5.9: Viscous and thermal boundary layer thicknesses comparison for all surfaces

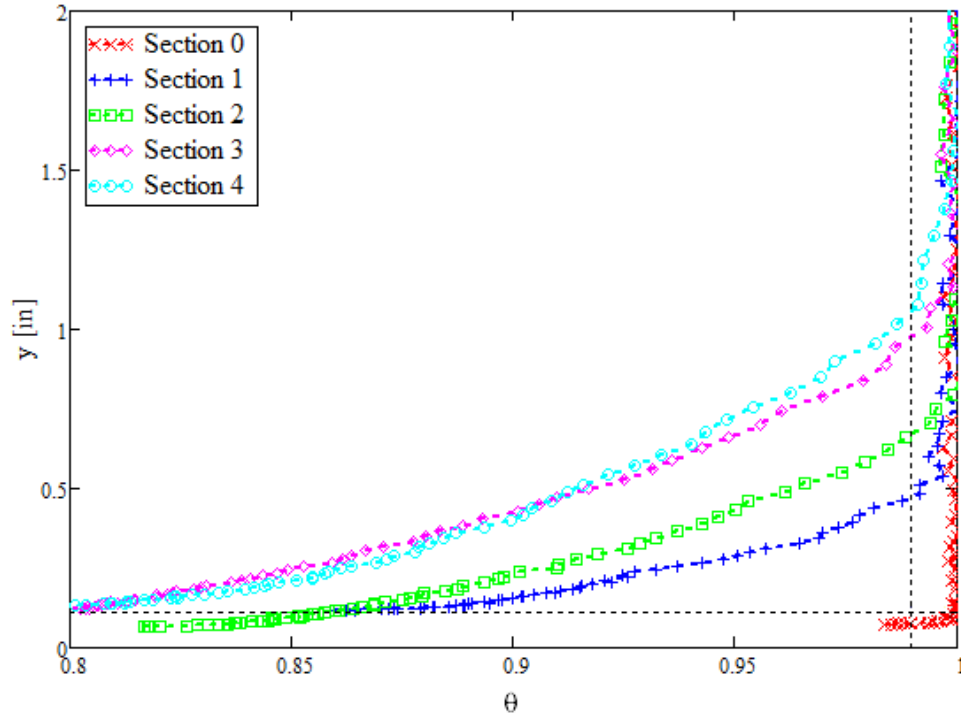


(a) 053096_run1_x10

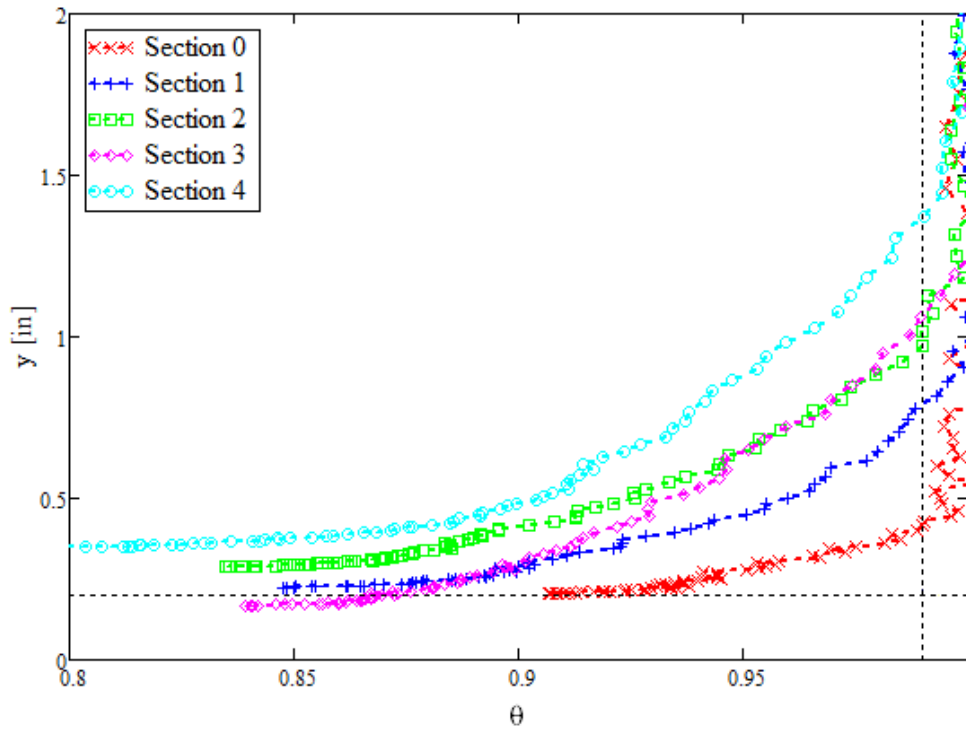


(b) 052996_run4_x10

Figure 5.10: Nondimensional velocity profile traces for the rough surfaces



(a) 053096_run1_x10



(b) 052996_run4_x10

Figure 5.11: Nondimensional temperature profile traces for the rough surfaces

CHAPTER SIX

Conclusions

In this chapter, a summary of the current work is provided. Suggestions for future work are also discussed.

Summary of Current Work

The convective heat transfer behavior of two surfaces exhibiting realistic Appendix C ice roughness distributions was investigated. The rough surfaces were generated using a Lagrangian droplet simulator which modeled the droplet impingement and coalescence processes during ice roughness formation. A steady state experiment was then employed to acquire the data necessary to calculate convective heat transfer coefficients across the rough surfaces. Using an IR camera, detailed surface maps of convective heat transfer coefficients were calculated. The development of the viscous and thermal boundary layers across the surfaces was also characterized using boundary layer traces. The information gathered during the course of this investigation marks the first attempt to characterize both the local convective heat transfer behavior and boundary layer development from surfaces exhibiting realistic ice roughness. The major findings of this study are as follows:

- Convective heat transfer decreases with increasing distance from the leading edge due to boundary layer growth. The exception is in the case of smooth to rough transition, where convective heat transfer is highest at the end of the flow transition region.

- The presence of densely packed surface roughness causes an overall increase in convective heat transfer, but can cause localized decreases at the surface floor due to boundary layer separation.
- Although the trends observed in this study are expected to match those of actual ice roughness, the magnitude of the convective heat transfer enhancement is lower than expected due to poorly matched Biot numbers between the ABS surfaces and actual ice.
- A comparison to Mart [33] indicates that the use of sparse roughness distributions may be sufficient to capture area averaged convective heat transfer values when the Biot number is well matched. However, this approach neglects local roughness effects on convective heat transfer, which are important in predicting the ice accretion process. It also neglects the physical mechanism of convective heat transfer enhancement.

Recommendations for Future Work

The results and conclusions from this study provide a good basis for future work on convective heat transfer from realistic ice roughness distributions. Several variations could be made to the experimental setup to gather additional data:

- The effects of an unheated starting length and varying heat fluxes along an airfoil could be studied by using different power settings for each heated area.
- Tests could be performed with an accelerating flow profile matched to a NACA 0012 airfoil by adding an insert to the wind tunnel ceiling.
- In addition to matching the Reynolds number, the Biot number could also be matched to better capture the effects of internal roughness element conduction on

convective heat transfer. This can be accomplished by manufacturing the roughness surfaces from a material with a higher thermal conductivity, such as aluminum.

- Additional surface distributions must also be tested. These surfaces could be generated using the same methods as described in this study; however, there is room for improvement in this technique. Although the surfaces tested in this investigation were based upon the best data available, the methods used to measure ice roughness data by Anderson et al. [23] were purely visual and somewhat subjective, with an uncertainty of $\pm 20\%$ in some parameters. NASA is currently developing a method to capture actual ice roughness formed on airfoils in the NASA IRT using a 3D scanning technique [39]. Preliminary results have shown the ability to capture more accurate, resolved roughness distribution surface data. The data from these scans could be manipulated and manufactured into testable surfaces. This will add more realism to the experiments by accounting for the evolution of ice roughness along an airfoil surface.
- CFD simulations could be implemented to determine the effects of varying roughness distribution parameters (element size, element spacing, etc.) once more experimental data has been collected to validate the simulations.

By building upon the results of this investigation a more rigorous correlation for the effects of convective heat transfer from ice roughness can be developed and implemented to improve the predictive capabilities of ice accretion codes.

APPENDICES

APPENDIX A

Data Reduction MATLAB Code

This appendix contains the MATLAB code used to perform the convective heat transfer coefficient data reduction for the smooth laminar surface test data. Similar code was used for the other surfaces.

```

% Data Analysis for Smooth Plate Laminar Test Case
% Steady state convective heat transfer test
% Written by: Logan Tecson
% Date: 12/3/12

clear all
close all
clc

%% Constants %%%%%%%%%%%%%%%%%%%%%%%%%%%%%%%%%%%%%%%%%%%%%%%%%%%%%%%%%%%%%%%%%%%%%%%%%
% Pixel area [m^2] (0.02" x 0.02")
A_p = 2.58064e-7;
% Total heated area [m^2] (5.5in X 6.375in and 7in X 6.375in)
A_t = [0.02262092, 0.02879026, 0.02879026, 0.02879026, 0.02879026];
% Plexiglas thickness [m]
t_p = 0.018288;
% Plexiglas thermal conductivity [W/mK]
k_p = 0.18;
% Unheated started length [in]
zeta = 1.7285;
% Surface emissivity (flat black spray paint)
eps = 0.95;
% Stefan-Boltzman constant [W/m^2K^4]
sig = 0.000000567;
% Transmissivity
tau = 0.82;

%% Set up the imaging grid in real coordinates %%%%%%%%%%%%%%%%%%%%%%%%%%%%%%%%%%%%%%%%%%%%%%%%%%%%%%%%%%%%%%%%%%%%%%%%%
% Pixel to inch conversions were determined by using the screw holes
% visible in the IR images of heated section 0
IPP = 4/200; % [inch/pixel]
PPI = 200/4; % [pixel/inch]

x_ref = 305; % reference pixel (screw hole centerline)
x_span = 320; % pixel span in x-axis

% Heated section 0 x-direction grid [in]
x_0_start = 7.3535 - x_ref*IPP;
x_0_end = 7.3535 + (x_span - x_ref)*IPP;
x_0 = linspace(x_0_start, x_0_end, x_span);

% Heated section 1 x-direction grid [in]
x_1_start = 13.8535 - x_ref*IPP;
x_1_end = 13.8535 + (x_span - x_ref)*IPP;
x_1 = linspace(x_1_start, x_1_end, x_span);

% Heated section 2 x-direction grid [in]
x_2_start = 21.1035 - x_ref*IPP;
x_2_end = 21.1035 + (x_span - x_ref)*IPP;
x_2 = linspace(x_2_start, x_2_end, x_span);

```

```

% Heated section 3 x-direction grid [in]
x_3_start = 28.3535 - x_ref*IPP;
x_3_end   = 28.3535 + (x_span - x_ref)*IPP;
x_3       = linspace(x_3_start, x_3_end, x_span);

% Heated section 4 x-direction grid [in]
x_4_start = 35.6035 - x_ref*IPP;
x_4_end   = 35.6035 + (x_span - x_ref)*IPP;
x_4       = linspace(x_4_start, x_4_end, x_span);

y_ref = 24; % reference pixel (top screw hole centerline)
y_span = 256; % pixel span in y-axis

% Universal y-direction grid
y_start = 10 - y_ref*IPP;
y_end   = 10 + (y_span - y_ref)*IPP;
y       = linspace(y_start, y_end, y_span);

%% Import IR image data %%%%%%%%%%%%%%%%%%%%%%%%%%%%%%%%%%%%%%%%%%%%%%%%%%%%%%%%%%%%%%%%%%%%%%%%%%
% Images were previously analyzed and averaged using a separate MATLAB
% function. Temperatures are converted from C to K
% _Cal = calibration and _SS = steady state
% Heated section 0
Pos_0_Cal = dlmread('H:\TEST DATA\IR Videos\Smooth Plate Laminar
(113012)\Pos_0_Cal.txt');
Pos_0_SS = dlmread('H:\TEST DATA\IR Videos\Smooth Plate Laminar
(113012)\Pos_0_SS.txt');
Pos_0_Cal = Pos_0_Cal + 273.15;
Pos_0_SS = Pos_0_SS + 273.15;

% Heated section 1
Pos_1_Cal = dlmread('H:\TEST DATA\IR Videos\Smooth Plate Laminar
(113012)\Pos_1_Cal.txt');
Pos_1_SS = dlmread('H:\TEST DATA\IR Videos\Smooth Plate Laminar
(113012)\Pos_1_SS.txt');
Pos_1_Cal = Pos_1_Cal + 273.15;
Pos_1_SS = Pos_1_SS + 273.15;

% Heated section 2
Pos_2_Cal = dlmread('H:\TEST DATA\IR Videos\Smooth Plate Laminar
(113012)\Pos_2_Cal.txt');
Pos_2_SS = dlmread('H:\TEST DATA\IR Videos\Smooth Plate Laminar
(113012)\Pos_2_SS.txt');
Pos_2_Cal = Pos_2_Cal + 273.15;
Pos_2_SS = Pos_2_SS + 273.15;

% Heated section 3
Pos_3_Cal = dlmread('H:\TEST DATA\IR Videos\Smooth Plate Laminar
(113012)\Pos_3_Cal.txt');
Pos_3_SS = dlmread('H:\TEST DATA\IR Videos\Smooth Plate Laminar
(113012)\Pos 3 SS.txt');

```

```

Pos_3_Cal = Pos_3_Cal + 273.15;
Pos_3_SS = Pos_3_SS + 273.15;

% Heated section 4
Pos_4_Cal = dlmread('H:\TEST DATA\IR Videos\Smooth Plate Laminar
(113012)\Pos_4_Cal.txt');
Pos_4_SS = dlmread('H:\TEST DATA\IR Videos\Smooth Plate Laminar
(113012)\Pos_4_SS.txt');
Pos_4_Cal = Pos_4_Cal + 273.15;
Pos_4_SS = Pos_4_SS + 273.15;

%% Import the LABVIEW data %%%%%%%%%%%%%%%%%%%%%%%%%%%%%%%%%%%%%%%%%%%%%%%%%%%%%%%%%%%%%%%%%%%%%%%%%
% Raw data from LABVIEW generated text file
rawdata = importdata('H:\TEST DATA\SS Data\Smooth Plate Laminar
(113012)\Smooth_Laminar_113012.txt');
% Indices where calibration images were taken for each heated section
Cal_ind = [16, 27, 35, 45, 63];
% Indices where steady state images were taken for each section
SS_ind = [715, 719, 722, 725, 732];

% Break rawdata into the calibration and steady state data only and
% write to text file for use in Mathcad
avg_data = [rawdata.data(Cal_ind,:) ; rawdata.data(SS_ind,:)];
dlmwrite('H:\TEST DATA\Data Analysis\smooth_laminar_uncert.txt',...
        avg_data);

% Column indices with power data for each heated section
E_ind = [36, 37, 38, 39]; % voltage
I_ind = [40, 41, 42, 43]; % current

% Extract voltage for sections 0-3 at steady state [V]
for i = 1:4
    E(i) = avg_data(i+5, E_ind(i));
end
E(5) = 4.597; % Manually input voltage for section 4

% Extract current for sections 0-3 at steady state [A]
for i = 1:4
    I(i) = avg_data(i+5, I_ind(i));
end
I(1) = I(1)*2; % Apply current transducer factor for section 0
I(5) = 2.078; % Manually input current for section 4

% Inlet air pressure
P = avg_data(:,53); % [Pa]

% Inlet air relative humidity
RH = avg_data(:,54); % [%]

%% Thermocouple values at calibration %%%%%%%%%%%%%%%%%%%%%%%%%%%%%%%%%%%%%%%%%%%%%%%%%%%%%%%%%%%%%%%%%%%%%%%%%
% Subsurface and underplate TCs, converted to K

```

```

TC0_Cal = avg_data(1,2) + 273.15;    TC8_Cal = avg_data(1,10) + 273.15;
TC1_Cal = avg_data(1,3) + 273.15;    TC9_Cal = avg_data(1,11) + 273.15;
TC2_Cal = avg_data(1,4) + 273.15;    TC10_Cal = avg_data(1,12) + 273.15;
TC3_Cal = avg_data(2,5) + 273.15;    TC11_Cal = avg_data(2,13) + 273.15;
TC4_Cal = avg_data(2,6) + 273.15;    TC12_Cal = avg_data(2,14) + 273.15;
TC5_Cal = avg_data(3,7) + 273.15;    TC13_Cal = avg_data(3,15) + 273.15;
TC6_Cal = avg_data(4,8) + 273.15;    TC14_Cal = avg_data(4,16) + 273.15;
TC7_Cal = avg_data(5,9) + 273.15;    TC15_Cal = avg_data(5,17) + 273.15;

```

```

% Freestream TCs, converted to K

```

```

FS_0_Cal = avg_data(1,18) + 273.15;
FS_1_Cal = avg_data(2,18) + 273.15;
FS_2_Cal = avg_data(3,18) + 273.15;
FS_3_Cal = avg_data(4,18) + 273.15;
FS_4_Cal = avg_data(5,18) + 273.15;

```

```

% Average freestream temperature (for TC calibration)

```

```

FS_Cal_Avg = (FS_0_Cal + FS_1_Cal + FS_2_Cal + FS_3_Cal + FS_4_Cal)/5;

```

```

%% Thermocouple values at steady state %%%%%%%%%%%%%%%%%%%%%%%%%%%%%%%%%%%%%%%%%%

```

```

% Subsurface and underplate TCs, converted to K

```

```

TC0_SS = avg_data(6,2) + 273.15;    TC8_SS = avg_data(6,10) + 273.15;
TC1_SS = avg_data(6,3) + 273.15;    TC9_SS = avg_data(6,11) + 273.15;
TC2_SS = avg_data(6,4) + 273.15;    TC10_SS = avg_data(6,12) + 273.15;
TC3_SS = avg_data(7,5) + 273.15;    TC11_SS = avg_data(7,13) + 273.15;
TC4_SS = avg_data(7,6) + 273.15;    TC12_SS = avg_data(7,14) + 273.15;
TC5_SS = avg_data(8,7) + 273.15;    TC13_SS = avg_data(8,15) + 273.15;
TC6_SS = avg_data(9,8) + 273.15;    TC14_SS = avg_data(9,16) + 273.15;
TC7_SS = avg_data(10,9)+ 273.15;    TC15_SS = avg_data(10,17)+ 273.15;

```

```

% Freestream TCs, converted to K

```

```

FS_0_SS = avg_data(6,18) + 273.15;
FS_1_SS = avg_data(7,18) + 273.15;
FS_2_SS = avg_data(8,18) + 273.15;
FS_3_SS = avg_data(9,18) + 273.15;
FS_4_SS = avg_data(10,18) + 273.15;

```

```

%% Corrected thermocouple steady state values %%%%%%%%%%%%%%%%%%%%%%%%%%%%%%%%%%%%%%%%%%

```

```

% Heated section 0 TCs

```

```

TC0_Cor = TC0_SS - (TC0_Cal - FS_Cal_Avg);
TC8_Cor = TC8_SS - (TC8_Cal - FS_Cal_Avg);
TC1_Cor = TC1_SS - (TC1_Cal - FS_Cal_Avg);
TC9_Cor = TC9_SS - (TC9_Cal - FS_Cal_Avg);
TC2_Cor = TC2_SS - (TC2_Cal - FS_Cal_Avg);
TC10_Cor = TC10_SS - (TC10_Cal - FS_Cal_Avg);
FS_0_Cor = FS_0_SS - (FS_0_Cal - FS_Cal_Avg);

```

```

% Heated section 1 TCs

```

```

TC3_Cor = TC3_SS - (TC3_Cal - FS_Cal_Avg);
TC11_Cor = TC11_SS - (TC11_Cal - FS_Cal_Avg);
TC4_Cor = TC4_SS - (TC4_Cal - FS_Cal_Avg);

```

```

TC12_Cor = TC12_SS - (TC12_Cal - FS_Cal_Avg);
FS_1_Cor = FS_1_SS - (FS_1_Cal - FS_Cal_Avg);

% Heated section 2 TCs
TC5_Cor = TC5_SS - (TC5_Cal - FS_Cal_Avg);
TC13_Cor = TC13_SS - (TC13_Cal - FS_Cal_Avg);
FS_2_Cor = FS_2_SS - (FS_2_Cal - FS_Cal_Avg);

% Heated section 3 TCs
TC6_Cor = TC6_SS - (TC6_Cal - FS_Cal_Avg);
TC14_Cor = TC14_SS - (TC14_Cal - FS_Cal_Avg);
FS_3_Cor = FS_3_SS - (FS_3_Cal - FS_Cal_Avg);

% Heated section 4 TCs
TC7_Cor = TC7_SS - (TC7_Cal - FS_Cal_Avg);
TC15_Cor = TC15_SS - (TC15_Cal - FS_Cal_Avg);
FS_4_Cor = FS_4_SS - (FS_4_Cal - FS_Cal_Avg);

%% Correct IR temperatures for transmissivity %%%%%%%%%%%
% Apply correction to each heated section pixel map
Pos_0_Cor = ((Pos_0_SS.^4 - Pos_0_Cal.^4)./tau + FS_Cal_Avg^4).^0.25);
Pos_1_Cor = ((Pos_1_SS.^4 - Pos_1_Cal.^4)./tau + FS_Cal_Avg^4).^0.25);
Pos_2_Cor = ((Pos_2_SS.^4 - Pos_2_Cal.^4)./tau + FS_Cal_Avg^4).^0.25);
Pos_3_Cor = ((Pos_3_SS.^4 - Pos_3_Cal.^4)./tau + FS_Cal_Avg^4).^0.25);
Pos_4_Cor = ((Pos_4_SS.^4 - Pos_4_Cal.^4)./tau + FS_Cal_Avg^4).^0.25);

%% Calculate air properties %%%%%%%%%%%
% Average freestream properties
T_inf = (FS_0_Cor + FS_1_Cor + FS_2_Cor + FS_3_Cor + FS_4_Cor)/5; % [K]
P_inf = mean(P(6:10)); % [Pa]
RH_inf = mean(RH(6:10)); % [%]
U_inf = avg_data(6,57); % [m/s]

% Use the freestream properties above in MathCAD to get air properties
rho_air = 1.204; % density [kg/m^3]
mu_air = 1.891e-5; % viscosity [kg/ms]
k_air = 0.02569; % thermal conductivity [(m*kg)/(K*s^3)]
Pr_air = 0.744; % Prandtl number

%% Experimental local convective heat transfer coefficients %%%%%%%%%%%
h_0 = (E(1)*I(1)/A_t(1) - k_p/t_p*(TC1_Cor - TC9_Cor) - sig*eps*
(Pos_0_Cor.^4 - FS_0_Cor^4)).*(Pos_0_Cor - FS_0_Cor).^(-1);
h_1 = (E(2)*I(2)/A_t(2) - k_p/t_p*(TC4_Cor - TC12_Cor) - sig*eps*
(Pos_1_Cor.^4 - FS_1_Cor^4)).*(Pos_1_Cor - FS_1_Cor).^(-1);
h_2 = (E(3)*I(3)/A_t(3) - k_p/t_p*(TC5_Cor - TC13_Cor) - sig*eps*
(Pos_2_Cor.^4 - FS_2_Cor^4)).*(Pos_2_Cor - FS_2_Cor).^(-1);
h_3 = (E(4)*I(4)/A_t(4) - k_p/t_p*(TC6_Cor - TC14_Cor) - sig*eps*
(Pos_3_Cor.^4 - FS_3_Cor^4)).*(Pos_3_Cor - FS_3_Cor).^(-1);
h_4 = (E(5)*I(5)/A_t(5) - k_p/t_p*(TC7_Cor - TC15_Cor) - sig*eps*
(Pos_4_Cor.^4 - FS_4_Cor^4)).*(Pos_4_Cor - FS_4_Cor).^(-1);

```

```

% Spanwise average values along the centerline +/- 0.5"
for i = 1:320
    h_0_avg(i) = sum(h_0(100:149,i))/50;
end

for i = 1:320
    h_1_avg(i) = sum(h_1(100:149,i))/50;
end

for i = 1:320
    h_2_avg(i) = sum(h_2(100:149,i))/50;
end

for i = 1:320
    h_3_avg(i) = sum(h_3(100:149,i))/50;
end

for i = 1:320
    h_4_avg(i) = sum(h_4(100:149,i))/50;
end

%% Theoretical heat transfer coefficients from laminar correlation %%
h_lam_0 = 0.453.*((U_inf*x_0*0.0254*rho_air)./mu_air).^(1/2).*(Pr_air)^(1/3).*k_air.*(x_0*0.0254).^(-1).*(1-(zeta./x_0).^(3/4)).^(-1/3);
h_lam_1 = 0.453.*((U_inf*x_1*0.0254*rho_air)./mu_air).^(1/2).*(Pr_air)^(1/3).*k_air.*(x_1*0.0254).^(-1).*(1-(zeta./x_1).^(3/4)).^(-1/3);
h_lam_2 = 0.453.*((U_inf*x_2*0.0254*rho_air)./mu_air).^(1/2).*(Pr_air)^(1/3).*k_air.*(x_2*0.0254).^(-1).*(1-(zeta./x_2).^(3/4)).^(-1/3);
h_lam_3 = 0.453.*((U_inf*x_3*0.0254*rho_air)./mu_air).^(1/2).*(Pr_air)^(1/3).*k_air.*(x_3*0.0254).^(-1).*(1-(zeta./x_3).^(3/4)).^(-1/3);
h_lam_4 = 0.453.*((U_inf*x_4*0.0254*rho_air)./mu_air).^(1/2).*(Pr_air)^(1/3).*k_air.*(x_4*0.0254).^(-1).*(1-(zeta./x_4).^(3/4)).^(-1/3);

```

APPENDIX B

Evaluation of Uncertainty Mathcad Worksheet

This appendix contains the Mathcad worksheet used to perform the evaluation of uncertainty for the smooth laminar surface test data. A similar worksheet was used for the other surfaces.

Read in data and assign variable names

Steady-state data file from MATLAB

SS_Data :=
smooth_lam[uncert.txt]

Heated area power measurements

Voltage

Current

$$E := \begin{pmatrix} \text{SS_Data}_{5,35} \\ \text{SS_Data}_{5,35} \\ \text{SS_Data}_{5,35} \\ \text{SS_Data}_{6,36} \\ \text{SS_Data}_{6,36} \\ \text{SS_Data}_{7,37} \\ \text{SS_Data}_{8,38} \\ 4.597 \end{pmatrix} \quad V = \begin{pmatrix} 4.527 \\ 4.527 \\ 4.527 \\ 4.517 \\ 4.517 \\ 4.536 \\ 4.492 \\ 4.597 \end{pmatrix} \quad V$$

$$I := \begin{pmatrix} 2\text{SS_Data}_{5,39} \\ 2\text{SS_Data}_{5,39} \\ 2\text{SS_Data}_{5,39} \\ \text{SS_Data}_{6,40} \\ \text{SS_Data}_{6,40} \\ \text{SS_Data}_{7,41} \\ \text{SS_Data}_{8,42} \\ 2.078 \end{pmatrix} \quad A = \begin{pmatrix} 1.636 \\ 1.636 \\ 1.636 \\ 2.088 \\ 2.088 \\ 2.084 \\ 2.121 \\ 2.078 \end{pmatrix} \quad A$$

Heated area measurements

Heated area width and length

Heated area

$$W_{ha} := \begin{pmatrix} 6.375 \\ 6.375 \\ 6.375 \\ 6.375 \\ 6.375 \\ 6.375 \\ 6.375 \\ 6.375 \end{pmatrix} \text{ in} \quad L_{ha} := \begin{pmatrix} 5.5 \\ 5.5 \\ 5.5 \\ 7 \\ 7 \\ 7 \\ 7 \\ 7 \end{pmatrix} \text{ in}$$

$$A_t := \overrightarrow{(W_{ha} \cdot L_{ha})} = \begin{pmatrix} 35.063 \\ 35.063 \\ 35.063 \\ 44.625 \\ 44.625 \\ 44.625 \\ 44.625 \\ 44.625 \end{pmatrix} \cdot \text{in}^2$$

Plexiglas properties

Thickness

Thermal conductivity

$$t_p := \begin{pmatrix} 0.72 \\ 0.72 \\ 0.72 \\ 0.72 \\ 0.72 \\ 0.72 \\ 0.72 \\ 0.72 \end{pmatrix} \text{ in}$$

$$k_p := 0.18 \frac{\text{W}}{\text{m} \cdot \text{K}}$$

Radiation constants

Surface emissivity

$$\varepsilon := 0.95$$

Stefan-Boltzman constant

$$\sigma := 5.67 \times 10^{-8} \frac{\text{W}}{\text{m}^2 \cdot \text{K}^4}$$

Transmissivity

$$\tau := 0.82$$

Uncertainty constants

Student's t value

$$t := 2$$

Correlated uncertainty

$$B_T := 1.4\text{K}$$

Section 0 IR temperature maps and 50 pixel by 50 pixel center point submatrix

SS_0_raw :=
...\Pos_0_SS.txt

Cal_0_raw :=
...\Pos_0_Cal.txt

SS_0a := submatrix(SS_0_raw, 102, 151, 65, 114) °C

Cal_0a := submatrix(Cal_0_raw, 102, 151, 65, 114) °C

SS_0b := submatrix(SS_0_raw, 102, 151, 134, 183) °C

Cal_0b := submatrix(Cal_0_raw, 102, 151, 134, 183) °C

SS_0c := submatrix(SS_0_raw, 102, 151, 203, 252) °C

Cal_0c := submatrix(Cal_0_raw, 102, 151, 203, 252) °C

Section 1 IR temperature maps and 50 pixel by 50 pixel center point submatrix

SS_1_raw :=
...\Pos_1_SS.txt

Cal_1_raw :=
...\Pos_1_Cal.txt

SS_1a := submatrix(SS_1_raw, 102, 151, 47, 96) °C

Cal_1a := submatrix(Cal_1_raw, 102, 151, 47, 96) °C

SS_1b := submatrix(SS_1_raw, 102, 151, 134, 183) °C

Cal_1b := submatrix(Cal_1_raw, 102, 151, 134, 183) °C

Section 2 IR temperature maps and 50 pixel by 50 pixel center point submatrix

SS_2_raw :=
...\Pos_2_SS.txt

Cal_2_raw :=
...\Pos_2_Cal.txt

SS_2 := submatrix(SS_2_raw, 102, 151, 134, 183) °C

Cal_2 := submatrix(Cal_2_raw, 102, 151, 134, 183) °C

Section 3 IR temperature maps and 50 pixel by 50 pixel center point submatrix

SS_3_raw :=
...\Pos_3_SS.txt

Cal_3_raw :=
...\Pos_3_Cal.txt

SS_3 := submatrix(SS_3_raw, 102, 151, 134, 183) °C

Cal_3 := submatrix(Cal_3_raw, 102, 151, 134, 183) °C

Section 4 IR temperature maps and 50 pixel by 50 pixel center point submatrix

SS_4_raw := ... \Pos_4_SS.txt Cal_4_raw := ... \Pos_4_Cal.txt

SS_4 := submatrix(SS_4_raw, 102, 151, 134, 183) °C Cal_4 := submatrix(Cal_4_raw, 102, 151, 134, 183) °C

Subsurface, under plate, and freestream thermocouple measurements

	calibration	steady state		calibration	steady state	
$T_{SS_raw} :=$	(SS_Data _{0,1}	SS_Data _{5,1}	(SS_Data _{0,9}	SS_Data _{5,9}
		SS_Data _{0,2}	SS_Data _{5,2}		SS_Data _{0,10}	SS_Data _{5,10}
		SS_Data _{0,3}	SS_Data _{5,3}		SS_Data _{0,11}	SS_Data _{5,11}
		SS_Data _{1,4}	SS_Data _{6,4}		SS_Data _{1,12}	SS_Data _{6,12}
		SS_Data _{1,5}	SS_Data _{6,5}		SS_Data _{1,13}	SS_Data _{6,13}
		SS_Data _{2,6}	SS_Data _{7,6}		SS_Data _{2,14}	SS_Data _{7,14}
		SS_Data _{3,7}	SS_Data _{8,7}		SS_Data _{3,15}	SS_Data _{8,15}
		SS_Data _{4,8}	SS_Data _{9,8}		SS_Data _{4,16}	SS_Data _{9,16}
) °C) °C	

	calibration	steady state	
$T_{inf_raw} :=$	(SS_Data _{0,17}	SS_Data _{5,17}
		SS_Data _{0,17}	SS_Data _{5,17}
		SS_Data _{0,17}	SS_Data _{5,17}
		SS_Data _{1,17}	SS_Data _{6,17}
		SS_Data _{1,17}	SS_Data _{6,17}
		SS_Data _{2,17}	SS_Data _{7,17}
		SS_Data _{3,17}	SS_Data _{8,17}
		SS_Data _{4,17}	SS_Data _{9,17}
) °C	

Calculate the corrected temperature values

Freestream average temperature at calibration

$T_{inf_cal} := \text{mean}(T_{inf_raw_{1,0}}, T_{inf_raw_{4,0}}, T_{inf_raw_{5,0}}, T_{inf_raw_{6,0}}, T_{inf_raw_{7,0}}) = 292.819 \text{ K}$

Corrected steady state temperatures for subsurface, under plate, and freestream thermocouples

$$T_{SS} := T_{SS_raw}^{\langle 1 \rangle} - \left(T_{SS_raw}^{\langle 0 \rangle} - T_{inf_cal} \right) = \begin{pmatrix} 304.227 \\ 304.221 \\ 304.727 \\ 306.016 \\ 306.988 \\ 306.329 \\ 306.941 \\ 307.413 \end{pmatrix} \text{ K} \quad \text{Subsurface temperature}$$

$$T_{UP} := T_{UP_raw}^{\langle 1 \rangle} - \left(T_{UP_raw}^{\langle 0 \rangle} - T_{inf_cal} \right) = \begin{pmatrix} 296.447 \\ 295.35 \\ 295.754 \\ 296.34 \\ 296.656 \\ 297.133 \\ 297.51 \\ 297.583 \end{pmatrix} \text{ K} \quad \text{Under the plate temperature}$$

$$T_{\infty} := T_{inf_raw}^{\langle 1 \rangle} - \left(T_{inf_raw}^{\langle 0 \rangle} - T_{inf_cal} \right) = \begin{pmatrix} 294.16 \\ 294.16 \\ 294.16 \\ 294.167 \\ 294.167 \\ 294.123 \\ 293.884 \\ 293.661 \end{pmatrix} \text{ K} \quad \text{Freestream temperature}$$

Corrected IR temperature measurement, averaged in the 50x50 pixel center area

$$T_{\text{avg}} := \begin{matrix} \left[\left[\left[\left(\frac{SS_{0a}^4 - Cal_{0a}^4}{\tau} + T_{\text{inf_cal}}^4 \right)^{0.25} \right] \right] \right] K \\ \left[\left[\left[\left(\frac{SS_{0b}^4 - Cal_{0b}^4}{\tau} + T_{\text{inf_cal}}^4 \right)^{0.25} \right] \right] \right] K \\ \left[\left[\left[\left(\frac{SS_{0c}^4 - Cal_{0c}^4}{\tau} + T_{\text{inf_cal}}^4 \right)^{0.25} \right] \right] \right] K \\ \left[\left[\left[\left(\frac{SS_{1a}^4 - Cal_{1a}^4}{\tau} + T_{\text{inf_cal}}^4 \right)^{0.25} \right] \right] \right] K \\ \left[\left[\left[\left(\frac{SS_{1b}^4 - Cal_{1b}^4}{\tau} + T_{\text{inf_cal}}^4 \right)^{0.25} \right] \right] \right] K \\ \left[\left[\left[\left(\frac{SS_{2}^4 - Cal_{2}^4}{\tau} + T_{\text{inf_cal}}^4 \right)^{0.25} \right] \right] \right] K \\ \left[\left[\left[\left(\frac{SS_{3}^4 - Cal_{3}^4}{\tau} + T_{\text{inf_cal}}^4 \right)^{0.25} \right] \right] \right] K \\ \left[\left[\left[\left(\frac{SS_{4}^4 - Cal_{4}^4}{\tau} + T_{\text{inf_cal}}^4 \right)^{0.25} \right] \right] \right] K \end{matrix} = \begin{matrix} \left(\begin{matrix} 301.463 \\ 302.388 \\ 303.412 \\ 304.182 \\ 304.394 \\ 307.186 \\ 307.33 \\ 306.37 \end{matrix} \right) K \end{matrix} \quad \text{Area averaged IR temperature}$$

IR temperture standard deviation

$$S_{Tavg} := \begin{pmatrix} \left[\left[\left[\frac{SS_{0a}^4 - Cal_{0a}^4}{\tau} + T_{inf_cal}^4 \right]^{0.25} \right] \right] K \\ \left[\left[\left[\frac{SS_{0b}^4 - Cal_{0b}^4}{\tau} + T_{inf_cal}^4 \right]^{0.25} \right] \right] K \\ \left[\left[\left[\frac{SS_{0c}^4 - Cal_{0c}^4}{\tau} + T_{inf_cal}^4 \right]^{0.25} \right] \right] K \\ \left[\left[\left[\frac{SS_{1a}^4 - Cal_{1a}^4}{\tau} + T_{inf_cal}^4 \right]^{0.25} \right] \right] K \\ \left[\left[\left[\frac{SS_{1b}^4 - Cal_{1b}^4}{\tau} + T_{inf_cal}^4 \right]^{0.25} \right] \right] K \\ \left[\left[\left[\frac{SS_2^4 - Cal_2^4}{\tau} + T_{inf_cal}^4 \right]^{0.25} \right] \right] K \\ \left[\left[\left[\frac{SS_3^4 - Cal_3^4}{\tau} + T_{inf_cal}^4 \right]^{0.25} \right] \right] K \\ \left[\left[\left[\frac{SS_4^4 - Cal_4^4}{\tau} + T_{inf_cal}^4 \right]^{0.25} \right] \right] K \end{pmatrix} = \begin{pmatrix} 0.319 \\ 0.218 \\ 0.173 \\ 0.101 \\ 0.122 \\ 0.123 \\ 0.142 \\ 0.306 \end{pmatrix} K$$

Calculated average convective heat transfer coefficients

$$h_{\text{avg}}(E, I, A_t, k_p, t_p, T_{\text{SS}}, T_{\text{UP}}, \varepsilon, \sigma, T_{\infty}, T_{\text{avg}}) := \left[\frac{\frac{E \cdot I}{A_t} - \frac{k_p}{t_p} \cdot (T_{\text{SS}} - T_{\text{UP}}) - \varepsilon \cdot \sigma \cdot (T_{\text{avg}}^4 - T_{\infty}^4)}{(T_{\text{avg}} - T_{\infty})} \right]$$

$$h := h_{\text{avg}}(E, I, A_t, k_p, t_p, T_{\text{SS}}, T_{\text{UP}}, \varepsilon, \sigma, T_{\infty}, T_{\text{avg}}) = \begin{pmatrix} 28.647 \\ 23.456 \\ 20.088 \\ 17.432 \\ 16.313 \\ 12.345 \\ 11.856 \\ 12.674 \end{pmatrix} \cdot \frac{\text{W}}{\text{m}^2 \cdot \text{K}} \quad \text{Calculated convective heat transfer coefficients}$$

Uncertainty components for voltage

Random and fixed uncertainties

$$U_{E_{\text{rand}}} := \begin{pmatrix} \text{SS_Data}_{5,43} \\ \text{SS_Data}_{5,43} \\ \text{SS_Data}_{5,43} \\ \text{SS_Data}_{6,44} \\ \text{SS_Data}_{6,44} \\ \text{SS_Data}_{7,45} \\ \text{SS_Data}_{8,46} \\ 0 \end{pmatrix} \text{V} = \begin{pmatrix} 9.772 \times 10^{-5} \\ 9.772 \times 10^{-5} \\ 9.772 \times 10^{-5} \\ 1.16 \times 10^{-4} \\ 1.16 \times 10^{-4} \\ 8.618 \times 10^{-5} \\ 8.318 \times 10^{-5} \\ 0 \end{pmatrix} \text{V} \quad U_{E_{\text{fixed}}} := \begin{pmatrix} 0.03\% \cdot E_0 \\ 0.03\% \cdot E_1 \\ 0.03\% \cdot E_2 \\ 0.03\% \cdot E_3 \\ 0.03\% \cdot E_4 \\ 0.03\% \cdot E_5 \\ 0.03\% \cdot E_6 \\ 0.25\% \cdot E_7 \end{pmatrix} = \begin{pmatrix} 1.358 \times 10^{-3} \\ 1.358 \times 10^{-3} \\ 1.358 \times 10^{-3} \\ 1.355 \times 10^{-3} \\ 1.355 \times 10^{-3} \\ 1.361 \times 10^{-3} \\ 1.348 \times 10^{-3} \\ 0.011 \end{pmatrix} \text{V}$$

Total uncertainty

$$U_E := \sqrt{U_{E_rand}^2 + U_{E_fixed}^2} = \begin{pmatrix} 1.362 \times 10^{-3} \\ 1.362 \times 10^{-3} \\ 1.362 \times 10^{-3} \\ 1.36 \times 10^{-3} \\ 1.36 \times 10^{-3} \\ 1.363 \times 10^{-3} \\ 1.35 \times 10^{-3} \\ 0.011 \end{pmatrix} V$$

Uncertainty components for current

Random and fixed uncertainties

$$U_{I_rand} := \begin{pmatrix} SS_Data_{5,47} \\ SS_Data_{5,47} \\ SS_Data_{5,47} \\ SS_Data_{6,48} \\ SS_Data_{6,48} \\ SS_Data_{7,49} \\ SS_Data_{8,50} \\ 0 \end{pmatrix} A = \begin{pmatrix} 3.202 \times 10^{-4} \\ 3.202 \times 10^{-4} \\ 3.202 \times 10^{-4} \\ 7.483 \times 10^{-4} \\ 7.483 \times 10^{-4} \\ 5.49 \times 10^{-4} \\ 5.242 \times 10^{-4} \\ 0 \end{pmatrix} A$$

$$U_{I_fixed} := \begin{pmatrix} 0.1A \\ 0.1A \\ 0.1A \\ 0.05A \\ 0.05A \\ 0.05A \\ 0.05A \\ 2.5\% \cdot I_4 \end{pmatrix} = \begin{pmatrix} 0.1 \\ 0.1 \\ 0.1 \\ 0.05 \\ 0.05 \\ 0.05 \\ 0.05 \\ 0.052 \end{pmatrix} A$$

Total uncertainty

$$U_I := \sqrt{U_{I_rand}^2 + U_{I_fixed}^2} = \begin{pmatrix} 0.1000005 \\ 0.1000005 \\ 0.1000005 \\ 0.0500056 \\ 0.0500056 \\ 0.050003 \\ 0.0500027 \\ 0.0522025 \end{pmatrix} A$$

Uncertainty components for heated area and Plexiglas thickness

Fixed uncertainty for all distance measurements

$$U_{\text{dist_fixed}} := \frac{1}{32} \text{in}$$

$$U_{\text{At}} := \sqrt{(U_{\text{dist_fixed}} \cdot W_{\text{ha}})^2 + (U_{\text{dist_fixed}} \cdot L_{\text{ha}})^2} = \begin{pmatrix} 0.263 \\ 0.263 \\ 0.263 \\ 0.296 \\ 0.296 \\ 0.296 \\ 0.296 \\ 0.296 \\ 0.296 \end{pmatrix} \cdot \text{in}^2$$

Total uncertainty in thickness

$$U_{\text{tp}} := \begin{pmatrix} U_{\text{dist_fixed}} \\ U_{\text{dist_fixed}} \end{pmatrix} = \begin{pmatrix} 0.031 \\ 0.031 \\ 0.031 \\ 0.031 \\ 0.031 \\ 0.031 \\ 0.031 \\ 0.031 \\ 0.031 \end{pmatrix} \cdot \text{in}$$

Uncertainty for thermocouple temperatures

Random uncertainties

	calibration	steady state		
$U_{\text{TSS_raw}} :=$	$SS_Data_{5,18}$	$SS_Data_{5,18}$	$\Delta^{\circ}\text{C} =$	$\begin{pmatrix} 2.543 \times 10^{-3} & 2.543 \times 10^{-3} \\ 4.04 \times 10^{-3} & 2.994 \times 10^{-3} \\ 3.668 \times 10^{-3} & 3.668 \times 10^{-3} \\ 3.329 \times 10^{-3} & 2.983 \times 10^{-3} \\ 1.838 \times 10^{-3} & 2.741 \times 10^{-3} \\ 2.612 \times 10^{-3} & 3.908 \times 10^{-3} \\ 5.007 \times 10^{-3} & 3.812 \times 10^{-3} \\ 5.224 \times 10^{-3} & 3.162 \times 10^{-3} \end{pmatrix} \text{K}$
	$SS_Data_{0,19}$	$SS_Data_{5,19}$		
	$SS_Data_{5,20}$	$SS_Data_{5,20}$		
	$SS_Data_{1,21}$	$SS_Data_{6,21}$		
	$SS_Data_{1,22}$	$SS_Data_{6,22}$		
	$SS_Data_{2,23}$	$SS_Data_{7,23}$		
	$SS_Data_{3,24}$	$SS_Data_{8,24}$		
	$SS_Data_{4,25}$	$SS_Data_{9,25}$		

$$\begin{array}{c}
 \text{calibration} \quad \text{steady state} \\
 U_{\text{TUP_raw}} := \begin{pmatrix} \text{SS_Data}_{0,26} & \text{SS_Data}_{5,26} \\ \text{SS_Data}_{0,27} & \text{SS_Data}_{5,27} \\ \text{SS_Data}_{0,28} & \text{SS_Data}_{5,28} \\ \text{SS_Data}_{1,29} & \text{SS_Data}_{6,29} \\ \text{SS_Data}_{1,30} & \text{SS_Data}_{6,30} \\ \text{SS_Data}_{2,31} & \text{SS_Data}_{7,31} \\ \text{SS_Data}_{3,32} & \text{SS_Data}_{8,32} \\ \text{SS_Data}_{4,33} & \text{SS_Data}_{9,33} \end{pmatrix} \Delta^{\circ}\text{C} = \begin{pmatrix} 2.606 \times 10^{-3} & 2.973 \times 10^{-3} \\ 5.147 \times 10^{-3} & 4.922 \times 10^{-3} \\ 4.174 \times 10^{-3} & 6.054 \times 10^{-3} \\ 3.312 \times 10^{-3} & 3.413 \times 10^{-3} \\ 2.993 \times 10^{-3} & 4.784 \times 10^{-3} \\ 3.34 \times 10^{-3} & 4.051 \times 10^{-3} \\ 3.607 \times 10^{-3} & 4.732 \times 10^{-3} \\ 5.819 \times 10^{-3} & 1.673 \times 10^{-3} \end{pmatrix} \text{K}
 \end{array}$$

$$\begin{array}{c}
 \text{calibration} \quad \text{steady state} \\
 U_{\text{Tinf_raw}} := \begin{pmatrix} \text{SS_Data}_{0,34} & \text{SS_Data}_{5,34} \\ \text{SS_Data}_{0,34} & \text{SS_Data}_{5,34} \\ \text{SS_Data}_{0,34} & \text{SS_Data}_{5,34} \\ \text{SS_Data}_{1,34} & \text{SS_Data}_{6,34} \\ \text{SS_Data}_{1,34} & \text{SS_Data}_{6,34} \\ \text{SS_Data}_{2,34} & \text{SS_Data}_{7,34} \\ \text{SS_Data}_{3,34} & \text{SS_Data}_{8,34} \\ \text{SS_Data}_{4,34} & \text{SS_Data}_{9,34} \end{pmatrix} \Delta^{\circ}\text{C} = \begin{pmatrix} 0.011 & 5.816 \times 10^{-3} \\ 0.011 & 5.816 \times 10^{-3} \\ 0.011 & 5.816 \times 10^{-3} \\ 6.416 \times 10^{-3} & 5.496 \times 10^{-3} \\ 6.416 \times 10^{-3} & 5.496 \times 10^{-3} \\ 0.01 & 0.012 \\ 9.75 \times 10^{-3} & 0.012 \\ 9.338 \times 10^{-3} & 5.27 \times 10^{-3} \end{pmatrix} \text{K}
 \end{array}$$

Total uncertainty in subsurface TC measurements

$$U_{\text{TSS}} := \sqrt{\left(U_{\text{TSS_raw}}^{\langle 0 \rangle} \right)^2 + \left(U_{\text{TSS_raw}}^{\langle 1 \rangle} \right)^2 + \left(U_{\text{Tinf_raw}}^{\langle 0 \rangle} \right)^2 + B_{\text{T}}^2} = \begin{pmatrix} 1.4000452 \\ 1.4000496 \\ 1.4000502 \\ 1.4000218 \\ 1.4000186 \\ 1.4000447 \\ 1.4000481 \\ 1.4000445 \end{pmatrix} \text{K}$$

Total uncertainty in under the plate TC measurements

$$U_{TUP} := \sqrt{\left(U_{TUP_raw}^{\langle \phi \rangle} \right)^2 + \left(U_{TUP_raw}^{\langle l \rangle} \right)^2 + \left(U_{Tinf_raw}^{\langle \phi \rangle} \right)^2 + B_T^2} = \begin{pmatrix} 1.4000462 \\ 1.4000587 \\ 1.4000599 \\ 1.4000228 \\ 1.4000261 \\ 1.4000467 \\ 1.4000466 \\ 1.4000442 \end{pmatrix} \text{ K}$$

Total uncertainty in freestream TC measurements

$$U_{T\infty} := \sqrt{\left(U_{Tinf_raw}^{\langle \phi \rangle} \right)^2 + \left(U_{Tinf_raw}^{\langle l \rangle} \right)^2 + B_T^2} = \begin{pmatrix} 1.4000527 \\ 1.4000527 \\ 1.4000527 \\ 1.4000255 \\ 1.4000255 \\ 1.4000868 \\ 1.400089 \\ 1.4000411 \end{pmatrix} \text{ K}$$

Uncertainty for IR camera temperatures

Random uncertainty

$$U_{Tavg_rand} := \frac{t \cdot S_{Tavg}}{\sqrt{2500}} = \begin{pmatrix} 0.013 \\ 8.708 \times 10^{-3} \\ 6.919 \times 10^{-3} \\ 4.03 \times 10^{-3} \\ 4.886 \times 10^{-3} \\ 4.916 \times 10^{-3} \\ 5.669 \times 10^{-3} \\ 0.012 \end{pmatrix} \text{ K}$$

Total uncertainty

$$U_{T_{avg}} := \sqrt{U_{T_{avg_rand}}^2 + \left(U_{T_{inf_raw}} \cdot \langle \theta \rangle \right)^2 + B_T^2} = \begin{pmatrix} 1.4000987 \\ 1.4000677 \\ 1.4000577 \\ 1.4000205 \\ 1.4000232 \\ 1.4000455 \\ 1.4000454 \\ 1.4000845 \end{pmatrix} \text{ K}$$

Overall uncertainty in average convective heat transfer coefficients

Partial derivatives of h with respect to each variable

$$\begin{aligned} \theta_E(E, I, A_t, k_p, t_p, T_{SS}, T_{UP}, \varepsilon, \sigma, T_\infty, T_{avg}) &:= \frac{d}{dE} h_{avg}(E, I, A_t, k_p, t_p, T_{SS}, T_{UP}, \varepsilon, \sigma, T_\infty, T_{avg}) \\ &= \frac{I}{A_t \cdot (T_{avg} - T_\infty)} \end{aligned}$$

$$\begin{aligned} \theta_I(E, I, A_t, k_p, t_p, T_{SS}, T_{UP}, \varepsilon, \sigma, T_\infty, T_{avg}) &:= \frac{d}{dI} h_{avg}(E, I, A_t, k_p, t_p, T_{SS}, T_{UP}, \varepsilon, \sigma, T_\infty, T_{avg}) \\ &= \frac{E}{A_t \cdot (T_{avg} - T_\infty)} \end{aligned}$$

$$\begin{aligned} \theta_{A_t}(E, I, A_t, k_p, t_p, T_{SS}, T_{UP}, \varepsilon, \sigma, T_\infty, T_{avg}) &:= \frac{d}{dA_t} h_{avg}(E, I, A_t, k_p, t_p, T_{SS}, T_{UP}, \varepsilon, \sigma, T_\infty, T_{avg}) \\ &= - \frac{E \cdot I}{A_t^2 \cdot (T_{avg} - T_\infty)} \end{aligned}$$

$$\begin{aligned} \theta_{t_p}(E, I, A_t, k_p, t_p, T_{SS}, T_{UP}, \varepsilon, \sigma, T_\infty, T_{avg}) &:= \frac{d}{dt_p} h_{avg}(E, I, A_t, k_p, t_p, T_{SS}, T_{UP}, \varepsilon, \sigma, T_\infty, T_{avg}) \\ &= - \frac{k_p \cdot (T_{UP} - T_{SS})}{t_p^2 \cdot (T_{avg} - T_\infty)} \end{aligned}$$

$$\begin{aligned} \theta_{T_{SS}}(E, I, A_t, k_p, t_p, T_{SS}, T_{UP}, \varepsilon, \sigma, T_\infty, T_{avg}) &:= \frac{d}{dT_{SS}} h_{avg}(E, I, A_t, k_p, t_p, T_{SS}, T_{UP}, \varepsilon, \sigma, T_\infty, T_{avg}) \\ &= - \frac{k_p}{t_p \cdot (T_{avg} - T_\infty)} \end{aligned}$$

$$\begin{aligned}\theta_{T_{UP}}(E, I, A_t, k_p, t_p, T_{SS}, T_{UP}, \varepsilon, \sigma, T_\infty, T_{avg}) &:= \frac{d}{dT_{UP}} h_{avg}(E, I, A_t, k_p, t_p, T_{SS}, T_{UP}, \varepsilon, \sigma, T_\infty, T_{avg}) \\ &= \frac{k_p}{t_p \cdot (T_{avg} - T_\infty)}\end{aligned}$$

$$\begin{aligned}\theta_{T_\infty}(E, I, A_t, k_p, t_p, T_{SS}, T_{UP}, \varepsilon, \sigma, T_\infty, T_{avg}) &:= \frac{d}{dT_\infty} h_{avg}(E, I, A_t, k_p, t_p, T_{SS}, T_{UP}, \varepsilon, \sigma, T_\infty, T_{avg}) \\ &= \frac{\frac{E \cdot I}{A_t} - \sigma \cdot \varepsilon \cdot (T_{avg}^4 - T_\infty^4) + \frac{k_p \cdot (T_{UP} - T_{SS})}{t_p}}{(T_{avg} - T_\infty)^2} + \frac{4 \cdot \sigma \cdot \varepsilon \cdot T_\infty^3}{T_{avg} - T_\infty}\end{aligned}$$

$$\begin{aligned}\theta_{T_{avg}}(E, I, A_t, k_p, t_p, T_{SS}, T_{UP}, \varepsilon, \sigma, T_\infty, T_{avg}) &:= \frac{d}{dT_{avg}} h_{avg}(E, I, A_t, k_p, t_p, T_{SS}, T_{UP}, \varepsilon, \sigma, T_\infty, T_{avg}) \\ &= \frac{\frac{E \cdot I}{A_t} - \sigma \cdot \varepsilon \cdot (T_{avg}^4 - T_\infty^4) + \frac{k_p \cdot (T_{UP} - T_{SS})}{t_p}}{(T_{avg} - T_\infty)^2} - \frac{4 \cdot T_{avg}^3 \cdot \sigma \cdot \varepsilon}{T_{avg} - T_\infty}\end{aligned}$$

Calculated uncertainty components

$$\Psi_E := \left[\left(U_E \cdot \theta_E(E, I, A_t, k_p, t_p, T_{SS}, T_{UP}, \varepsilon, \sigma, T_\infty, T_{avg}) \right) \right]^2 = \begin{pmatrix} 1.818 \times 10^{-4} \\ 1.432 \times 10^{-4} \\ 1.133 \times 10^{-4} \\ 9.702 \times 10^{-5} \\ 9.303 \times 10^{-5} \\ 5.708 \times 10^{-5} \\ 5.474 \times 10^{-5} \\ 4.26 \times 10^{-3} \end{pmatrix} \cdot \left(\frac{W}{m^2 K} \right)^2$$

$$\Psi_I := \left[\left(U_I \cdot \theta_I(E, I, A_t, k_p, t_p, T_{SS}, T_{UP}, \varepsilon, \sigma, T_\infty, T_{avg}) \right) \right]^2 = \begin{pmatrix} 7.511 \\ 5.917 \\ 4.68 \\ 0.614 \\ 0.588 \\ 0.364 \\ 0.337 \\ 0.43 \end{pmatrix} \cdot \left(\frac{W}{m^2 K} \right)^2$$

$$\Psi_{A_t} := \left[\overrightarrow{\left(U_{A_t} \cdot \theta_{A_t}(E, I, A_t, k_p, t_p, T_{SS}, T_{UP}, \varepsilon, \sigma, T_\infty, T_{avg}) \right)} \right]^2 = \begin{pmatrix} 0.113 \\ 0.089 \\ 0.07 \\ 0.047 \\ 0.045 \\ 0.028 \\ 0.027 \\ 0.03 \end{pmatrix} \cdot \left(\frac{W}{m^2 K} \right)^2$$

$$\Psi_{t_p} := \left[\overrightarrow{\left(U_{t_p} \cdot \theta_{t_p}(E, I, A_t, k_p, t_p, T_{SS}, T_{UP}, \varepsilon, \sigma, T_\infty, T_{avg}) \right)} \right]^2 = \begin{pmatrix} 0.207 \\ 0.212 \\ 0.172 \\ 0.17 \\ 0.186 \\ 0.09 \\ 0.09 \\ 0.109 \end{pmatrix} \cdot \left(\frac{W}{m^2 K} \right)^2$$

$$\Psi_{T_{SS}} := \left[\overrightarrow{\left(U_{T_{SS}} \cdot \theta_{T_{SS}}(E, I, A_t, k_p, t_p, T_{SS}, T_{UP}, \varepsilon, \sigma, T_\infty, T_{avg}) \right)} \right]^2 = \begin{pmatrix} 3.56 \\ 2.805 \\ 2.218 \\ 1.893 \\ 1.815 \\ 1.113 \\ 1.05 \\ 1.176 \end{pmatrix} \cdot \left(\frac{W}{m^2 K} \right)^2$$

$$\Psi_{T_{UP}} := \left[\overrightarrow{\left(U_{T_{UP}} \cdot \theta_{T_{UP}}(E, I, A_t, k_p, t_p, T_{SS}, T_{UP}, \varepsilon, \sigma, T_\infty, T_{avg}) \right)} \right]^2 = \begin{pmatrix} 3.56 \\ 2.805 \\ 2.218 \\ 1.893 \\ 1.815 \\ 1.113 \\ 1.05 \\ 1.176 \end{pmatrix} \cdot \left(\frac{W}{m^2 K} \right)^2$$

$$\Psi_{T_{\infty}} := \left[\overrightarrow{\left(U_{T_{\infty}} \cdot \theta_{T_{\infty}}(E, I, A_t, k_p, t_p, T_{SS}, T_{UP}, \varepsilon, \sigma, T_{\infty}, T_{avg}) \right)} \right]^2 = \begin{pmatrix} 42.817 \\ 24.252 \\ 14.975 \\ 10.264 \\ 8.904 \\ 3.651 \\ 3.254 \\ 3.99 \end{pmatrix} \cdot \left(\frac{W}{m^2 K} \right)^2$$

$$\Psi_{T_{avg}} := \left[\overrightarrow{\left(U_{T_{avg}} \cdot \theta_{T_{avg}}(E, I, A_t, k_p, t_p, T_{SS}, T_{UP}, \varepsilon, \sigma, T_{\infty}, T_{avg}) \right)} \right]^2 = \begin{pmatrix} 43.877 \\ 25.052 \\ 15.607 \\ 10.789 \\ 9.394 \\ 3.97 \\ 3.556 \\ 4.322 \end{pmatrix} \cdot \left(\frac{W}{m^2 K} \right)^2$$

Correlated uncertainty contributions

$$\Psi_{CU1} := \frac{\overrightarrow{\left(2 \theta_{TSS}(E, I, A_t, k_p, t_p, T_{SS}, T_{UP}, \varepsilon, \sigma, T_{\infty}, T_{avg}) \right)}}{\left[\left(\theta_{TUP}(E, I, A_t, k_p, t_p, T_{SS}, T_{UP}, \varepsilon, \sigma, T_{\infty}, T_{avg}) \cdot B_T \right)^2 \right]^{-1}} = \begin{pmatrix} -7.121 \\ -5.61 \\ -4.437 \\ -3.786 \\ -3.631 \\ -2.226 \\ -2.1 \\ -2.351 \end{pmatrix} \cdot \left(\frac{W}{m^2 K} \right)^2$$

$$\Psi_{CU2} := \frac{\overrightarrow{\left(2 \theta_{TSS}(E, I, A_t, k_p, t_p, T_{SS}, T_{UP}, \varepsilon, \sigma, T_{\infty}, T_{avg}) \right)}}{\left[\left(\theta_{T_{\infty}}(E, I, A_t, k_p, t_p, T_{SS}, T_{UP}, \varepsilon, \sigma, T_{\infty}, T_{avg}) \cdot B_T \right)^2 \right]^{-1}} = \begin{pmatrix} -24.692 \\ -16.495 \\ -11.527 \\ -8.816 \\ -8.04 \\ -4.031 \\ -3.697 \\ -4.331 \end{pmatrix} \cdot \left(\frac{W}{m^2 K} \right)^2$$

$$\Psi_{CU3} := \frac{\overrightarrow{2\theta_{TSS}(E, I, A_t, k_p, t_p, T_{SS}, T_{UP}, \varepsilon, \sigma, T_\infty, T_{avg})}}{\left(\theta_{Tavg}(E, I, A_t, k_p, t_p, T_{SS}, T_{UP}, \varepsilon, \sigma, T_\infty, T_{avg}) \cdot B_T^2\right)^{-1}} = \begin{pmatrix} 24.995 \\ 16.765 \\ 11.768 \\ 9.039 \\ 8.259 \\ 4.204 \\ 3.865 \\ 4.508 \end{pmatrix} \cdot \left(\frac{W}{m^2 K}\right)^2$$

$$\Psi_{CU4} := \frac{\overrightarrow{2\theta_{TUP}(E, I, A_t, k_p, t_p, T_{SS}, T_{UP}, \varepsilon, \sigma, T_\infty, T_{avg})}}{\left(\theta_{T\infty}(E, I, A_t, k_p, t_p, T_{SS}, T_{UP}, \varepsilon, \sigma, T_\infty, T_{avg}) \cdot B_T^2\right)^{-1}} = \begin{pmatrix} 24.692 \\ 16.495 \\ 11.527 \\ 8.816 \\ 8.04 \\ 4.031 \\ 3.697 \\ 4.331 \end{pmatrix} \cdot \left(\frac{W}{m^2 K}\right)^2$$

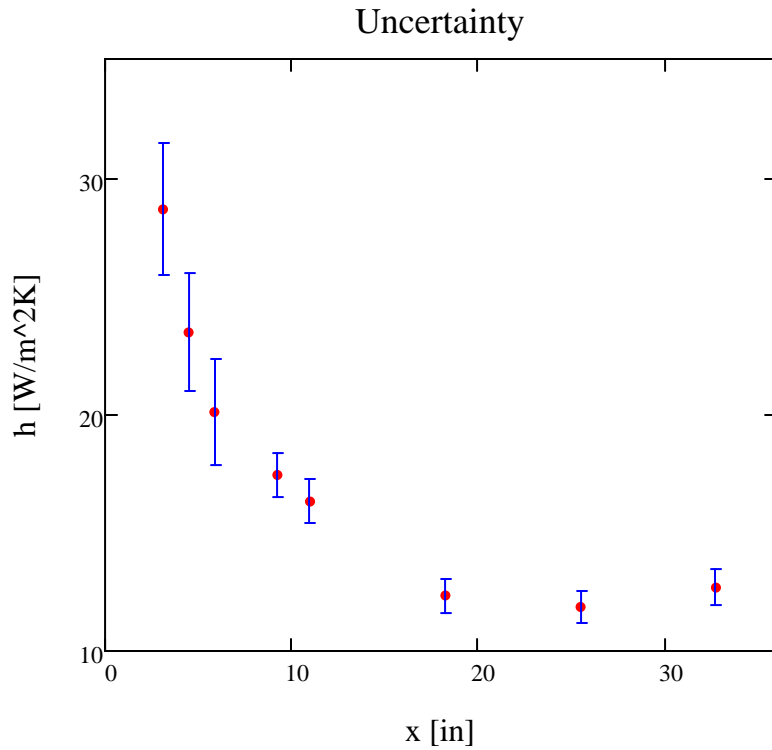
$$\Psi_{CU5} := \frac{\overrightarrow{2\theta_{TUP}(E, I, A_t, k_p, t_p, T_{SS}, T_{UP}, \varepsilon, \sigma, T_\infty, T_{avg})}}{\left(\theta_{Tavg}(E, I, A_t, k_p, t_p, T_{SS}, T_{UP}, \varepsilon, \sigma, T_\infty, T_{avg}) \cdot B_T^2\right)^{-1}} = \begin{pmatrix} -24.995 \\ -16.765 \\ -11.768 \\ -9.039 \\ -8.259 \\ -4.204 \\ -3.865 \\ -4.508 \end{pmatrix} \cdot \left(\frac{W}{m^2 K}\right)^2$$

$$\Psi_{CU6} := \frac{\overrightarrow{2\theta_{T\infty}(E, I, A_t, k_p, t_p, T_{SS}, T_{UP}, \varepsilon, \sigma, T_\infty, T_{avg})}}{\left(\theta_{Tavg}(E, I, A_t, k_p, t_p, T_{SS}, T_{UP}, \varepsilon, \sigma, T_\infty, T_{avg}) \cdot B_T^2\right)^{-1}} = \begin{pmatrix} -86.677 \\ -49.294 \\ -30.574 \\ -21.046 \\ -18.29 \\ -7.614 \\ -6.803 \\ -8.304 \end{pmatrix} \cdot \left(\frac{W}{m^2 K}\right)^2$$

Overall uncertainty in h

$$U_{\text{havg}} := \sqrt{\Psi_E + \Psi_I + \Psi_{At} + \Psi_{tp} + \Psi_{TSS} + \Psi_{TUP} + \Psi_{T\infty} + \Psi_{Tavg} \dots + \Psi_{CU1} + \Psi_{CU2} + \Psi_{CU3} + \Psi_{CU4} + \Psi_{CU5} + \Psi_{CU6}} = \begin{pmatrix} 2.80132 \\ 2.49597 \\ 2.22064 \\ 0.91575 \\ 0.90954 \\ 0.69966 \\ 0.67871 \\ 0.76232 \end{pmatrix} \cdot \frac{W}{m^2 K}$$

$$\frac{U_{\text{havg}}}{h} = \begin{pmatrix} 9.779 \\ 10.641 \\ 11.055 \\ 5.253 \\ 5.576 \\ 5.668 \\ 5.724 \\ 6.015 \end{pmatrix} \% \quad \text{Percent uncertainty}$$



REFERENCES

- [1] Addy, H.E., 2000, "Ice Accretions and Icing Effects for Modern Airfoil," NASA/TP-2000-210031.
- [2] Dillingham, G.L, 2010, "Preliminary Information on Aircraft Icing and Winter Operations," GAO-10-441T.
- [3] Cebeci, T., and Kafyeke, F., 2003, "Aircraft Icing," *Annual Review of Fluid Mechanics*, **35**, pp. 11-21.
- [4] Gent, R.W., Dart, N.P, and Cansdale, J.T., 2000, "Aircraft Icing," *Philosophical Transactions: Mathematical, Physical, and Engineering Sciences*, **358**(1776), pp. 2873-2911.
- [5] Jeck, R. K., 2002, "Icing Design Envelopes (14 CFR Parts 25 and 29, Appendix C) Converted to a Distance-Based Format," DOT/FAA/AR-00/30.
- [6] Code of Federal Regulations, Title 14, §25, Appendix C.
- [7] Wright, W.B., 2002, "User Manual for the NASA Glenn Ice Accretion Code LEWICE," NASA/CR-2002-211793.
- [8] Vargas, M., 2007, "Current Experimental Basis for Modeling Ice Accretions on Swept Wings," *Journal of Aircraft*, **44**(1), pp. 274-290.
- [9] Olsen, W., and Walker, E., 1986, "Experimental Evidence for Modifying the Current Physical Model for Ice Accretion on Aircraft Surfaces," NASA TM-87184.
- [10] Prandtl, L., 1904, "Über Flüssigkeitsbewegung bei sehr kleiner Reibung," Proceedings of the 3rd International Mathematics Congress, Heidelberg, Germany.
- [11] Bejan, A., 2004, *Convection Heat Transfer*, 2nd ed., John Wiley & Sons, Inc., Hoboken, NJ, pp. 38-39.
- [12] Cengel, Y.A., 2003, *Heat Transfer: A Practical Approach*, 2nd Ed., McGraw-Hill, Inc., New York, NY, pp. 373, 341, 359.
- [13] Munson, B.R., Okiishi, T.H., Huebsch, W.W., and Rothmayer, A.P., 2013, *Fundamentals of Fluid Mechanics*, 7th ed., John Wiley & Sons, Inc., Hoboken, NJ, pp. 482.

- [14] Schlichting, H., 1936, "Experimental Investigation of the Problem of Surface Roughness," TM-832, National Advisory Committee on Aeronautics.
- [15] Winkler, J. F., 1996, "Local Flowfield About Large Distributed Roughness Elements in a Laminar Boundary Layer," Ph.D. Dissertation, University of Illinois at Urbana-Champaign.
- [16] Mart, S.R., and McClain, S.T., 2012, "Protuberances in a Turbulent Thermal Boundary Layer," *Journal of Heat Transfer*, **134**.
- [17] Nikuradse, J., 1933, "Laws for Flows in Rough Pipes," *VDI-Forschungsheft*, **4**, pp. 361.
- [18] McClain, S. T., Vargas, M., Kreeger, R. E., and Tsao, J. C., 2007, "Heat Transfer from Protuberances", *Journal of Thermophysics and Heat Transfer*, **21**(2), pp. 337-345.
- [19] Wang, Z.J., Chi, X.K., Shih, T., and Bons, J.P., 2004, "Direct Simulation of Surface Roughness Effects with RANS and DES Approaches on Viscous Adaptive Cartesian Grids," AIAA-2004-2420.
- [20] Schetz, J.A., 2010, *Boundary Layer Analysis*, American Institute of Aeronautics and Astronautics, Virginia, pp. 21.
- [21] Poinsette, P.E., Van Fossen, G.J., and DeWitt, K.J., 1990, "Convective Heat Transfer Measurements from a NACA 0012 Airfoil in Flight and in the NASA Lewis Icing Research Tunnel," NASA TM-102448.
- [22] Anderson, D. N., and Shin, J., 1997, "Characterization of Ice Roughness from Simulated Icing Encounters," NASA TM-107400.
- [23] Anderson, D. N., Hentschel, D. B., and Ruff, G. A., 1998, "Measurement and Correlation of Ice Accretion Roughness," NASA CR-2003-211823.
- [24] Messinger, B.L., 1953, "Equilibrium Temperature of an Unheated Icing Surface as a Function of Air Speed," *Journal of Aeronautical Sciences*, pp. 29-42.
- [25] Dukhan, N., and Van Fossen, Jr., G. J., 2003, "Experimental Frossling Numbers for Ice-Roughened NACA 0012 Airfoils," *Journal of Aircraft*, **40**(6), pp. 1161-1167.
- [26] Shin, J., 1994, "Characteristics of Surface Roughness Associated With Leading Edge Ice Accretion," NASA TM-106459.
- [27] Bons, J. P., 2002, "St and Cf Augmentation for Real Turbine Roughness With Elevated Freestream Turbulence," *Journal of Turbomachinery*, **124**, pp. 632-644.

- [28] Croce, G., De Candido, E., Habashi, W. G., Munzar, J., Aubé M. S., Baruzzi, G. S., and Aliaga, C., 2010, “FENSAP-ICE: Analytical Model for Spatial and Temporal Evolution of In-Flight Icing Roughness,” *Journal of Aircraft*, **47**(4), pp. 1283-1289.
- [29] Myers, T.G., and Hammond, D.W., 1999, “Ice and Water Film Growth from Incoming Supercooled Droplets,” *International Journal of Heat and Mass Transfer*, **42**, pp. 2233-2242.
- [30] Bragg, M. B., Kerho, M. F., and Cummings, M. J., 1994, “Effect of Initial Ice Roughness on Airfoil Aerodynamics,” AIAA-94-0800.
- [31] Bragg, M. B., Cummings, M.J., Lee, S., and Henze, C.M., 1996, “Boundary-Layer and Heat-Transfer Measurements on an Airfoil with Simulated Ice Roughness,” AIAA-96-0866.
- [32] Beysens, D., 1995, “The Formation of Dew,” *Atmospheric Research*, **39**, pp. 215–237.
- [33] Mart, S. R., 2011, “The Effect of Roughness Element Thermal Conductivity on Turbulent Convection,” Master’s thesis, Department of Mechanical Engineering, Baylor University, TX.
- [34] The International Association for the Properties of Water and Steam, 2007, “Revised Release on the IAPWS Industrial Formulation 1997 for the Thermodynamic Properties of Water and Steam,” <http://www.iapws.org/>.
- [35] White, F. M., 2006, *Viscous Fluid Flow*, 3rd Ed, Boston, McGraw-Hill, Inc., New York, NY.
- [36] Wilke, C. R., 1950, “A Viscosity Equation for Gas Mixtures,” *Journal of Chemical Physics*, **18**(4), pp. 517-519.
- [37] Coleman, H. W., and Steele, W. G., 1999, *Experimentation and Uncertainty Analysis for Engineers*, 2nd ed., John Wiley and Sons, Inc., Hoboken, NJ.
- [38] Kline, S. J., and McClintock, F. A., 1953, “Describing Uncertainties in Single-Sample Experiments,” *Mechanical Engineering*, **75**, pp. 3-8.
- [39] Lee, S., Broeren, A.P., Addy, H.E., Sills, R., and Pifer, E.M., 2012, “Development of 3-D Ice Accretion Measurement Method,” NASA/TM-2012-217702.